ISSN 2708-6437(Online)
ISSN 2708-6429(Print)

Journal of Engineering Advancements

Editor-in-Chief:
Prof. Dr. Mohammad Mashud

Volume 02 Issue 03

Published by:
SciEn Publishing Group

Journal of Engineering Advancements
Apt. # 6 C-D, House # 191
Road # 9/A, Dhanmondi R/A
Dhaka-1209, Bangladesh
Email: jea@scienpg.com Website: www.scienpg.com/jea/

Published in: September 2021
Published by: SciEn Publishing Group

Price: Each Issue BDT 200.00 (US$ 15) **ISSN:** 2708-6437 (Online) 2708-6429 (Print)

Journal of Engineering Advancements

Volume 02, Issue 03 September 2021

CONTENTS

Original Articles

This page is intentionally left blank.

Journal of Engineering Advancements

Published by: SciEn Publishing Group

Apt. # 6 C-D, House # 191, Road # 9/A
Dhanmondi, Dhaka-1209, Bangladesh
Email Address: jea@scienpg.com

www.scienpg.com/jea/

This page is left intentionally blank

SciEn
Journal of Engineering Advancements Vol. 02(03) 2021, pp 118-124 https://doi.org/10.38032/jea.2021.03.001

Sentiment Analysis on Bengali Facebook Comments To Predict Fan's Emotions Towards a Celebrity

*Md. Serajus Salekin Khan, Sanjida Reza Rafa, Al Ekram Hossain Abir, Amit Kumar Das**

Department of Computer Science and Engineering, East West University, Dhaka, Bangladesh

Received: April 29, 2021, Revised: July 12, 2021, Accepted: July 14, 2021, Available Online: July 23, 2021

ABSTRACT

In this present era, sentiment analysis is considered one of the most rapidly growing fields of computer science study. It is a text mining technique that is automated and determines the emotion of a text. A text can be divided into many emotions using sentiment analysis. Since there are some studies on emotion analysis in the Bangla language, it is regarded as a key research area in the field of analyzing the Bangla language. This paper works with five different emotions: Happy, Sad, Angry, Surprised, and Excited. Apart from these emotions, our paper also deals with two categories, as Abusive and Religious. We used different machine learning techniques to train our dataset. We got an accuracy of 62% for Support Vector Machine (SVM), 58% for Random Forest (RF), 55% for K-Nearest Neighbors (KNN), 52% for Naïve Bayes (NB), and 50% for Neural Network.

Keywords: Sentiment, Celebrities, Machine Learning, tf-idf, svm, Emotion

1 Introduction

Sentiment analysis is also known as opinion mining, is the study of interpreting human feelings, which is the systematic detection, extraction, quantification, text interpretation, where NLP(Natural Language Processing) is used to investigate affective states and contextual intelligence. It is, in turn, a method for determining the emotional tone of a group of words, which is then used to get a better interpretation of the attitudes, opinions, and feelings expressed in an online mention.

Detecting underlying feelings has become a must in today's ever-changing world. We can gain major advantages in several fields by detecting the motive behind a human decision, which can range from buying a particular product to criminal motivation, employee-employer relationships, and so on. Sentiment analysis is a highly automated process that can be used to understand a viewpoint from spoken language, documents, or even video feeds.

Human Emotions are biochemical states resulting from neurophysiological shifts in the system [1]-[3] of the nerves that are linked to behavioral retaliation, feelings, thoughts. Psychologists have attempted to categorize the various kinds of feelings that people have. Few different ideas have arisen to categorize and describe the feelings that people feel. Psychologists have identified six basic emotions: sorrow, happiness, anxiety, disgust, rage, and surprise. Analysis of human reaction has exploded over the past two decades, with contributions from a variety of fields such as psychology, psychiatry, affective biology, sociology of feelings, computer science, medicine, history, and medicine. However, when researchers wanted to identify these basic human emotions from any text written by humans, speech, and facial expressions, the term 'Sentiment Analysis' is introduced in computer science.

The original academic studies of public opinion were performed during WWII and after WWII, with a mostly political impetus. However, contemporary sentiment research did not become mainstream until the mid-2000s and is mostly concentrated on online-based product ratings [4].

After the outbreak, the use of sentiment analysis has been extended to a number of other sectors, including stock market forecasting and terrorist attack reactions. Moreover, sentiment analysis is useful for social media monitoring because it helps us to see how the general public feels about a given subject. It has a wide range of applications and is highly efficient. Organizations all over the world are embracing the opportunity to derive information from social data.

However, when we went through with different research work on human emotion analysis, we found that there have been relatively few studies on emotion analysis in the Bangla language due to its language complexity, while several works have been done for English and other languages [5],[6]. Bangla is the world's fourth most common language, with about 250 million native speakers worldwide. As Bangla is one of the most popular languages and almost 250 million people are using Bangla to express their emotions, we emphasized Bangla to extract emotion. On the other hand, detecting any slang or abusive words in Bangla is comparatively more complex due to a lack of resources than in English [7],[8]. Moreover, there are religious variations among the Bengali speakers. People are using social media to defame different religious thoughts, and this is how religious violence is increasing day by day. Generally, people express their opinions and ideas through social media like Facebook, Twitter, etc., a considerable amount of data is available about various issues [9].

Being inspired by the application of sentiment analysis, in this paper, we proposed a method that will predict sentiment from text written in BANGLA using the SVM algorithm.

2 Related Works

Among various research areas of Computer science, sentiment analysis is considered one of the fastest-growing research topics. According to a review, the origins of sentiment analysis can be found in surveys on public opinion research at the turn of the twentieth century and text analysis conducted by a computational linguistics community in the 1990s [4].

*Corresponding Author Email Address: amit.csedu@gmail.com

Computer-based sentiment analysis moved towards the outbreak with the availability of texts on the web. This outbreak greatly impacted various fields by identifying the underlying emotion from any text or voice message. Many papers discussed the issue of sentiment analysis using a number of approaches. We had found several papers talking about our related field when we went through different papers.

Das. A. [10] et al. suggested a hybrid mechanism by integrating both rule-based and automated systems to derive the viewpoints from the text (Bangla and English). They have used Natural Language Processing (NLP) and SVM to implement this system. To get a better solution, Mahmudun M. et al. [9], used the concept of TF (term frequency) and IDF (inverse document frequency) values, and they extract the various characteristics of negative, positive, or neutral terms from text written in Bangla to get a more accurate result. Das D. [11] proposed an emotion monitoring method on a subject or event that used SentiWordNeT for both Bangla and English text and used sense-based affect scoring techniques. Hasan K.A. et al. [12] used SentiWordNet and WordNet to determine the polarity and meaning of words of the text to develop their methods for detecting sentiment from text written in the Bangla language. Chowdhury S. et al. [13] used the SVM and MaxEnt (Maximum Entropy) algorithm to extract sentiments from Bangla Microblog (Twitter) posts automatically, regardless of whether the polarity of the text is positive or negative. Go A. et al. [14] used three machine learning techniques: SVM, MaxEnt, and Naive Bayes to identify the emotions of Twitter messages with emoticons. Using HindiSentiWordNet (HSWN) and the Synset replacement algorithm, Pandey P. et al. [15] proposed a method for sentiment analysis of Hindi movie reviews. To extract emotion from any Bangla text, Tuhin R. A. et al. [16] proposed two machine learning techniques: the Naive Bayes Classification Algorithm and the Topical Method. The suggested methods have been used at both the article and sentence levels. Tembhurnikar S. D. et al. [17] developed a model based on LDA to analyze sentiment, which they used to rate tweets in terms of popularity. Umamaheswari K. et.al [18] used SVM and LDA to identify the viewpoint from the IMDB movie analysis dataset.

3 Methodology

Among the three broad areas of Machine learning, we used Supervised Learning. Since we worked on text classification and our dataset was multiclass labeled, supervised learning was the suitable approach for this kind of research. Because supervised classification of text is done when we have defined the classification categories [19]. This means that it requires the pre-labeled dataset with correct values.

Again, machines do not understand free text, image, or video data. It can read only 1s or 0s. To make data as machine-readable, the dataset must be transformed or encoded. For this case, we used Term Frequency-Inverse Document Frequency (TF-IDF) which is available in a python library called “Scikit-learn”.

So, the framework of this study includes- cleaning dataset and transform it into vector form. Learn the transformed dataset in machine learning models. To learn our dataset in the machine, we used the Support Vector Machine (SVM) classifier in this research. SVM gives very outstanding results compared to other classifiers such as K-Nearest Neighbors, Naive Bayes, Random Forest, Neural Network, Random Forest, which were also used in this research to ensure the validity of the result. SVM is so famous for its kernel trick to handle nonlinear input shapes [20]. Generally, supervised learning-based sentiment analysis consists of two measures for document classification. As shown in Fig. 1, it learns a model by using the training data. The trained classifier evaluates the model's accuracy in the testing process by predicting the target class of unknown test data.

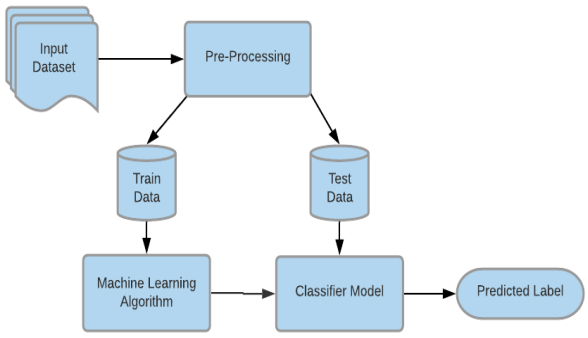

Fig. 1 Working Mechanism of proposed method

Table 1 Dataset Sample

Comments	Emotion
সত্যি সাকিব ভাইয়া মন থেকে তোমাকে অনেক ভালোবাসি	Happy
তোমার সেই গর্জন নিয়ে আবার মাঠে ফেরার অপেক্ষায় আছি	Excited
তদের বড়লোকি জীবন দেখলে আমরা ছোটলোকদের কষ্ট হয়	Sad
একজন বিধর্মীর জন্য এত আবেগ ভালো না	Religious
জতো পারিস তেল লাগা লুচ্চার বাচ্চা লাব হবে না	Abusive
গতি ১৪৫ কিঃমি বাংলার মিসাইল তাসকিনের বিধ্বংসী বোলিংয়ে অবাক সবাই	Surprised
এখানেও এসে কিছু ব্যাক্তি উপদেশ দিতে শুরু করবে যতসব নেকামি এই জাতি	Angry

3.1 Data collection

Data has been collected from some Facebook pages of Bangladeshi celebrities, including Cricketer, Actor, Actress, Youtuber, etc. For this research, data was specifically comments of general peoples on celebrity's Facebook pages. Facepager has been used for extracting comments from posts of some pages as it can fetch publicly available data from Facebook, YouTube, Twitter and other websites with JSON based API. To extract data with facepager, an access token is required. The token will be generated automatically when a profile is logged in via this tool. Another option to collect access token is a website called ‘Graph API Explorer- Facebook Developer’. The Graph API allows us to read and write data to and from the Facebook social graph. Facepager takes an id of the desired pages or profiles which we want to use for extracting data. After extraction, it stores the raw data in a SQLite database and later those data can be exported as a csv excel sheet [9].

We have collected 63,000 comments as raw data, including Bangla, English, and a mix of both Bangla and English language called Banglish or other languages. For collection sources, we

have used 12-15 pages of celebrities based on a 3-month duration. Table 1 shows some samples from our dataset, which represents a short scenario of the dataset.

3.2 Data Cleaning

Collected raw data has different varieties of comments where we required only pure Bangla text. It means that a text or comment should be written with only Bengali fonts and should not contain any other characters. Generally, in social media, people's comments in several types of language or mix of multiple language characters in a single comment. Since we need only Bangla comments, we had to clean and remove unnecessary data from the raw dataset as these data will create noise and reduce model accuracy.

The English and multilingual comments were removed first, leaving around 10,000 comments. The dataset after this process included either pure Bangla text or Bangla text mixed with some characters. So secondly, the remaining comments were cleaned based on conditions like each character's Unicode value in a comment should be ranged in between 2432 to 2559 or 32. Unicode value from 2432 to 2559 is for Bangla fonts and 32 for space. We manually labeled the dataset based on 10,000 data points. We have seven individual classes: Happy, Sad, Angry, Surprised, Excited, Abusive, and Religious.

3.3 Data Transformation

TF-IDF: By using TF-IDF, the dataset is transformed or encoded and features were extracted. This is a very common text-to-feature vectors conversion algorithm and creates a numerical representation of a pattern used for fitting machine algorithms for predictions [21]. TF-IDF score for a word in a dataset is calculated by multiplying two different metrics [22]. The 'Term Frequency' counts how many times word (w_i) appears in a document, and it is calculated by using Eq. (1).

$$TF_{i,j} = \frac{word\ i\ frequency\ in\ sentence\ j}{total\ words\ in\ sentence\ j} \quad (1)$$

Then the 'Inverse Document Frequency' means how common or rare a word in the entire dataset. It is calculated by using the following Eq. (2),

$$IDF_i = log\left(\frac{total\ number\ of\ sentence}{number\ of\ sentence\ contain\ i}\right) \quad (2)$$

where IDF value of a word is the logarithm of the total number of documents or sentences divided by the number of sentences that contains a word (w_i).

$$Score_{i,j} = TF_{i,j} \times IDF_i \quad (3)$$

where $score_{i,j}$ is the numeric value that tells how important word (w_i) is. So, it can be said that the importance of a keyword phrase is determined by comparing its frequency in large sets of documents.

Let assume a small dataset: ['*আপনাকে মাঠে দেখার অপেক্ষায় রইলাম*', '*আবার আপনাকে জাতীয় দলে দেখার অপেক্ষায়*', '*গানের অপেক্ষা করছি কবে শুনতে পাবো*']. Fig. 2 shows some sample tokens or features with their weights that are generated by TF-IDF based on the assumed dataset. TF-IDF generates tokens from every comment or sentence in a dataset, and each unique token gets a feature index. Finally, each sentence becomes a vector, and the weighted numbers of each vector represent the score of features.

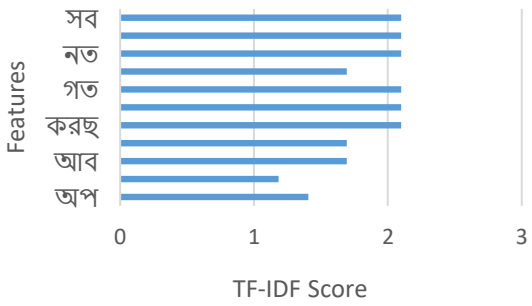

Fig. 2 Sample features with their Weights

3.4 Proposed Classifiers

3.4.1 Support Vector Machine

SVM is an algorithm that finds the best possible decision boundary between vectors that belong to the same group and those that do not belong to it. Generally, SVM works better with a small dataset, and sometimes it works better than the Neural Network-based models. This classifier categorizes n-dimensional space into classes by inventing the decision boundary so that new data points can be easily placed into the appropriate category in the future [23].

By definition, SVM is a two-class model, which means it can distinguish between two different classes. To separate two classes, there can be multiple hyperplanes that can be chosen. The best hyperplane has maximum separation between two classes. Since we dealt with 7 classes, the SVM, in this case, uses the One vs. Rest (OVR) approach. It splits the multiclass dataset into multiple binary classification problems. On each binary classification problem, a binary classifier is trained, and predictions are made using the most confident model [24]. For example, our classes were Happy, Sad, Angry, Surprised, Excited, Abusive and Religious. One binary classification can be like- Happy vs [Sad, Angry, Surprised, Excited, Abusive and Religious]. So, one class is fitted against all the other classes for each classifier. It provides a significant computational advantage to the multiclass problem [9].

3.4.2 Naïve Bayes

Classifying using Naive Bayes is simple and relies on probabilities of events. Despite its simplicity, it performs well in various text classification problems like sentiment analysis [9]. It is a method of statistical classification that is based on the Bayes Theorem, which is as follows:

$$P(X|Y) = P(X)\frac{P(Y|X)}{P(Y)} \quad (4)$$

where,

P(X)=probability of X (hypothesis)

P(Y)=probability of Y (data)

P(Y|X)=porbability of Y given X that the hypothesis X is true

P(X|Y)=probability of X given Y

We used the Multinomial NB classifier as it is suitable for this kind of research. Normally, integer feature counts are needed for the multinomial distribution. Fractional counts, such as TF-IDF, can also function in practice [25].

3.4.3 Neural Network

From the three classes of Artificial Neural Network, we used Multilayer Perceptron (MLP) classifier, which is a feedforward neural network. MLPs are very flexible and usefull for tabular datasets, classification problems, regression problems, etc. In MLP, nodes are arranged in multiple layers, such as input layers, hidden layers, and output layers. MLP uses a supervised learning method called backpropagation to train its models. A linear perceptron has only one layer, but an MLP has multiple layers and non-linear activation. Data that is not linearly separable can be differentiated using this method [26].

3.4.4 Random Forest

The Random forest algorithm generates decision trees based on data samples and then predicts each one and selects the most appropriate solution by voting. It's an ensemble method that's better than a single decision tree because it averages the results to minimize over-fitting [27]. Fig. 3 shows the working flow of the Random Forest classifier.

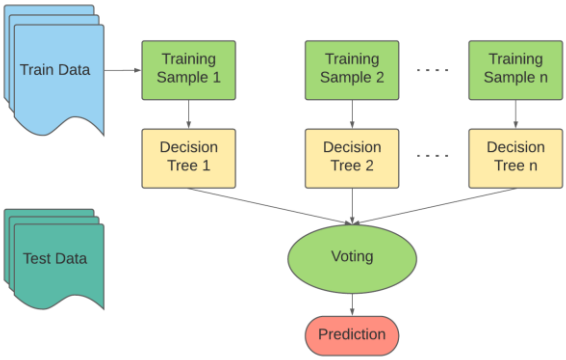

Fig. 3 Working flow of Random Forest

3.4.5 K-Nearest Neighbors

The KNN algorithm classifies data by identifying the K nearest matches in training data and then predicting using the class label of the nearest matches. Traditionally, euclidean distance has been used to find the nearest match. To calculate distance and make predictions, KNN needs a numerical representation of words that can be obtained from TF-IDF. The distance between all of these feature vectors generated by TF-IDF in the data-set will be determined from the feature vector of unlabeled text data. K-Nearest vectors will be chosen from among them, and the class with the highest frequency will be labeled to the unlabeled results.

4 Results & Analysis

4.1 Results

To better represent the proposed classifiers, we observed four different metrics called Precision, Recall, F1-Score, and Accuracy to evaluate and understand our model's performance more clearly. In every metric, 4 classifiers along with SVM were performed to observe which one works better.

4.1.1 Precision

The precision metric indicates how accurate the class is. This metric measures whether the prediction of the positive class is valid or not [9]. If the classifier correctly classifies all positive values, the maximum score is 1. However, precision can be calculated by Eq. (5).

$$Precision = \frac{TP}{TP + FP} \tag{5}$$

Which is the ratio of correctly predicted positive observations to the total number of positively predicted observations. So, a more precision score means less false positive rate.

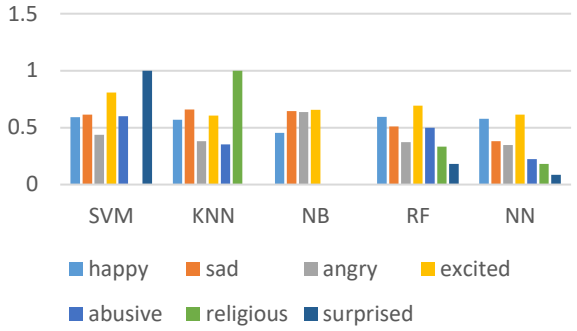

Fig. 4 Precision Score for 5 Classifiers

Fig. 4 shows that SVM has overall high Precision for all 7 classes. But it couldn't predict correctly the 'religious' class, which is here with zero precision. On the other hand, RF and NN classifiers had overall less precision value than SVM, but they could classify all of the classes. Precision alone does not help much due to its lack of consideration for the negative class. It is typically paired with the Recall metric.

4.1.2 Recall

The ratio of correctly expected positive observations to all observations in the actual class is known as recall [9]. Recall can be calculated by Eq. (6) where FN is considered, unlike precision.

$$Recall = \frac{TP}{TP + FN} \tag{6}$$

This metric indicates how well the model recognizes positive classes. So, a higher recall score means a lower false-positive rate.

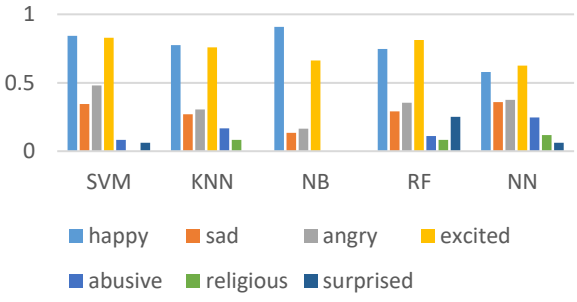

Fig. 5 Recall Score for 5 Classifiers

Fig. 5 shows that still SVM has an overall higher recall score than other classifiers but could not predict all classes correctly, as we discussed in the precision section. Since 'happy' and 'excited' classes are the majority, all of the classifiers have higher recall scores for them and a lower score for the rest of the classes.

4.1.3 F1 Score

The weighted average of Precision and Recall is the F1 Score. Thus, this score takes into account both false positives and false negatives. Although f1 is less intuitive than accuracy, it is generally more useful if the distribution of classes is uneven [28],[29]. When false positives and false negatives cost the same, accuracy works better. If they don't, then Precision and Recall can help that's why F1 Score came. F1 score can be calculated by Eq. (7), where FN is considered, unlike precision.

$$F1\ score = \frac{2 \times (Precision \times Recall)}{Precision + Recall} \quad (7)$$

To calculate F1 Score, we used a weighted average as our dataset was imbalanced, and we wanted to give more importance to some predictions based on their proportion. It takes a weighted mean of the measures. Each weight represents the number of samples in that class. Still, we cannot say directly which classifier is better because a higher F1-score does not necessarily mean a better classifier. It combines both Precision and Recall and measures overall model accuracy. So, a high f1 score also means high Precision and Recall.

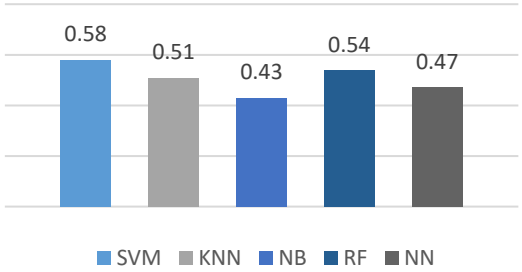

Fig. 6 Weighted F1-Scores for 5 classifiers

As shown in Fig. 6, F1 score 0.58, 0.51, 0.43, 0.54, 0.47 for SVM, KNN, NB, RF, NN respectively. SVM has a higher score than others, which means it predicted 58% of data correctly, considering both false positive and false negative values.

4.1.4 Accuracy

The ratio of correctly predicted True Positives and True Negatives to the total test dataset is known as accuracy. It can be calculated by Eq. (8), meaning that the number of correctly classified samples out of the total samples.

$$Accuracy = \frac{TP + TN}{TP + TN + FP + FN} \quad (8)$$

Two separate experiments were carried out to assess the accuracy of the proposed methods. We converted the dataset into two segments as 70% data for training and 30% data for testing to conduct these experiments. In the first experiment, we trained the dataset in all of the mentioned algorithms. In the second experiment, we mapped our 7 classes (Sad, Happy, Angry, Excited, Religious, Abusive, Surprised) into three higher classes- Positive, Negative, and Neutral.

Table 2 Mapping 7 classes into 3 higher class

New Emotion Class	Previous Emotion Class
Positive	Happy, Excited
Negative	Angry, Religious, Abusive
Neutral	Surprised, Sad

As shown in Table 2, the mapping is done based on the 7 types of class that express actual human sentiment or thoughts. Surprised and Sad comments imply neither positive nor negative, so these were mapped into neutral class. That means the dataset is labeled with these 3 classes rather than seven. Again all of the algorithms were trained with this dataset [16].

Fig. 7 Accuracy comparison between 5 classifiers

After training our algorithms with 7 class labeled dataset, we got an accuracy of 62% for Support Vector Machine (SVM), 58% for Random Forest (RF), 55% for K-Nearest Neighbors (KNN), 52% for Naïve Bayes (NB) and 50% for Neural Network. And with 3 class labeled dataset, we got accuracy 73%, 71%, 68%, 68%, and 67% for SVM, RF, NN, KNN, and NB, respectively. Accuracy from two different experiments shown in Fig. 7. In both experiments, SVM worked better than the rest of the algorithms.

From the above four different types of metrics, it is cleared that SVM is the best suitable for this research as it worked better than other classifiers. This means SVM can be chosen for the future to predict human emotion towards a person or anything. Generally, this research aims to extract emotion from the comment of the different posts on social media, where people can comment on something. Many comments can be collected from social sites in an automated way, and later the proposed algorithm SVM will predict a human expression or a comment easily. For which algorithm must be trained with sample data first. So, in the future, a complete automated tool is possible to detect human sentiment.

4.2 Validation

Since SVM performed better in every experiment, we applied cross-validation to validate the stability and confusion matrix to evaluate performance.

4.2.1 Confusion Matrix

The confusion matrix is a better option for reporting results in Multi-class classification problems because it helps to observe the relations between the classifier outputs and the true ones [30]. Fig. 8 is a 7 x 7 Confusion matrix which is used for evaluating the performance of the SVM classifier, where 7 is the total number of target classes. The matrix compares actual target values and the ones predicted by the SVM classifier. This gives us a more comprehensive view of our classification model's performance and the errors it is making [28]. Ideally, the confusion matrix would result in values only on the diagonal. For example, the intersection cell of the 4th row and 4th column has a value of 0.81 which means that 81% of the 'excited' class were predicted correctly, or it can be said 81% of people are happy

with a particular celebrity according to the test data. These values are just counts based on only test data.

Fig. 8 Confusion Matrix for SVM

Results can be described in terms of the following:

1. **True Positive (TP):** Positive values were properly predicted as actual positive.
2. **False Positive (FP):** The predicted values were wrong in predicting a positive outcome.
3. **False Negative (FN):** Positive values were predicted as negative.
4. **True Negative (TN):** The predicted values were right in predicting a negative value.

A system is considered to be correct when it produces either true positives or true negatives. Incorrect performance occurs when the system generates False Positives or False Negatives. For example, we want to predict emotion for a sentence which is actually 'happy' type [29]. If the machine predicts emotion as 'happy' then it will be True Positive. Let's find TP, FP, FN, TN for a class say- 'abusive'.

$$TP = 3, TN = 531, FP = 2, FN = 43$$

Which says that 3 of 'abusive' class from test data were predicted correctly, 531 were predicted as True but not that specific class, 2 false predictions but class is true, 43 false predictions and also these were not that 'abusive' class.

4.2.2 Cross-Validation

It's not expected that a model will work correctly with real data it's never seen before. We need some assurance that the model has correctly identified the majority of the patterns in the dataset and is not overly sensitive to noise or has low bias and variance [29]. In order to get a static accuracy from SVM, we used cross-validation utilizing the K-fold algorithm, which allows for random sampling, and the stratified K-fold algorithm, which allows for stratified sampling.

We got an accuracy of 58% from K-Fold and 59% from Stratified K-Fold cross validation (Fig. 9) for the SVM classifier. This is lower than the accuracy we've mentioned previously but it is static and much more accurate. Stratified worked well on our imbalance dataset as it does not make folds randomly.

4.3 Limitations

Our paper works with five different emotions and in two categories. In total, we have seven different classes and those classes are Happy, Sad, Angry, Surprised, Excited, Religious, and Abusive. By using a data collection tool we have collected almost ten thousand data. However, only three thousand data are labeled according to our classes. A major portion of our data set remains unlabeled.

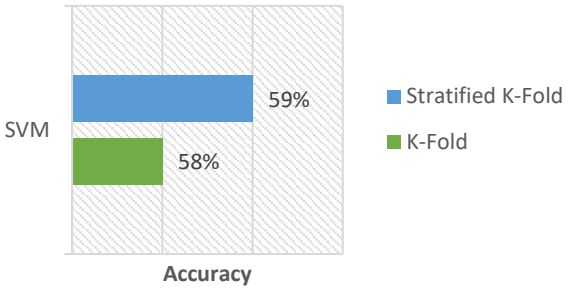

Fig. 9 Accuracy from K-Fold and Stratified K-Fold

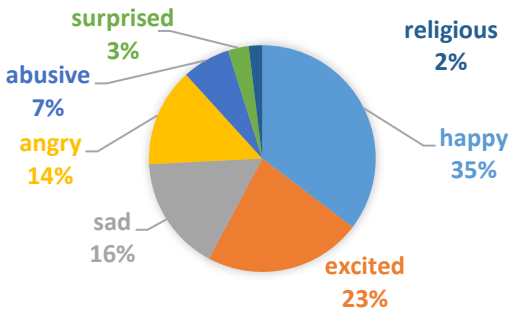

Fig. 10 Data Statistics

As a consequence, the required accuracy was not obtained according to our dataset. Due to the small dataset, Neural Network-based CNN and RNN algorithms were not used while these algorithms work well with larger datasets. Moreover, our dataset is not balanced. For seven different classes, we have different amounts of labeled data. Here, the dominating class is Happy. Almost 35% of data is labeled for the happy class, where only 2% of data is labeled for the Religious class as shown in Fig. 10. Due to a lack of balance data, we could not obtain higher accuracy.

5 Conclusion

Sentiment analysis is playing an essential role in revealing convenient information from people's opinions. It helps us to extract human emotions through speech, text, or even facial expressions. As a result, extracting viewpoints from text, speech, and facial expressions is a critical challenge in various fields, including social media tracking, product analysis, customer reviews analysis, clinical service analysis, and so on. Being inspired by these needs, this research paper works on extracting emotion from Bangla text. We know people nowadays are very involved in social media such and they are using social media to express their opinions on various matters. So, sentiment analysis can be helpful to gain a deeper understanding of people's views in order to provide better service. This study aimed to collect comments from different Facebook pages of Bangladeshi celebrities and develop a model that will be able to predict sentiment based on Bengali text. Our proposed methods can predict five other emotions from Bangla text, and we achieved 62% accuracy by using the Support Vector Machine (SVM) machine learning algorithm. Apart from this, our method is able to predict two different categories, such as Religious and

Abusive, which made our research work unique from other existing research work. In addition, the main reason for choosing SVM as the primary model is that it works better than other models such as Random Forest (RF), K-Nearest Neighbors (KNN), Naïve Bayes (NB), and Neural Network that is described in the previous section.

References

[1] Panksepp J., 2004. Affective neuroscience: The foundations of human and animal emotions. Oxford university press.

[2] Damasio A.R., 1998. Emotion in the perspective of an integrated nervous system. Brain research reviews, 26(2-3), pp.83-86.

[3] Ekman. P.E. and Davidson, R.J., 1994. The nature of emotion: Fundamental questions. Oxford University Press.

[4] Viking Mäntylä., M. Graziotin, D. and Kuutila M., 2016. The Evolution of Sentiment Analysis-A Review of Research Topics, Venues, and Top Cited Papers. arXiv e-prints, pp.arXiv-1612.

[5] Drovo, M.D., Chowdhury, M. Uday, S.I. and Das. A.K., 2019, June. Named entity recognition in bengali text using merged hidden markov model and rule base approach. In 2019 7th International Conference on Smart Computing & Communications (ICSCC) (pp. 1-5). IEEE.

[6] Hossain, M.T., Hasan, M.W. and Das, A.K., 2021, January. Bangla Handwritten Word Recognition System Using Convolutional Neural Network. In 2021 15th International Conference on Ubiquitous Information Management and Communication (IMCOM) (pp. 1-8). IEEE.

[7] Mumu, T.F., Munni, I.J. and Das, A.K., 2021. Depressed people detection from bangla social media status using lstm and cnn approach. Journal of Engineering Advancements, 2(01), pp.41-47.

[8] Islam, J., Mubassira, M., Islam, M.R. and Das, A.K., 2019, February. A speech recognition system for Bengali language using recurrent neural network. In 2019 IEEE 4th international conference on computer and communication systems (ICCCS) (pp. 73-76). IEEE.

[9] Mahmudun, M., Altaf, M.T. and Ismail, S., 2016. Detecting sentiment from Bangla text using machine learning technique and feature analysis. Int. J. Comput. Appl., 975, p.8887.

[10] Das, A. and Bandyopadhyay, S., 2010. Phrase-level polarity identification for Bangla. Int. J. Comput. Linguist. Appl.(IJCLA), 1(1-2), pp.169-182.

[11] Das, D., 2011, March. Analysis and tracking of emotions in english and bengali texts: a computational approach. In Proceedings of the 20th international conference companion on World wide web (pp. 343-348).

[12] Hasan, K.A. and Rahman, M., 2014, December. Sentiment detection from bangla text using contextual valency analysis. In 2014 17th International Conference on Computer and Information Technology (ICCIT) (pp. 292-295). IEEE.

[13] Chowdhury, S. and Chowdhury, W., 2014, May. Performing sentiment analysis in Bangla microblog posts. In 2014 International Conference on Informatics, Electronics & Vision (ICIEV) (pp. 1-6). IEEE.

[14] Go, A., Bhayani, R. and Huang, L., 2009. Twitter sentiment classification using distant supervision. CS224N project report, Stanford, 1(12), p.2009.

[15] Pandey, P. and Govilkar, S., 2015. A framework for sentiment analysis in Hindi using HSWN. International Journal of Computer Applications, 119(19).

[16] Tuhin, R.A., Paul, B.K., Nawrine, F., Akter, M. and Das, A.K., 2019, February. An automated system of sentiment analysis from bangla text using supervised learning techniques. In 2019 IEEE 4th International Conference on Computer and Communication Systems (ICCCS) (pp. 360-364). IEEE.

[17] Tembhurnikar, S.D. and Patil, N.N., 2015. Sentiment Analysis using LDA on Product Reviews: A Survey. International Journal of Computer Applications, 975, p.8887.

[18] Umamaheswari, K. and Karthiga, R., Sentiment Classification based on Latent Dirichlet Allocation. International Journal of Computer Applications, 975, p.8887.

[19] Das, A.K., Al Asif, A., Paul, A. and Hossain, M.N., 2021. Bangla hate speech detection on social media using attention-based recurrent neural network. Journal of Intelligent Systems, 30(1), pp.578-591.

[20] Datacamp.com, 2021. [Online]. Available: https://www.datacamp.com/community/tutorials/svm-classification-scikit-learn-python.

[21] Rakib, O.F., Akter, S., Khan, M.A., Das, A.K. and Habibullah, K.M., 2019, December. Bangla word prediction and sentence completion using GRU: an extended version of RNN on N-gram language model. In 2019 International Conference on Sustainable Technologies for Industry 4.0 (STI) (pp. 1-6). IEEE.

[22] Monkeylearn.com, 2021. [Online]. Available: https://monkeylearn.com/blog/what-is-tf-idf/

[23] "Support Vector Machine (SVM) Algorithm - Javatpoint", www.javatpoint.com, 2021. [Online]. Available: https://www.javatpoint.com/machine-learning-support-vector-machine-algorithm.

[24] Hossain, M.M., Labib, M.F., Rifat, A.S., Das, A.K. and Mukta, M., 2019, June. Auto-correction of english to bengali transliteration system using levenshtein distance. In 2019 7th International Conference on Smart Computing & Communications (ICSCC) (pp. 1-5). IEEE.

[25] Labib, M.F., Rifat, A.S., Hossain, M.M., Das, A.K. and Nawrine, F., 2019, June. Road accident analysis and prediction of accident severity by using machine learning in Bangladesh. In 2019 7th International Conference on Smart Computing & Communications (ICSCC) (pp. 1-5). IEEE.

[26] "Multilayer Perceptron (MLP) vs Convolutional Neural Network in Deep Learning", Medium, 2021. [Online]. Available: https://medium.com/data-science-bootcamp/multilayer-perceptron-mlp-vs-convolutional-neural-network-in-deep-learning-c890f487a8f1.

[27] Emon, E.A., Rahman, S., Banarjee, J., Das, A.K. and Mittra, T., 2019, June. A deep learning approach to detect abusive bengali text. In 2019 7th International Conference on Smart Computing & Communications (ICSCC) (pp. 1-5). IEEE.

[28] Ullah, M.R., Bhuiyan, M.A.R. and Das, A.K., 2017, September. IHEMHA: Interactive healthcare system design with emotion computing and medical history analysis. In 2017 6th International Conference on Informatics, Electronics and Vision & 2017 7th International Symposium in Computational Medical and Health Technology (ICIEV-ISCMHT) (pp. 1-8). IEEE.

[29] Bhuiyan, M., Rahman, A., Ullah, M. and Das, A.K., 2019. iHealthcare: Predictive model analysis concerning big data applications for interactive healthcare systems. Applied Sciences, 9(16), p.3365.

[30] "Confusion Matrix - an overview | ScienceDirect Topics", Sciencedirect.com, 2021. [Online]. Available: https://www.sciencedirect.com/topics/engineering/confusion-matrix.

[31] Das, A.K., Ashrafi, A. and Ahmmad, M., 2019, February. Joint cognition of both human and machine for predicting criminal punishment in judicial system. In 2019 IEEE 4th International Conference on Computer and Communication Systems (ICCCS) (pp. 36-40). IEEE.

SciEn
Journal of Engineering Advancements Vol. 02(03) 2021, pp 125-131 https://doi.org/10.38032/jea.2021.03.002

SVD-Krylov based Sparsity-preserving Techniques for Riccati-based Feedback Stabilization of Unstable Power System Models

Mahtab Uddin[*,1,3], *M. Monir Uddin*[2], *M. A. Hakim Khan*[3], *M. Tanzim Hossain*[4]

[1]Institute of Natural Sciences, United International University, Dhaka-1212, Bangladesh
[2]Department of Mathematics and Physics, North South University, Dhaka-1229, Bangladesh
[3]Department of Mathematics, Bangladesh University of Engineering & Technology, Dhaka-1000, Bangladesh
[4]Department of Electrical and Computer Engineering, North South University, Dhaka-1229, Bangladesh

Received: May 01, 2021, Revised: July 20, 2021, Accepted: July 24, 2021, Available Online: August 20, 2021

ABSTRACT

We propose an efficient sparsity-preserving reduced-order modelling approach for index-1 descriptor systems extracted from large-scale power system models through two-sided projection techniques. The projectors are configured by utilizing Gramian based singular value decomposition (SVD) and Krylov subspace-based reduced-order modelling. The left projector is attained from the observability Gramian of the system by the low-rank alternating direction implicit (LR-ADI) technique and the right projector is attained by the iterative rational Krylov algorithm (IRKA). The classical LR-ADI technique is not suitable for solving Riccati equations and it demands high computation time for convergence. Besides, in most of the cases, reduced-order models achieved by the basic IRKA are not stable and the Riccati equations connected to them have no finite solution. Moreover, the conventional LR-ADI and IRKA approach not preserves the sparse form of the index-1 descriptor systems, which is an essential requirement for feasible simulations. To overcome those drawbacks, the fitting of LR-ADI and IRKA based projectors from left and right sides, respectively, desired reduced-order systems attained. So that, finite solution of low-rank Riccati equations, and corresponding feedback matrix can be executed. Using the mechanism of inverse projection, the Riccati-based optimal feedback matrix can be computed to stabilize the unstable power system models. The proposed approach will maintain minimized $\mathfrak{H}_2$ -norm of the error system for reduced-order models of the target models.

Keywords: Singular Value Decomposition, Krylov Subspace, Alternative Direction Implicit, Riccati Equation, $\mathcal{H}_2$-norm, Optimal Feedback Stabilization.

1 Introduction

The index-1 descriptor systems of the first-order are conventionally the technical arrangement of sparse sub-matrices with appropriate structure. These sub-matrices are arranged in system-oriented input-output combinations. These systems can be formed as

$$\begin{aligned} E_{11}\dot{x_1}(t) &= A_{11}x_1(t) + A_{12}x_2(t) + B_1u(t), \\ 0 &= A_{21}x_1(t) + A_{22}x_2(t) + B_2u(t), \\ y(t) &= C_1x_1(t) + C_2x_2(t) + Du(t), \\ x(t_0) &= x_0, \quad t \geq t_0. \end{aligned} \tag{1}$$

In system (1), $E_{11} \in \mathbb{R}^{n_1 \times n_1}$ is the differential coefficient matrix, and $A_{11} \in \mathbb{R}^{n_1 \times n_1}$, $A_{12} \in \mathbb{R}^{n_1 \times n_2}$, $A_{21} \in \mathbb{R}^{n_2 \times n_1}$, $A_{22} \in \mathbb{R}^{n_2 \times n_2}$ are the state sub-matrices. The control multiplier sub-matrices $B_1 \in \mathbb{R}^{n_1 \times p}$, $B_2 \in \mathbb{R}^{n_2 \times p}$ with the state multiplier sub-matrices $C_1 \in \mathbb{R}^{m \times n_1}$, $C_2 \in \mathbb{R}^{m \times n_2}$. The direct gain matrix $D \in \mathbb{R}^{m \times p}$ is for the input to output transfer without alteration, it remains zero in many of the physical systems, for instance, power systems models. Here, the system dimension of the system (1) is $n = n_1 + n_2$ with the dimensions of input and output p and m, respectively. In the case of large-scale systems n is very large, whereas p, m are comparatively smaller. The vectors $x_1(t) \in \mathbb{R}^{n_1}$, $x_2(t) \in \mathbb{R}^{n_2}$ are for state vectors, whereas $u(t) \in \mathbb{R}^p$ and $y(t) \in \mathbb{R}^m$represent the input (control) and output vectors, respectively. The sub-matrices E_{11} and A_{22} have the full rank [1]-[2].

For further manipulation, $x_2(t) = -A_{22}^{-1}A_{21}x_1(t) - A_{22}^{-1}B_2u(t)$ needs to be eliminated from the algebraic (second) part of the Equation (1). Then the *Schur complements of the system* (1) can be formed as

$$\begin{aligned} x \coloneqq x_1, \quad \mathcal{E} \coloneqq E_{11}, \quad \mathcal{A} \coloneqq A_{11} - A_{12}A_{22}^{-1}A_{21}, \\ \mathcal{B} \coloneqq B_1 - A_{12}A_{22}^{-1}B_2, \mathcal{C} \coloneqq C_1 - C_2A_{22}^{-1}A_{21}, \\ \mathcal{D} \coloneqq D - C_2A_{22}^{-1}B_2. \end{aligned} \tag{2}$$

Using the Schur complements given in (2), the index-1 descriptor system (1) can structure into an analogous generalized LTI continuous-time system as

$$\begin{aligned} \mathcal{E}\dot{x}(t) &= \mathcal{A}x(t) + \mathcal{B}u(t), \\ y(t) &= \mathcal{C}x(t) + \mathcal{D}u(t). \end{aligned} \tag{3}$$

Applying Laplace transformation, the transfer function for the system (3) can be found as

$$G(s) = \mathcal{C}(s\mathcal{E} - \mathcal{A})^{-1}\mathcal{B} + \mathcal{D}; \quad s \in \mathbb{C}. \tag{4}$$

The implications of LTI continuous-time systems are inescapable in the branches of engineering fields with the applications of applied mathematics, for example, system and control theory, mechatronics, power electronics [3]-[5]. Continuous-time Algebraic Riccati Equation (CARE) plays a premier role in engineering applications, such as the systems that

*Corresponding Author Email Address: mahtab@ins.uiu.ac.bd

originated from mechanical and electrical fields [6]-[7] . The CARE yields from the system (3) can be formed as

$$\mathcal{A}^T X\mathcal{E} + \mathcal{E}^T X\mathcal{A} - \mathcal{E}^T X\mathcal{B}\mathcal{B}^T X\mathcal{E} + \mathcal{C}^T\mathcal{C} = 0. \qquad (5)$$

If all of the eigenvalues of the Hamiltonian matrix of the system (3) lie outside the imaginary axis, the solution X of the CARE (5) is then unique and finite [8]. The symmetric positive-definite Matrix X is called stabilizing if the closed-loop matrix $\mathcal{A} - (\mathcal{B}\mathcal{B}^T)X\mathcal{E}$ exists and is stable. Some of the systems, that have eigenvalues very close to the imaginary axis are called semi-stable systems. For an unstable type of system (3), the optimal feedback matrix $K^o = \mathcal{B}^T X\mathcal{E}$ needs to estimate to apply the Riccati-based feedback stabilization [9]. Implementing the desired K^o, the matrix $\mathcal{A}_s = \mathcal{A} - BK^o$ can be formed to replace the system matrix $\mathcal{A}$. Then the optimally stabilized target system can be written as

$$\begin{aligned} \mathcal{E}\dot{x}(t) &= \mathcal{A}_s x(t) + \mathcal{B}u(t), \\ y(t) &= \mathcal{C}x(t) + \mathcal{D}u(t). \end{aligned} \qquad (6)$$

In the previous works, we have discussed the rational Krylov subspace method (RKSM) and the Kleinman-Newton technique for the Riccati-based feedback stabilization technique for unstable index-1 descriptor systems [10]-[11]. The linear quadratic regulator (LQR) approach is the key of the RKSM and the low-rank Cholesky-factor integrated alternative direction implicit (LRCF-ADI) approach requires in the Kleinman-Newton technique. A modified form of the iterative rational Krylov algorithm (IRKA) technique was recently derived to treat that of the systems through optimal feedback stabilization [12]. In those works, some unstable systems extracted from the Brazilian Interconnected Power System (BIPS) models are deliberated to stabilize.

In this work, we introduce two-sided projection techniques for Riccati-based feedback stabilization for unstable BIPS models utilizing reduced-order modeling, which is a coupled approach of singular value decomposition and Krylov subspace and naming as Iterative SVD-Krylov Algorithm (ISKA). The reduced-order models will be validated through the $\mathcal{H}_2$ norm of the error system. Comparative discussion on the present work and IRKA approaches will be done.

2 Preliminaries

The Lyapunov equation consisting of observability Gramian $\mathcal{Q}$ of the system (3) has the form

$$\mathcal{A}^T\mathcal{Q}\mathcal{E} + \mathcal{E}^T\mathcal{Q}\mathcal{A} + \mathcal{C}^T\mathcal{C} = 0. \qquad (7)$$

Computation of the $\mathcal{Q}$ by solving the Equation (7) containing large-scale matrices by the direct solvers is infeasible for the large-scale systems, sometimes it may impossible for the rising size of the system components. Thus, the observability Gramian factor Z_q needs to be estimated by any feasible approach. There are some efficient techniques available for executing Z_q, for example, low-rank Cholesky-factor-based Alternating Direction Implicit (LRCF-ADI) [13]-[14]. Then the Gramian, $\mathcal{Q} = Z_q Z_q^T$ can be approximated as the solution of the Lyapunov Equation (7). The LRCF-ADI approach for computing Z_q is provided in Algorithm 1.

Algorithm 1: First-order LRCF-ADI Algorithm [13]

Input: $\mathcal{E}, \mathcal{A}, \mathcal{B}, \mathcal{C}, \tau$ (tolerance), i_{max} (iterations), and $\{\mu_j\}_{j=1}^{i_{max}}$ (initial shifts).

Output: Low-rank Cholesky-factor Z_q for $\mathcal{Q} = Z_q Z_q^T$.

Assume at $i = 1, Z_0 = [\,]$ and $W_0 = \mathcal{C}^T$.
while $\|\mathcal{W}_{i-1}\mathcal{W}_{i-1}^T\| \geq \tau$ or $i \leq i_{max}$ **do**
  Solve $\mathcal{V}_i = (\mathcal{A}^T + \mu_i\mathcal{E}^T)^{-1}\mathcal{W}_{i-1}$.
  if $Im(\mu_i) = 0$ **then**
    Update $Z_i = \begin{bmatrix} Z_{i-1} & \sqrt{-2\mu_i}\mathcal{V}_i \end{bmatrix}$,
    Compute $\mathcal{W}_i = \mathcal{W}_{i-1} - 2\mu_i\mathcal{E}^T\mathcal{V}_i$.
  else
    Assume $\gamma_i = \sqrt{-2Re(\mu_i)}, \quad \delta_i = \frac{Re(\mu_i)}{Im(\mu_i)}$,
    Update $Z_{i+1} = \begin{bmatrix} Z_{i-1} & \gamma_i(Re(\mathcal{V}_i) + \delta_i Im(\mathcal{V}_i)) & \gamma_i\sqrt{\delta_i^2 + 1}Im(\mathcal{V}_i) \end{bmatrix}$,
    Compute, $\mathcal{W}_{i+1} = \mathcal{W}_{i-1} - 4Re(\mu_i)\mathcal{E}^T[Re(\mathcal{V}_i) + \delta_i Im(\mathcal{V}_i)]$.
    $i = i + 1$
  end if
  $i = i + 1$
end while

Considering the computationally feasible r-dimensional reduced-order model (ROM) of the system (3) as

$$\begin{aligned} \hat{\mathcal{E}}\dot{\hat{x}}(t) &= \hat{\mathcal{A}}\hat{x}(t) + \hat{\mathcal{B}}\hat{u}(t), \\ \hat{y}(t) &= \hat{\mathcal{C}}\hat{x}(t) + \hat{\mathcal{D}}\hat{u}(t), \end{aligned} \qquad (8)$$

where $\hat{\mathcal{E}} \in \mathbb{R}^{r\times r}$, $\hat{\mathcal{A}} \in \mathbb{R}^{r\times r}$, $\hat{\mathcal{B}} \in \mathbb{R}^{r\times p}$, $\hat{\mathcal{C}} \in \mathbb{R}^{m\times r}$ and $\hat{\mathcal{D}} \in \mathbb{R}^{m\times p}$.

The reduced coefficient matrices of (8) are formed by the following way

$$\begin{aligned} \hat{\mathcal{E}} = W^T\mathcal{E}V, \quad \hat{\mathcal{A}} = W^T\mathcal{A}V, \quad \hat{\mathcal{B}} = W^T\mathcal{B}, \\ \hat{\mathcal{C}} = \mathcal{C}V, \quad \hat{\mathcal{D}} = \mathcal{D}. \end{aligned} \qquad (9)$$

The transfer function of the ROM (8) can be found as

$$\hat{G}(s) = \hat{\mathcal{C}}\left(s\hat{\mathcal{E}} - \hat{\mathcal{A}}\right)^{-1}\hat{\mathcal{B}} + \hat{\mathcal{D}}; \quad s \in \mathbb{C}. \qquad (10)$$

The right projector V is built by the well-known Krylov-based interpolatory techniques IRKA given in [15]-[16] as

$$V = [(\alpha_1\mathcal{E} - \mathcal{A})^{-1}\mathcal{B}b_1, \ldots, (\alpha_r\mathcal{E} - \mathcal{A})^{-1}\mathcal{B}b_r\,], \qquad (11)$$

where $\{\alpha_i\}_{i=1}^r$ and $\{b_i\}_{i=1}^r$ are the interpolation points and tangential direction respectively. The left projector W is computed by the observability Gramian $\mathcal{Q}$ utilizing the singular value decomposition-based techniques discussed in [17]-[19] as

$$W = \mathcal{Q}V(V^T\mathcal{Q}V)^{-1}. \qquad (12)$$

The successive steps of the computation of the ROM (8) are exhibited in Algorithm 2.

Algorithm 2: First-order ISKA [17]

Input: $\mathcal{E}, \mathcal{A}, \mathcal{B}, \mathcal{C}, \mathcal{D}$ and Z_q (from Algorithm 1).

Output: $\hat{\mathcal{E}}, \hat{\mathcal{A}}, \hat{\mathcal{B}}, \hat{\mathcal{C}}, \hat{\mathcal{D}} := \mathcal{D}$.

1 Choose the initial interpolation points $\{\alpha_i\}_{i=1}^{r}$ and the tangential directions $\{b_i\}_{i=1}^{r}$.
2 Construct $V = [(\alpha_1\mathcal{E} - \mathcal{A})^{-1}\mathcal{B}b_1, \dots, (\alpha_r\mathcal{E} - \mathcal{A})^{-1}\mathcal{B}b_r\ ]$.
3 Compute $\mathcal{Q} = Z_q Z_q^T$ and construct $W = \mathcal{Q}V(V^T\mathcal{Q}V)^{-1}$.
4 **while** $(not\ converged)$ **do**
5 Find $\hat{\mathcal{E}} = W^T\mathcal{E}V,\ \hat{\mathcal{A}} = W^T\mathcal{A}V,\ \hat{\mathcal{B}} = W^T\mathcal{B},\ \hat{\mathcal{C}} = \mathcal{C}V$.
6 **for** $i = 1, \dots, r$. **do**
7 Evaluate $\hat{\mathcal{A}}z_i = \lambda_i\hat{\mathcal{E}}z_i$ and $y_i^*\hat{\mathcal{A}} = \lambda_i y_i^*\hat{\mathcal{E}}$ to find $\alpha_i \longleftarrow -\lambda_i, b_i^* \longleftarrow -y_i^*\hat{\mathcal{B}}$.
8 **end for**
9 Repeat Step-2 and Step-3.
10 $i = i + 1$
11 **end while**
12 Repeat Step-5 to find the reduced-order matrices.

3 Sparsity-preserving SVD-Krylov techniques for the stabilization of first-order index-1 descriptor system

The objective of this work is to reduce the dimension of the first-order index-1 system (1) by keeping the sparse structure invariant through the Iterative SVD-Krylov Algorithm (ISKA) approach. To do this, it is essential to modify some steps of first-order ISKA and LRCF-ADI algorithms in terms of sparse sub-matrices.

3.1 Sparsity-preserving LRCF-ADI approach for the first-order index-1 descriptor system

The LRCF-ADI method of first-order was discussed in [13],[20]-[21]. The modification of the LRCF-ADI algorithm for the structure-preserving second-order form can be derived as follows.

For the truncated term Γ, the first iteration of the Step-3 of Algorithm 1 can be written as

$$(\mathcal{A}^T + \mu_1\mathcal{E}^T)\mathcal{V}_1 = \mathcal{C}^T,$$
$$or, \left(\begin{bmatrix} A_{11} & A_{12} \\ A_{21} & A_{22} \end{bmatrix}^T + \mu_1 \begin{bmatrix} E_{11} & 0 \\ 0 & 0 \end{bmatrix}^T\right)\begin{bmatrix} \mathcal{V}_1 \\ \Gamma \end{bmatrix} = \begin{bmatrix} C_1^T \\ C_2^T \end{bmatrix}. \quad (13)$$

Thus, we have

$$\begin{bmatrix} A_{11}^T + \mu_1 E_{11}^T & A_{21}^T \\ A_{12}^T & A_{22}^T \end{bmatrix}\begin{bmatrix} \mathcal{V}_1 \\ \Gamma \end{bmatrix} = \begin{bmatrix} C_1^T \\ C_2^T \end{bmatrix}. \quad (14)$$

As a consequence, for $i \geq 2$, the next $i - th$ iteration takes the form

$$\begin{bmatrix} A_{11}^T + \mu_i E_{11}^T & A_{21}^T \\ A_{12}^T & A_{22}^T \end{bmatrix}\begin{bmatrix} \mathcal{V}_i \\ \Gamma \end{bmatrix} = \begin{bmatrix} \mathcal{W}_{i-1} \\ 0 \end{bmatrix}. \quad (15)$$

If the estimated shift parameter has no imaginary part, then the Step-6 of Algorithm 1 can be formed as

$$\mathcal{W}_i = \mathcal{W}_{i-1} - 2\mu_i E_{11}^T\mathcal{V}_i. \quad (16)$$

Otherwise, for $\delta_i = \frac{Re(\mu_i)}{Im(\mu_i)}$, the Step-10 of Algorithm 1 can be expressed as

$$\mathcal{W}_{i+1} = \mathcal{W}_{i-1} - 4Re(\mu_i)E_{11}^T[Re(\mathcal{V}_i) + \delta_i Im(\mathcal{V}_i)]. \quad (17)$$

The restructured sparse form of LRCF-ADI for the first-order index-1 system is exhibited in Algorithm 3.

Algorithm 3: LRCF-ADI for first-order sparse index-1 descriptor system

Input: $E_{11}, A_{11}, A_{12}, A_{21}, A_{22}, B_1, B_2, C_1, C_2, \tau$ (tolerance), i_{max} (iterations), and $\{\mu_j\}_{j=1}^{i_{max}}$ (initial shifts).

Output: Low-rank Cholesky-factor Z_q for $\mathcal{Q} \approx Z_q Z_q^T$.

1 Assume at $i = 1, Z_0 = [\ ]$ and $\mathcal{W}_0 = [C_1 \quad C_2]^T$.
2 **while** $\|\mathcal{W}_{i-1}\mathcal{W}_{i-1}^T\| \geq \tau$ or $i \leq i_{max}$ **do**
3 Solve (14) to find $\mathcal{V}_1$ and (15) to find $\mathcal{V}_i\ ;\ i \geq 2$.
4 **if** $Im(\mu_i) = 0$ **then**
5 Update $Z_i = [Z_{i-1} \quad \sqrt{-2\mu_i}\mathcal{V}_i]$,
6 Compute the updated value of $\mathcal{W}_i$ by (16)
7 **else**
8 Assume $\gamma_i = \sqrt{-2Re(\mu_i)}, \quad \delta_i = \frac{Re(\mu_i)}{Im(\mu_i)}$,
9 Update $Z_{i+1} = \left[Z_{i-1} \quad \gamma_i(Re(\mathcal{V}_i) + \delta_i Im(\mathcal{V}_i)) \quad \gamma_i\sqrt{\delta_i^2 + 1}Im(\mathcal{V}_i)\right]$,
10 Compute the updated value of $\mathcal{W}_{i+1}$ by (17).
11 $i = i + 1$
12 **end if**
13 $i = i + 1$
14 **end while**

3.2 Sparsity-preserving ISKA for first-order index-1 descriptor system

Algorithm 2 needs to reform in the sparse form with the system matrices of (1). In the Step-2 of this algorithm, projector V needs to be re-structured utilizing the first-order sparse matrices. Let us consider the $i - th$ iteration of V be expressed as V_i and it can be configured as

$$(\alpha_i\mathcal{E} - \mathcal{A})V_i = \mathcal{B}b_i, \quad (18)$$
$$or, \begin{bmatrix} \alpha_i E_{11} - A_{11} & -A_{12} \\ -A_{21} & -A_{22} \end{bmatrix}\begin{bmatrix} V_i \\ \Lambda \end{bmatrix} = \begin{bmatrix} B_1 \\ B_2 \end{bmatrix} b_i.$$

The term Λ is to be truncated. The explicit execution of the reduced-order matrices for the system (8) defined in (9) is infeasible and contradicts the aim of the work.

The reduced-order matrices can be efficiently acquired by the sparsity preserving form as

$$\hat{\mathcal{E}} = W^T E_{11}V, \quad \hat{A} = W^T A_{11}V - (W^T A_{12})A_{22}^{-1}(A_{21}V),$$
$$\hat{B} = W^T B_1 - (W^T A_{12})A_{22}^{-1}B_2, \quad (19)$$
$$\hat{C} = C_1 V - C_2 A_{22}^{-1}(A_{21}V).$$

The sparsity-preserving modified form of Algorithm 2 for the first-order index-1 system is summarized in Algorithm 4.

Algorithm 4: ISKA for first-order sparse index-1 descriptor system

Input: $E_{11}, A_{11}, A_{12}, A_{21}, A_{22}, B_1, B_2, C_1, C_2, D$ and Z_q (from Algorithm 3).

Output: $\hat{\mathcal{E}}, \hat{\mathcal{A}}, \hat{\mathcal{B}}, \hat{\mathcal{C}}, \hat{\mathcal{D}} := D - C_2 A_{22}^{-1} B_2$.

1. Choose the initial interpolation points $\{\alpha_i\}_{i=1}^{r}$ and the tangential directions $\{b_i\}_{i=1}^{r}$.
2. Construct $V = [V_1, V_2, \dots, V_r]$ using (18).
3. Compute $\mathcal{Q} = Z_q Z_q^T$ and construct $W = \mathcal{Q}V(V^T\mathcal{Q}V)^{-1}$.
4. **while** $(not\ converged)$ **do**
5. Find the reduced-order matrices by (19).
6. **for** $i = 1, \dots, r$. **do**
7. Evaluate $\hat{\mathcal{A}} z_i = \lambda_i \hat{\mathcal{E}} z_i$ and $y_i^* \hat{\mathcal{A}} = \lambda_i y_i^* \hat{\mathcal{E}}$ to find $\alpha_i \longleftarrow -\lambda_i, b_i^* \longleftarrow -y_i^* \hat{\mathcal{B}}$.
8. **end for**
9. Repeat Step-2 and Step-3.
10. $i = i + 1$
11. **end while**
12. Repeat Step-5 to find the reduced-order matrices.

3.3 Computing the optimal feedback matrix from ROM

System (3) can be written in a reduced-order form as (8) by exerting the reduced-order matrices defined in (19) and corresponding CARE can be attained as

$$\hat{\mathcal{A}}^T \hat{X} \hat{\mathcal{E}} + \hat{\mathcal{E}} \hat{X} \hat{\mathcal{A}} - \hat{\mathcal{E}} \hat{X} \hat{\mathcal{B}} \hat{\mathcal{B}}^T \hat{X} \hat{\mathcal{E}} + \hat{\mathcal{C}}^T \hat{\mathcal{C}} = 0. \qquad (20)$$

Here $\hat{X}$ has the same properties of X. The MATLAB library command *care* can be applied to solve the low-rank CARE (20). The low-rank stabilizing feedback matrix $\hat{K} = \hat{\mathcal{B}}^T \hat{X} \hat{\mathcal{E}}$ corresponding to the ROM (8) can be computed, and consequently approximated the stabilizing optimal feedback matrix K^o of the full model (3) can be reclaimed employing the scheme of reverse projection as

$$K^o = (\hat{\mathcal{B}}^T \hat{X} \hat{\mathcal{E}}) V^T E_{11} = \hat{K} V^T E_{11}. \qquad (21)$$

3.4 Optimally stabilized first-order index-1 descriptor system

For the original system (1), optimal feedback matrix K^o can be attained by assigning the ROM (8). Then by utilizing K^o, the optimally stabilized system (1) can be found by replacing A_{11} and A_{21} by $A_{11} - B_1 K^o$ and $A_{21} - B_2 K^o$, respectively

3.5 $\mathcal{H}_2$-norm of the error system

Now, the error system associated with the ROM (8) of the subjected system (1) by maintaining the form (3) has the form

$$G_{err} = G(s) - \hat{G}(s) = \mathcal{C}_{err}(s\mathcal{E}_{err} - \mathcal{A}_{err})^{-1} B_{err}, \qquad (22)$$

where the transfer functions $G(s)$ and $\hat{G}(s)$ are connected to the systems (1) and (8), respectively. In (22), we have constituted

$$\mathcal{E}_{err} = \begin{bmatrix} \mathcal{E} & 0 \\ 0 & \hat{\mathcal{E}} \end{bmatrix}, \quad \mathcal{A}_{err} = \begin{bmatrix} \mathcal{A} & 0 \\ 0 & \hat{\mathcal{A}} \end{bmatrix}, \qquad (23)$$
$$\mathcal{B}_{err} = \begin{bmatrix} \mathcal{B} \\ \hat{\mathcal{B}} \end{bmatrix} \quad and \quad \mathcal{C}_{err} = [\mathcal{C} \quad -\hat{\mathcal{C}}].$$

The observability Lyapunov equation corresponding to the Graminan $\mathcal{Q}_{err}$ of the error system (22) is

$$\mathcal{A}_{err}^T \mathcal{Q}_{err} \mathcal{E}_{err} + \mathcal{E}_{err}^T \mathcal{Q}_{err} \mathcal{A}_{err} + \mathcal{C}_{err}^T \mathcal{C}_{err} = 0. \qquad (24)$$

For the error system (22), the Authors in [5] explored an efficient approach to approximate the $\mathcal{H}_2$-norm as

$$\|G_{err}\|_{\mathcal{H}_2} = \sqrt{trace(\mathcal{B}_{err}^T \mathcal{Q}_{err} \mathcal{B}_{err})} \qquad (25)$$
$$= \sqrt{\|G(s)\|_{\mathcal{H}_2}^2 + \|\hat{G}(s)\|_{\mathcal{H}_2}^2 + 2trace(\mathcal{B}^T \mathcal{Q}_s \hat{\mathcal{B}})}$$

Here, $\|G(s)\|_{\mathcal{H}_2}$ is the $\mathcal{H}_2$-norm of the full model which we need to evaluate at one time in computation but this is unfeasible to investigate for a large-scale system by any direct solver. Suppose Z_q is the low-rank Gramian factor that can be successfully determined by rearranging Algorithm 3, such that $\mathcal{Q} = Z_q Z_q^T$, then $\|G(s)\|_{\mathcal{H}_2}$ can be written as

$$\|G(s)\|_{\mathcal{H}_2}^2 = trace(\mathcal{B}^T \mathcal{Q} \mathcal{B}) \qquad (26)$$
$$= trace\left(B_1^T (Z_q Z_q^T) B_1 + B_2^T (Z_q Z_q^T) B_2\right).$$

Again, the $\mathcal{H}_2$-norm of the ROM, $\|\hat{G}(s)\|_{\mathcal{H}_2}$ can be enumerated by the Gramian $\hat{\mathcal{Q}}$ of the low-rank Lyapunov equation

$$\hat{\mathcal{A}}^T \hat{\mathcal{Q}} \hat{\mathcal{E}} + \hat{\mathcal{E}}^T \hat{\mathcal{Q}} \hat{\mathcal{A}} + \hat{\mathcal{C}}^T \hat{\mathcal{C}} = 0, \qquad (27)$$

that consists of reduced-order matrices. Due to the small size of these matrices, the following Lyapunov equation is solvable by the MATLAB library command *lyap*.

Finally, $\text{trace}(\mathcal{B}^T \mathcal{Q}_s \hat{\mathcal{B}})$ can be measured by the low-rank Gramian $\mathcal{Q}_s$ of the sparse-dense Sylvester equation

$$\mathcal{A}^T \mathcal{Q}_s \hat{\mathcal{E}} + \mathcal{E}^T \mathcal{Q}_s \hat{\mathcal{A}} + \mathcal{C}^T \hat{\mathcal{C}} = 0, \qquad (28)$$

that can be efficiently solved by the techniques presented in Algorithm 4 of [22].

4 Numerical results

The derived method ISKA is validated by implementing some models evolved from Brazilian Interconnected Power System (BIPS) [23]. The computations are performed numerically by MATLAB® R2015a (8.5.0.197613) with a processor $4 \times \text{Intel}^{®}\text{Core}^{\text{TM}}\text{i5} - 6200\text{U}$ incorporating a memory capacity of 16 GB with a clock speed of 2.30 GHz.

Table 1 displays the dimensions of the discussing models along with analogous input-output structures, and the size of the corresponding ROMs gained by the developed technique ISKA as illustrated in Algorithm 4.

Table 1 Model examples with input-output structures

Model	Full model (n)	Input/Output	ROM (r)
BIPS-606	7135	4/4	30
BIPS-1998	15066	4/4	70
BIPS-2476	16861	4/4	100
BIPS-3078	21128	4/4	120

The models are named on the number of the states they consist of [24]. Detailed of those models are available on the web-page.

In the previous work [12], it is found that IRKA based reduced-order model for the semi-stable model BIPS-3078 has no finite solution of the corresponding Riccati equation but the ISKA approach has no such kind of limitation.

4.1 Frequency domain analysis

All the above-mentioned power system models are structurally identical and have the same physical attributes. For the compactness of the work, only the comparative analysis of the transfer function of model BIPS-3078 is provided.

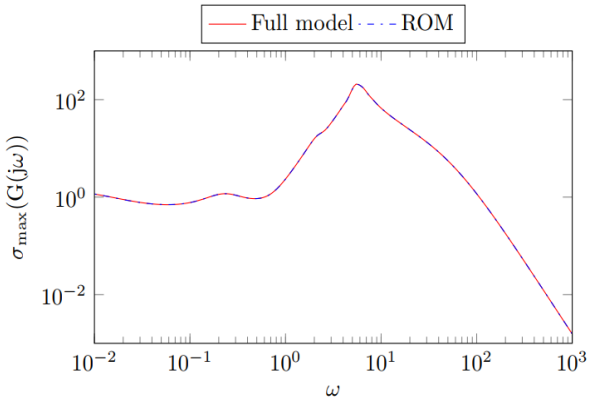

(a) Sigma plot

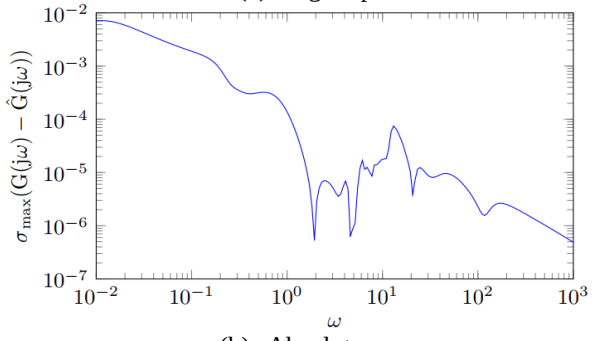

(b) Absolute error

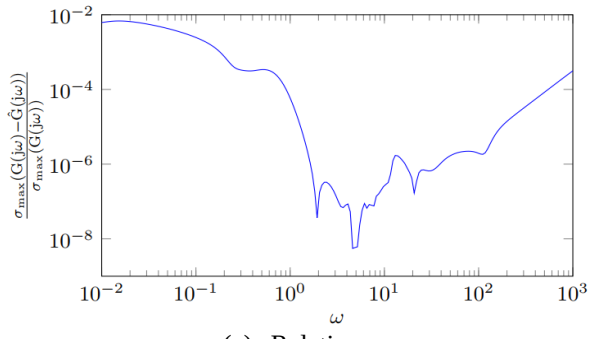

(c) Relative error

Fig. 1 Comparison of full model and ROM of the model BIPS-3078

Sub-figures of Fig. 1 gives graphical validation of the efficient match of the transfer function of model BIPS-3078 with the corresponding ISKA-based ROM. Fig. 1a displays comparison transfer functions, whereas Fig. 1b and Fig. 1c depict the absolute error and relative error in computing the ROM of the target model.

From the above-displaying figures, it can be said that the ISKA-based approach is efficient for finding desired ROM of the target model.

4.2 Stability analysis

Sub-figures of Fig. 2 exhibit the stabilized step-responses of the model BIPS-3078 for the dominant input-output relations.

From the foregoing figures, it has been seen that in every input-output relation, the step-responses of the model BIPS-3078 optimally stabilized.

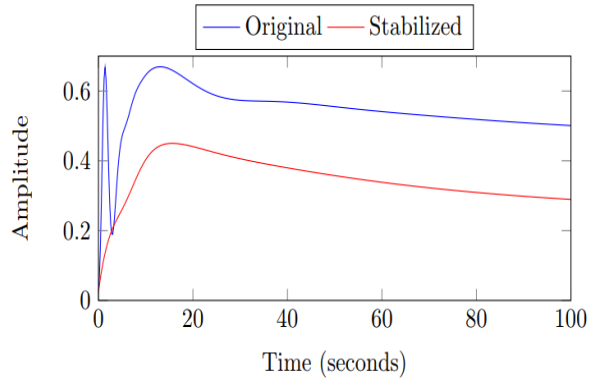

(a) 1st input / 4th input

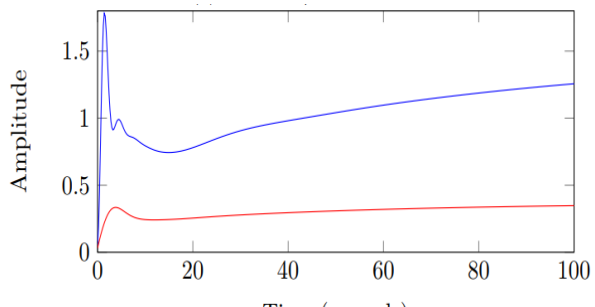

(b) 2nd input / 1st input

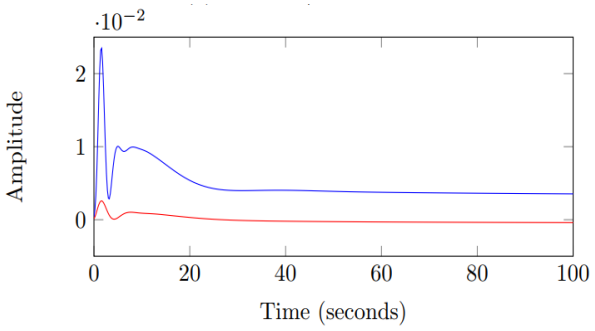

(c) 3rd input / 2nd input

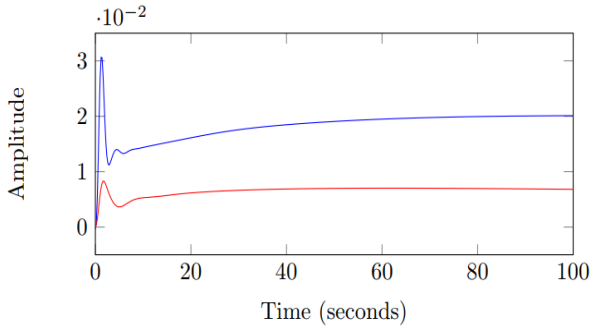

(d) 4th input / 3rd input

Fig. 2 Stabilization of step-responses of the model BIPS-3078

From the aforesaid figures, it is revealed that the eigenvalues of the models BIPS-606, BIPS-1998, and BIPS-2476 are stabilized efficiently.

Sub-figures of Fig. 3 demonstrate the optimal feedback stabilization of the eigenvalues of the BIPS models.

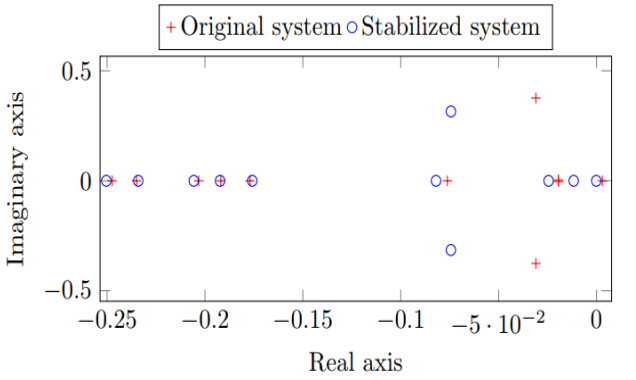

(a) BIPS-606

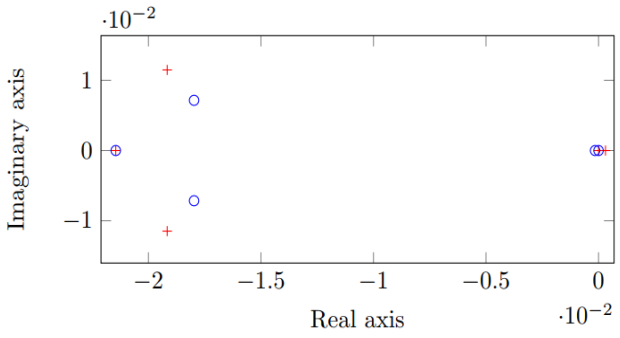

(b) BIPS-1998

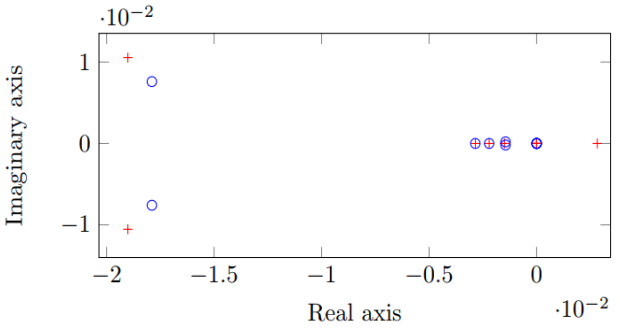

(c) BIPS-2476

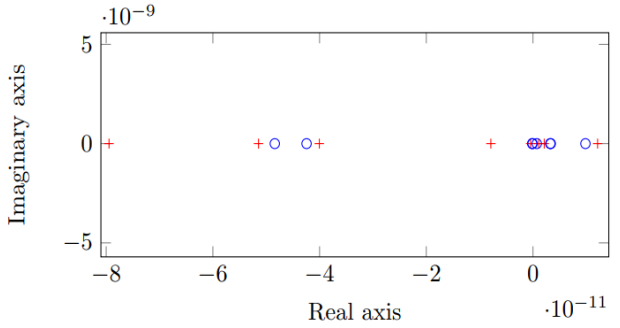

(d) BIPS-3078

Fig. 3 Eigenvalue stabilization of BIPS models

But the stabilization process for the semi-stable model BIPS-3078 is mildly interrupted but still acceptable as the eigenvalues are in the very small neighborhood of the imaginary axis (a very magnified view is provided).

4.3 $\mathcal{H}_2$-norm comparisons

Table 2 represents the $\mathcal{H}_2$ error norm of the full model and the corresponding ROM of the BIPS models. This table is numerical evidence of the robustness of the proposed approach.

Table 2 $\mathcal{H}_2$ error norm the of the full models and the ROMs

Model	BIPS-606	BIPS-1998	BIPS-2476	BIPS-3078
$\mathcal{H}_2$ error norm	2.16×10^{0}	1.22×10^{-2}	4.34×10^{-4}	2.05×10^{-4}

It has been audited that the $\mathcal{H}_2$ error norms are decreasing with the increasing size of the target models. Thus, the ISKA approach is expedient to minimize the $\mathcal{H}_2$ error norms of the considering models and it gives a better approximation for the models of the larger size.

5 Conclusion

We have discussed a sparsity-preserving two-sided projection-based reduced-order modelling approach for index-1 descriptor systems of the first-order form. The Gramian based singular value decomposition and Krylov-based reduced-order modelling are coupled to achieve the reduced-order models. The conventional first-order LRCF-ADI and ISKA algorithms are modified to the sparse form keeping the structure of the target systems invariant. The proposed techniques are devoted to the Riccati-based feedback stabilization of the target systems. We have tested the validity of the proficiency of the derived approaches by implementing them to the power system models of the type unstable index-1 descriptor system in the first-order form. The robustness is investigated by $\mathcal{H}_2$ error norms of the reduced-order models corresponding to the target models.

6 Acknowledgment

The work is supported by Institute for Advanced Research (IAR), United International University, Dhaka, Bangladesh. The project title is *"Computation of Optimal Control for Differential-Algebraic Equations (DAE) with Engineering Applications"* with the reference IAR/01/19/SE/18.

References

[1] Hossain, M.S. and Uddin, M.M., 2019. Iterative methods for solving large sparse Lyapunov equations and application to model reduction of index 1 differential-algebraic equations. *Numerical Algebra, Control & Optimization*, *9*(2), p.173.

[2] Benner, P., Saak, J. and Uddin, M.M., 2016, December. Reduced-order modeling of index-1 vibrational systems using interpolatory projections. In *2016 19th International Conference on Computer and Information Technology (ICCIT)* (pp.134-138). IEEE.

[3] Uddin, M.M., 2015. *Computational methods for model reduction of large-scale sparse structured descriptor systems* (Doctoral dissertation, Otto-von Guericke Universität Magdeburg).

[4] Benner, P., Saak, J. and Uddin, M.M., 2016. Structure preserving model order reduction of large sparse second-order index-1 systems and application to a mechatronics

model. *Mathematical and Computer Modelling of Dynamical Systems*, *22*(6), pp.509-523.

[5] Rahman, M., Uddin, M.M., Andallah, L.S. and Uddin, M., 2020. Interpolatory Projection Techniques for $\mathcal{H}_2$ Optimal Structure-Preserving Model Order Reduction of Second-Order Systems. *Advances in Science, Technology and Engineering Systems Journal*, *5*(4), pp.715-723.

[6] Chu, E.K.W., 2011, August. Solving large-scale algebraic Riccati equations by doubling. In *Talk presented at the Seventeenth Conference of the International Linear Algebra Society, Braunschweig, Germany* (Vol. 22).

[7] Chen, W. and Qiu, L., 2015. Linear quadratic optimal control of continuous-time LTI systems with random input gains. *IEEE Transactions on Automatic Control*, *61*(7), pp.2008-2013.

[8] Abou-Kandil, H., Freiling, G., Ionescu, V. and Jank, G., 2012. *Matrix Riccati equations in control and systems theory*. Birkhäuser.

[9] Bänsch, E., Benner, P., Saak, J. and Weichelt, H.K., 2015. Riccati-based boundary feedback stabilization of incompressible Navier-Stokes flows. *SIAM Journal on Scientific Computing*, *37*(2), pp.A832-A858.

[10] Uddin, M., Khan, M.A.H. and Uddin, M.M., 2019, September. Riccati based optimal control for linear quadratic regulator problems. In *2019 5th International Conference on Advances in Electrical Engineering (ICAEE)* (pp.290-295). IEEE.

[11] Uddin, M., Khan, M.A.H. and Uddin, M.M., 2019, December. Efficient computation of Riccati-based optimal control for power system models. In *2019 22nd International Conference on Computer and Information Technology (ICCIT)* (pp.260-265). IEEE.

[12] Uddin, M., Uddin, M.M., Khan, M.A.H. and Rahman, M.M., 2021. Interpolatory projection technique for Riccati-based feedback stabilization of index-1 descriptor systems. *IOP Conference Series: Materials Science and Engineering*, *1070*(1), pp.12-22.

[13] Li, J.R., 2000. *Model reduction of large linear systems via low rank system Gramians* (Doctoral dissertation, Massachusetts Institute of Technology).

[14] Hossain, M.S., Omar, S.G., Tahsin, A. and Khan, E.H., 2017, September. Efficient system reduction modeling of periodic control systems with application to circuit problems. In *2017 4th International Conference on Advances in Electrical Engineering (ICAEE)* (pp. 259-264). IEEE.

[15] Gugercin, S., Antoulas, A.C. and Beattie, C., 2008. H_2 model reduction for large-scale linear dynamical systems. *SIAM journal on matrix analysis and applications*, *30*(2), pp.609-638.

[16] Wyatt, S.A., 2012. *Issues in interpolatory model reduction: Inexact solves, second-order systems and DAEs* (Doctoral dissertation, Virginia Tech).

[17] Gugercin, S., 2008. An iterative SVD-Krylov based method for model reduction of large-scale dynamical systems. *Linear Algebra and its Applications*, *428*(8-9), pp.1964-1986.

[18] Khatibi, M., Zargarzadeh, H. and Barzegaran, M., 2016, September. Power system dynamic model reduction by means of an iterative SVD-Krylov model reduction method. In *2016 IEEE Power & Energy Society Innovative Smart Grid Technologies Conference (ISGT)* (pp.1-6). IEEE.

[19] Li, S., Trevelyan, J., Wu, Z., Lian, H., Wang, D. and Zhang, W., 2019. An adaptive SVD–Krylov reduced order model for surrogate based structural shape optimization through isogeometric boundary element method. *Computer Methods in Applied Mechanics and Engineering*, *349*, pp.312-338.

[20] Lu, A. and Wachspress, E.L., 1991. Solution of Lyapunov equations by alternating direction implicit iteration. *Computers & Mathematics with Applications*, *21*(9), pp.43-58.

[21] Benner, P., Li, J.R. and Penzl, T., 2008. Numerical solution of large-scale Lyapunov equations, Riccati equations, and linear-quadratic optimal control problems. *Numerical Linear Algebra with Applications*, *15*(9), pp.755-777.

[22] Benner, P., Køhler, M. and Saak, J., 2011. Sparse-dense Sylvester equations in $\mathcal{H}_2$ model order reduction.

[23] Freitas, F.D. and Costa, A.S., 1999. Computationally efficient optimal control methods applied to power systems. *IEEE transactions on power systems*, *14*(3), pp.1036-1045.

[24] Leandro, R.B., e Silva, A.S., Decker, I.C. and Agostini, M.N., 2015. Identification of the oscillation modes of a large power system using ambient data. *Journal of Control, Automation and Electrical Systems*, *26*(4), pp.441-453.

SciEn
Journal of Engineering Advancements Vol. 02(02) 2021, pp 132-147 https://doi.org/10.38032/jea.2021.02.006

Heat Transfer Characteristics Analysis of a Nanofluid in a Tube with a Co-axial Twisted Tape Inserter: A Numerical Approach

Tasnimul Alam[*], *Mohammad Ilias Inam*

Department of Mechanical Engineering, Khulna University of Engineering & Technology, Khulna-9203, Bangladesh

Received: April 04, 2021, Revised: July 14, 2021, Accepted: July 18, 2021, Available Online: August 21, 2021

ABSTRACT

This study demonstrates the forced convection heat transfer of a water-based nanofluid inside a circular tube with a twisted tape inserter. During these simulations, it was assumed that the tube wall heated with constant heat flux, inlet of the tube had a lower temperature and Titanium Oxide (TiO_2) particles were used as nanoparticles for nanofluid mixture. The results depict the effect of some significant parameters, i.e., twist ratio (T.R.), number of twists, Reynolds number, and volume fractions of nanoparticles on the heat transfer characteristics inside the tube with a twisted tape inserter. It is visualized from the numerical results that the Nusselt number (Nu) and heat transfer co-efficient have higher values at the twisted region than the outlet. During this numerical simulation, the Reynolds number (Re), volume fractions of particles, and twist ratios were varied into the range from 100 to 500, 0 to 0.1, and 1 to 5, respectively. Mixture model conducted these numerical simulations with Direct Numerical Simulation (DNS) method using ANSYS Fluent 16.2 with the help of three-dimensional Navier-Stokes equation. The results depicted for both water and nanofluid, the average Nusselt number and heat transfer co-efficient enhance at lower twist ratios and a higher number of twists. Results also show that Nusselt number and heat transfer coefficient increase with Reynolds Number. The heat transfer characteristics of twisted-tape inserter portion and their differences of those characteristics with the tube outlet were investigated numerically and graphically.

Keywords: Twist Ratio, Volume Fraction, Reynolds Number, Nusselt Number, Heat Transfer Co-efficient, DNS.

1 Introduction

Heat transfer is very common in lots of environmental and industrial applications. Due to that, lots of research have been conducted to enhance the convection heat transfer characteristics. Laminar flow heat transfer inside a circular tube is popular like in refrigeration and heat exchanger, just a name of a few. One of the most common heat enhancement procedures is to use twisted-tape in plain tubes. Bergles and Somerscales illustrated the enhancement of heat transfer by several active or passive methods. The author observed heat transfer enhancement by inserting a twisted-tape in laminar pipe flow [1]. Nanofluids' peristaltic motion through a porous medium that follows the non-Newtonian method inside the asymmetric channel was investigated by Eldabe and Abo Seida et al. [2]. Nanoparticles' effect on the heat transfer characteristics inside a circular tube is shown by Sundar et al. for different Reynolds numbers (*Re*) ranging 3000 ~ 22,000 and volume fractions of particles varying 0.1% ~ 0.3. The author found that Nusselt Number increased with *Re* and volume fraction; however, pumping power also increased by 18% with the volume fraction of particles [3]. Wie He and Davood Toghraie investigated the effect of a twisted tape inserter inside a tube considering the single-phase model and multiphase model. They found that multiphase models give closer results to actual results rather than using a single-phase model. They also found that twisted tape provides better performance. For instance, single tape provides 2.18 times, whereas twin twisted tape gives 2.04 times [4]. M. Arulprakasa et al. analyzed the effect of conical strips on the heat transfer characteristics using various twist ratios and geometrical configuration. The strips of the conical shape generate swirl flow which gives a higher Nusselt number as a result of higher fluid mixing. This enhancement technique protects the matter of cost and plays an important factor in energy consumption. This passive technique decreases the thermal boundary layer, which intensifies fluid mixing [5]. S. Eiamsa-ard et al. illustrated the newly constructed DWTs regarding heat transfer enhancement devices. It was assumed that wing structural part situated near the wall enhanced the decisive point of heat transfer rate. Turbulence conducted in different experiments for three different types of twist ratios 3, 4 and 5. Here, the Reynolds numbers were varied 3,000 to 27,000. Oblique delta-winglet and straight delta-winglet arrangement were set up to investigate the heat transfer characteristics to a certain extent [6]. Yeping Ping et al. depicted an external magnetic field's influence in the convective nanofluid flow having an impact of heat dissipation and thermal radiation. A rotating tube with a low, stable angular velocity induced the forced flow incident while the outer circumference tube remained firm. Aspect ratio, Reynolds numbers, Hartmann numbers, and radiative parameters was measured in that numerical study [7]. Shyy Woei Chang, Ker-Wei Yu, Ming Hsin Lu examined the effect of heat transfer due to single, double, and triple twisted tape inside a hollow circular enclosure by numerical method. They illustrated all the calculations ranging Reynolds numbers from 3,000 to 14,000, and the Nusselt numbers 1.5-2.3, 1.98-2.8, 2.86-3.76 for single, double, and triple twisted tubes, respectively. They strategically aimed to focus on extending the Reynolds number in different circumstances. The clearance between the edges of the tube's tape, wall, and cyclic swirls' characteristics was maintained stable in twin, triple twisted-tapes inserting the tube [8]. S. Eiamsa-ard, K. Wongcharee, K. Kunnarak, Manoj Kumar analyzed the behavior of a tube consisting dimples all over the surface and having a twisted tape inserting in it. The angles used

*Corresponding Author Email Address: rishan11bd@gmail.com Published by: SciEn Publishing Group

for dimples were 0, 15, 30, and 45 degrees; the twist ratios for calculation were 3.0, 4.0, 5.0 and volume fractions used for TiO_2 nanofluids were 0.05, 0.1, and 0.15%. This study covers Reynolds numbers ranging from 5,000 to 15,000. However, these dimple surface studies boosted up the blending of fluid, creating secondary flow and enhanced thermodynamic properties through the tube [9]. M. Jafaryar et al. investigated the characteristics of heat transfer using CuO-H_2O nanofluid consisting of a twisted-tape insert in a heat exchanger. This mixture's behavior was considered a single phase. The phenomena of better mixing of nanofluids were investigated by decreasing the pitch ratio. Mainly they work on the influence of swirling flow in nanofluid hydrodynamic nature [10]. The effect of a twisted perforated tape inserts having V cut configuration in a heat exchanger was investigated by Bipin Kumar, Manoj Kumar, Anil Kumar, and Siddhart Jain. They showed that heat transfer augmentation occurred varying the twist ratio 2 to 6, Reynolds number ranging from 2,700 to 23,400. This performance was measured at 1.58, where the V-cut and PTT pitch ratio changing from 1 to 2. In this case, the enhancement of heat transfer was measured by the minimum friction fall. As the PTT has the characteristics to enhance the heat transfer with less pressure drop compared to solid twisted tape (STT), hence it is proved convenient where V-cut twisted tape being used on the periphery of the structure [11]. J.P. Meyer, S.M. Abolarin investigated the heat transfer augmentation and the pressure drop characteristics in transition flow regime in a circular tube having a square-edged inlet and twisted tape inserts. The experiment was done using various twist ratios of 3, 4, and 5 where the square-edged configuration was used as the inlet. The tube has a constant heat flux confined in it. Reynolds numbers were ranged from 400 to 14,000, and the Prandtl number used in that changing between 2.9 and 6.7. When the twist ratio was kept constant, the heat flux varied. As the flux got higher, it delayed the transition from laminar to turbulent flow. If both the twist and Reynolds number had remained constant, an increment of heat flux would cause a decrease in friction factor values [12]. L. Syam Sundar et al. experimented the laminar convective heat transfer through a circular tube having a constant heat flux where Al_2O_3, TiO_2, and CuO nanofluids were used for investigating the thermodynamic properties of the flow, i.e., thermal conductivity, density and viscosity. This work had been investigated in a constant heat flux boundary condition. Moreover, each value had been compared with rational values, and the improvement in heat transfer was depicted [13]. The water flows having mixed with magnetite nanoparticles acquired two parallel disks that increase the thermal conductivity. This study is depicted by Rizwan Ul Ha1 et al. Magnetite (Fe_3O_4), Cobalt ferrite ($CoFe_2O_4$), and Mn-Zn ferrite ($MnZnFe_2O_4$) are mixed with water where water acted as the base fluid. All those results were investigated for velocity, temperature, reduced screen friction, and reduced Nusselt numbers. The variation in parameters enhances the thermal conductivity. In this investigation, water-based Magnetite (Fe_3O_4) gave the maximum lowest friction factor and low Nusselt number compared with the other mixtures. The temperature distribution was depicted broadly plotting against various nanofluid volume fractions to discuss this squeezing channel's full domain [14]. Ali Celen et al. explored a numerical method where the single-phase flow of base fluid water was compared and simulated with TiO_2 nanoparticles immersed in a base fluid with constant heat flux having temperature-dependent parameters. Local and average heat transfer characteristics such as pressure drop, temperature, and velocity distribution in several types of tested pipes were thoroughly investigated in this procedure. This study's results between measured values, numerical outputs and their changes had been represented in terms of Reynolds number and flow rate [15]. The thermodynamic performance using nanofluid flow in a triangular tube consisting a twisted tape was discussed by Cong Qi, Maoni Liu, Tao Luo, Yuhang Pan, and Zhonghao Rao. The effect of nanoparticles in a tube having twisted tape was defined by mass fractions, in which cases 0.1 wt%, 0.3 wt%, and 0.5 wt % had been utilized, and the Reynolds number raged (*Re*) 400-9000. They found a significant increment in Nusselt number by 52.5% and 34.7% for laminar and turbulent flow, respectively. The performances of heat transfer characteristics in both triangular and corrugated tubes were compared. However, it was revealed that the triangular tube with twisted tape has higher heat transfer performance than the corrugated tube [16]. Fatih Selimefendigi et al. analyzed the effect of conjugate natural convection where there was a cavity with a conductive partition. The nanofluids create the conductivity both of the opposite sides of the partitions. Al_2O_3, CuO nanoparticles were used on different sides of the partitions; a numerical analysis was performed by taking Grashof numbers 10^3-10^6, the angles of stooping between 0 to 275 degrees, thermodynamic conductivity ranged from 0.01 to 10, and finally, the volume fractions were used between 0 to 0.04. The investigation showed that thermodynamic conductivity increased due to the partitions. Simultaneously, the heat transfer rate increased its value for fulfilling the cavity with nanofluid particles [17]. Heat transfer characteristics of transient nanofluid flow between parallelly placed plates using magnetic field described in Buongiorno model were investigated by M. Sheikholeslami et al. The validation of this work was done by comparing with the results of viscous fluid. Hartmann number, Schmidt number, Brownian motion parameters, and Eckert number were used for calculating different analytical procedures in that regard. It was also revealed that the Nusselt number is enhanced by the enhancement of Hartmann number, Eckert number, and Schmidt number, but due to the increase of squeeze number, it decreases [18]. L. Syam Sundar et al. analyzed the impact of twisted tape in concern of heat transfer and friction factor improvement with Fe_3O_4 nanofluids, which reveal the magnetic characteristics. In the particular case the twist ratio *(y/d)* was taken ranging from 0 to 15, the Reynolds number varied from 3,000 to 22,000. Here, the friction factor faced increment due to 0.6% volume fraction of the nano particles' mixture. The analyzed results were compared with the generalized experimented results and found out that friction factor increment 1.231 times with Fe_3O_4 particles with base fluid [19]. The conduction and convection heat transfer nature of the Au-H_2O nanofluid mixture having differential with walls in a cubic confined system or enclosure had been depicted by Primoz˘Ternik et al. The confined walls were presumed to be adiabatic. The standard finite volume method and Boussinesq approximation were utilized to solve the differential governing equations for each case. Volume fractions were taken 0 to 5% in this regard, and Rayleigh's ranged from 10^1 to 10^6. The Nusselt number faced decrement while the volume fractions were greater than 0% [20]. The capability of heat transfer through a medium where pressure drop occurs and plays a significant role with multiple twisted tape inserts in a circular enclosure was investigated by Chaitanya Vashistha et al. The technique reduced the cost and enhanced heat transfer characteristics. Having used single, twin, four twisted tape with twist ratios 2.5, 3, and 3.5 for swirl and counter swirl flow, using the Reynolds number ranging from 4,000 to 14,000, they found out that the maximum heat transfer is possible due to the value of twist ratio 2.5 with the rise of friction losses. The maximum rise had been found for heat transfer and friction factor 2.42 and 6.96 correspondingly with

the comparison of smooth tube performance, and it was discussed by the characteristics of flow patterns [21]. Zeinali et al. investigated the heat transfer of Al_2O_3-water nanofluid flow through a duct that assimilates at the-cross-section. There was seen a high-pressure fall, high-pressure trial structure where the fluid flow characteristics have been measured. Still, the square section provides a minimum pressure drop and a better heat augmentation performance illustrated in this particular technique. However, the heat exchange rate was not well enough if a circular duct used in such case for enhancement, nanofluid fluid flow through a changed geometrical structure could be optimum to heat transfer enhancement. Using the different configurations, the enhancement of the heat transfer coefficient was 27.6% utilizing 2.5% volume fractions of nanoparticles [22]. The mixed fluid flow that is fully developed through an inclined and horizontal tube having a heat flux with uniform rate heat transfer performance was measured by M. Akbari et al. The fluid flow characteristics with an extended range of Reynolds number and Grashof had been used to solve the three-dimensional governing equations in that case. The impact of nanoparticles and the quantity of inclination in heat transfer performance has been illustrated and represented in this technique. The study showed that maximum heat transfer could be gained by 15% using 4% volume fractions of Al_2O_3 and the slope was 45 degrees for inclination [23]. M.M Rashidi, Mohammad Nasiri, Marzieh Khezerloo, and Najib Laraqi investigated the impact of a magnetic field in heat transfer characteristics of nanofluid flow where mixed convection was present. The vertical channel having sinusoidal walls where the numerical study has proceeded. In that case, the Nusselt number varied from 500 to 1000, three Hartman numbers 0, 5, and 10, sine waves having amplitude 0.1, 0.2, and 0.3 were taken to conduct the numerical study. Al_2O_3 nanofluid mixture was considered two dimensional and laminar, steady and incompressible flow. The thermal properties were assumed constant, and Boussinesq assumptions had been calculated by the density variation. It was revealed that with the increase of Grashof number, the Nusselt number enhances with various volume fractions of nanoparticles. Moreover, the Hartman number increases both the Nusselt and Poiseulle parameters that were also proved by Weres numerical investigation [24]. Ramtin Barzegian, Mostafa Keshavarz, and Alireza Alouyan experimented with the heat transfer characteristics and dropped pressure using TiO_2 nanofluid flow through a brazed plate heat exchanger (BPHE). The particles' size volume fractions 0.3%, 0.8%, and 1.5% were taken, where the investigation was fully done under turbulent flow conditions. The investigation showed that the heat transfer coefficient increases due to varied volume fraction particles with 99% pure distilled water. The maximum enhancement of the parameter i.e. heat transfer co-efficient for 0.3%,0.8% and 1.5% volume fractions were examined 6.6%, 13.5% and 23.7% respectively. Further, it was revealed that there is a negligible increment of pressure drop compared to the enhanced heat transfer coefficient [25]. Thermoplastic properties for superheated steam were investigated by Fengrui et al., where a mathematical model is assumed to predict pressure and temperature in SHS injection wells. After the validation of the model, superheated degree at the bottom-most section increased; this parameter also increased by injection rate and injection temperature. The numerical study of intrinsic flow characteristics of SHS in the wellbore could be beneficial in the oil field [26]. The neural network numerical study with TiO_2 nanofluids having spirally coiled tube and magnetic field had been studied by P. Naphon, S. Wiriyasart, and T. Arisariyawong. Different training algorithms were utilized to solve errors for attaining the required ANN configuration. Among those algorithms, Levenberg-Marquardt back propagation gives the optimal result. It was explored that for the required ANN model, the data falls within 2.5 to 5% variation of the heat transfer characteristics parameters, i.e., Nusselt numbers, friction factors. The optimal ANN had been applied to investigate the spirally coiled tube with the magnetic field's help [27]. Omid Ali Akbari et al. investigated the impact of velocity in the non-Newtonian fluid using base fluid nanoparticles. Carbon Methyl Cellulose (CMC) solution has a 5% weight concentration with water used as a base fluid using base fluid nanoparticles. A two-dimensional microchannel with Reynolds numbers ranging from 10 to 1000 and a cartesian model system was introduced. The non-Newtonian fluid motion creates effect on pressure drop, Nusselt number, temperature, and non-Newtonian fluid's motions, which were discussed elaborately in the numerical study. The analysis depicted that the increment in volume fractions and the decline in the particles' size enhanced the heat transfer performance [28]. The assumptions of heat transfer augmentation and pressure drop were investigated by Halit Bas and Veysel Ozceyhan by the method of Taguchi. The construction parameters i.e. twist ratio (y/d = 2, 2.5, 3 and 3.5), Reynolds number (Re=5,200, 9,600, 14,000 and 18,400) were taken to analyze the effect of Nusselt numbers and pressure drop on such parameters. The motive of that numerical study was to define the reason for acquiring the highest Nusselt number and lowest pressure drop by performing the least number of experiments and reducing the cost. This method showed the pressure drop decreases with the increased twist ratio, Reynolds number, and clearance ratio [29]. A numerical approach in the nanofluid simulation was studied by Adriana Minea et al., which illustrated that nanofluid affected solar energy technology. In this approach, different procedures were introduced to investigate CFD analysis. The exact procedure was a considerable reference for analyzers who are likely to deal with the study regarding nanofluid flow [30]. The convective heat transfer characteristics of nanofluid flow for the cooling operation of electro-mechanical devices by the use of single-phase fluid flow was analyzed by Mangal Singh Lodhi et al. In this case, Al_2O_3 nanofluid laminar flow, Reynolds number ranging from 300 to 1000, particles' concentration 1.0 to 3.0 and the micro-channel having 500 μm inner diameter, length of 100 mm were assumed. The performance characteristics were compared with distilled water. They measured that the heat transfer co-efficient increment was up to 24.5% while the friction factor was achieved 22.7% higher than the regular value. The performance evaluation showed that the categorization of using this nanofluid flow having higher efficiency than unity ($\eta>1$) [31].

The present paper studied the heat transfer characteristics, i.e., Nusselt number, heat transfer coefficient, the pressure drop in terms of different parameters i.e. Reynolds number, Twist ratio, number of twists, and volume fractions. However, a special case had not been discussed in the past studies of this field which is about the changes of the twisted inserter's heat transfer characteristics. Previously, all the reviews were about the outlet heat transfer characteristics, i.e., Nusselt number, Reynolds number, and pressure drop of a plain tube, rectangular or triangular channel. But in the present study, it can be seen the change of those characteristics in the twisted tape inserter having constant heat flux overall the circular tube. For calculating both the outlet and twisted tape portion's heat transfer characteristics, isosurfaces were created in both at the outlet of the tube and the end of the twisted inserter end. Thus, planes are created in both sections. Then again by using isosurface command and selecting fluid domain simultaneously in the setup portion of Ansys 16.2, we can calculate Nusselt number and heat transfer co-efficient

easily both at the outlet of tube and end of the twisted tape inserter. Different lengths of twisted tape inserters have been considered. However, the diameter of the inserters were fixed in all cases and twist-ratios were 1, 2, 3, 4 and 5. Further explanations of parameters have been discussed in section 3. Mainly this article focuses on the change heat transfer characteristics at the end of the twisted-tape inserter portion and the comparison of inserter's end to the outlet characteristics. TiO_2 nanoparticles mixture and water have been for individual calculations. And a comparison between water and nanofluid flow heat transfer characteristics at the outlet and twisted part of the tube have been made and represented graphically.

This paper has organized boundary conditions at section 2; numerical methodology along with mesh dependency has been presented in section 3; results and discussion are analyzed at section 4 and section 5 is the conclusion.

2 Boundary Conditions

In this paper, a plain tube of length L=0.5 m, diameter D=0.025 m, (refer to Fig. 1) the twist having a length of 0.1 m, 0.15 m, 0.16 m, 0.20 m, and 0.30 m; the diameter of the twist, d=0.02 m, have been taken. The plain tube contains a constant heat flux around the whole body, equal to q=300 Wm^{-2}, and it was assumed that the inlet temperature to be 306 K. For the Reynolds number 100 to 500 taking the interval of 100, the velocities were measured 0.004019, 0.008038, 0.0120577, 0.0160769 and 0.02009617 respectively. The initial gauge pressure is considered 0 Pascal in every condition. The heat transfer characteristics, i.e., Nusselt number, heat transfer coefficient, and pressure drop for the outlet and the twisted section, will be presented in this paper for twist-ratio (T.R.) 1, 2, 3, 4 and 5 as shown in Fig. 2-Fig. 6. The effect of the number of twists (1, 2, 3, 4, and 5) on heat transfer characteristics for a fixed length of twisted tape has also been investigated. The Nusselt number, heat transfer coefficient at the outlet for a plain tube having twisted tape inserter were measured separately both for water and TiO_2+water nanofluid flow varying Reynolds number from 100 to 600. The difference in those parameters for at the outlet wall and twisted tape inserter portion has also been analyzed. The twisted-tape has an adiabatic, no-slip condition, and the entrance length was considered sufficiently large for fully developed flow.

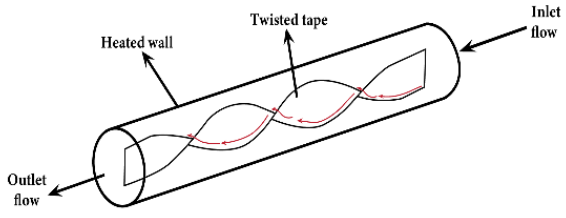

Fig. 1 Twisted-tape insert in a plain tube

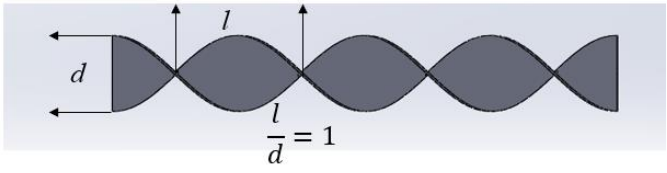

Fig. 2 Twisted-tape with twist-ratio (T.R.) 1

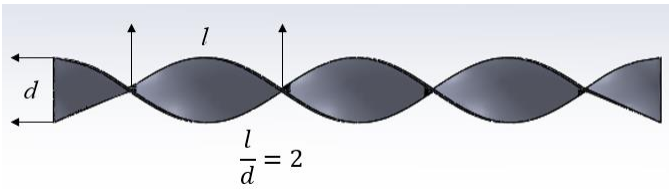

Fig. 3 Twisted-tape with twist-ratio (T.R.) 2

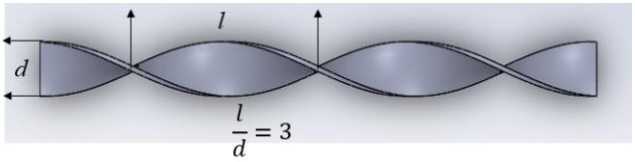

Fig. 4 Twisted-tape with twist-ratio (T.R.) 3

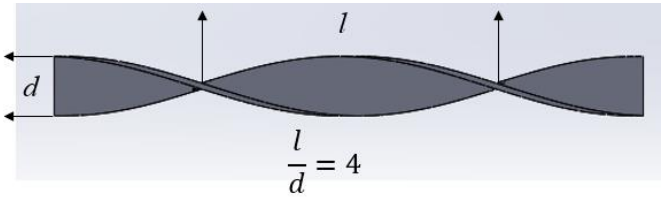

Fig. 5 Twisted-tape with twist-ratio (T.R.) 4

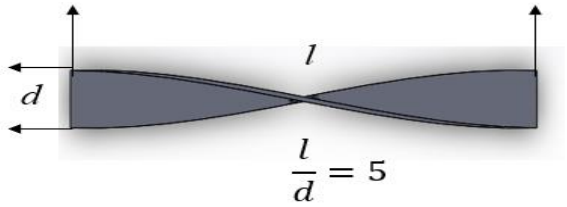

Fig. 6 Twisted-tape with twist-ratio (T.R.) 5

3 Methodology

3.1 Governing equations

The governing equations are continuity, momentum, and energy equations. Those equations are described as follows [32] -

Continuity equation:

$$\frac{\partial U_x}{\partial x}+\frac{\partial U_y}{\partial y}+\frac{\partial U_z}{\partial z}=0 \quad (1)$$

The general energy condition is additionally called the condition of movement or Navier-Stoke's condition; moreover, the condition is often used in forced convection. The condition of coherence is grown just by applying the law of preservation of mass to a little volume component inside a streaming liquid.

Momentum equation:

X-momentum equation:

$$U_x\frac{\partial U_x}{\partial x}+U_y\frac{\partial U_x}{\partial x}+U_z\frac{\partial U_x}{\partial x}=-\frac{1}{\rho}\frac{\partial p}{\partial x}+\vartheta\left(\frac{\partial Ux^2}{\partial^2 x}+\frac{\partial Ux^2}{\partial^2 y}+\frac{\partial Ux^2}{\partial^2 z}\right) \quad (2)$$

Y-momentum equation:

$$U_x\frac{\partial U_y}{\partial y}+U_y\frac{\partial U_y}{\partial y}+U_z\frac{\partial U_y}{\partial y}=-\frac{1}{\rho}\frac{\partial p}{\partial y}+\vartheta\left(\frac{\partial Uy^2}{\partial^2 x}+\frac{\partial Uy^2}{\partial^2 y}+\frac{\partial Uy^2}{\partial^2 y}\right) \quad (3)$$

Z-momentum equation:

$$U_x\frac{\partial U_z}{\partial z}+U_y\frac{\partial U_z}{\partial z}+U_z\frac{\partial U_z}{\partial z}=-\frac{1}{\rho}\frac{\partial p}{\partial z}+\vartheta\left(\frac{\partial Uz^2}{\partial^2 x}+\frac{\partial Uz^2}{\partial^2 y}+\frac{\partial Uz^2}{\partial^2 z}\right) \quad (4)$$

The entire domain is solved with a single momentum equation and the resulting velocity is shared between the phases. Those momentum equations in three dimensional volume (x, y and z) are dependent on the surface forces and body forces acting on the fluid. Surface forces act due to pressure and viscous stress whereas the body forces are determined by a generic body per unit volume integrated over the volume.

Energy equation:

$$U_x \frac{\partial T}{\partial x} + U_y \frac{\partial T}{\partial y} + U_z \frac{\partial T}{\partial z} = \frac{k}{\rho C_p}\left(\frac{\partial^2 T}{\partial x^2} + \frac{\partial^2 T}{\partial y^2} + \frac{\partial^2 T}{\partial z^2}\right) \quad 5$$

In this equation, x, y and z are spatial coordinates of a domain i.e. independent variables and density (ρ), temperature (T) are dependent of the independent variables. U_x, U_y and U_z are the velocity components of in x,y and z directions. Therefore, the equations are partial differential equations not the ordinary differential equations. In Ansys 16.2, the energy equation is kept on before running all whole calculations.

Thermoplastic properties of nanofluids can be measured by the following equations [33] -

Density for nanofluid:

$$\rho_{nf} = (1-\varphi)\,\rho_w + \varphi\,\rho_{np} \quad 6$$

ρ_w= density of water

ρ_{np}= density of nanoparticle

φ= volume fraction of particle

Specific-heat of nanofluid:

$$C_{p,nf} = \frac{\varphi \rho_{np} C_{p,np} + (1-\varphi)\rho_w C_{p,w}}{\rho_{nf}} \quad 7$$

$C_{p,np}$= specific-heat of nano particle

$C_{p,w}$= specific-heat of water

Thermal conductivity of nanofluid:

$$\frac{k_{nf}}{k_w} = \frac{k_{np} + 2k_w + 2\varphi(k_{np} - k_w)}{k_{np} + 2k_w - \varphi(k_{np} - k_w)} \quad 8$$

k_w= thermal conductivity of water

k_{np}= thermal conductivity of nanoparticle

The viscosity of nanofluid:

$$\mu_{nf} = (1 + 2.5\varphi)\,\mu_w \quad 9$$

μ_w= viscosity of water

Here, the density (ρ_{nf}), specific heat capacity ($C_{p,nf}$) of TiO_2 nanofluid have been calculated based on the empirical correlations proposed by M. Hatami, A. Kheirkhah, H.Ghanbari-Rad, Dengwei Jing et al. Also, thermal conductivity (K_{nf}) and viscosity (μ_{nf}) for nanofluid have been estimated based on the semi-empirical equations presented by Teknik, Primoz˘ et al [20]. There are some equations needed to calculate the parameters of heat transfer augmentation. They are [34] -

$$Nu = \frac{hD}{k} \quad 10$$

Nusselt number is a dimensionless parameter defined by the ratio of convective heat transfer to conductive heat transfer.

$$Re = \frac{\rho V D}{\mu} \quad 11$$

Reynolds numbers help to predict the flow pattern. In this paper laminar flow of fluid is considered. So, the Reynolds number for plain tube flow is assumed lower.

$$Q = hA(Tw - Tf) \quad 12$$

This is the basic energy balance equation for convective heat transfer. Heat transfer mainly depends on the difference of the temperature of fluid outside the thermal boundary layer T_f and the temperature of fluid on the surface T_w. Augmentation happens if heat transfer co-efficient (h) and surface area (A) increases.

$$q_1 = h\Delta T \quad 13$$

As the plain tube contains constant heat flux, the heat transfer coefficient, and the temperature difference ΔT are used to measure the parameter.

$$q_2 = h_{twist}\Delta T_{LMTD} \quad 14$$

This equation is required for calculating the heat transfer co-efficient in the twisted-tape (h_{twist}) from the constant heat flux previously discussed and ΔT_{LMTD}.

$$LMTD = \frac{(HT_s - CT_e) - (HT_e - CT_s)}{\ln\left(\frac{HT_s - CT_e}{HT_e - CT_s}\right)} = \frac{\Delta T_1 - \Delta T_2}{ln\left(\frac{\Delta T_1}{\Delta T_2}\right)} \quad 15$$

$LMTD$= log mean temperature difference

HT_s= hot stream starting temperature

HT_e= hot stream ending temperature

CT_s= cold stream starting temperature

CT_e= cold stream ending temperature

In the twisted section, there two isosurfaces were taken at the starting and end of the twist. From Ansys 16.2, the $LMTD$ can be calculated by taking the individual temperatures from the isosurfaces. Thus, the other parameters, i.e., Nusselt number and heat transfer of the twisted-tape, can be investigated.

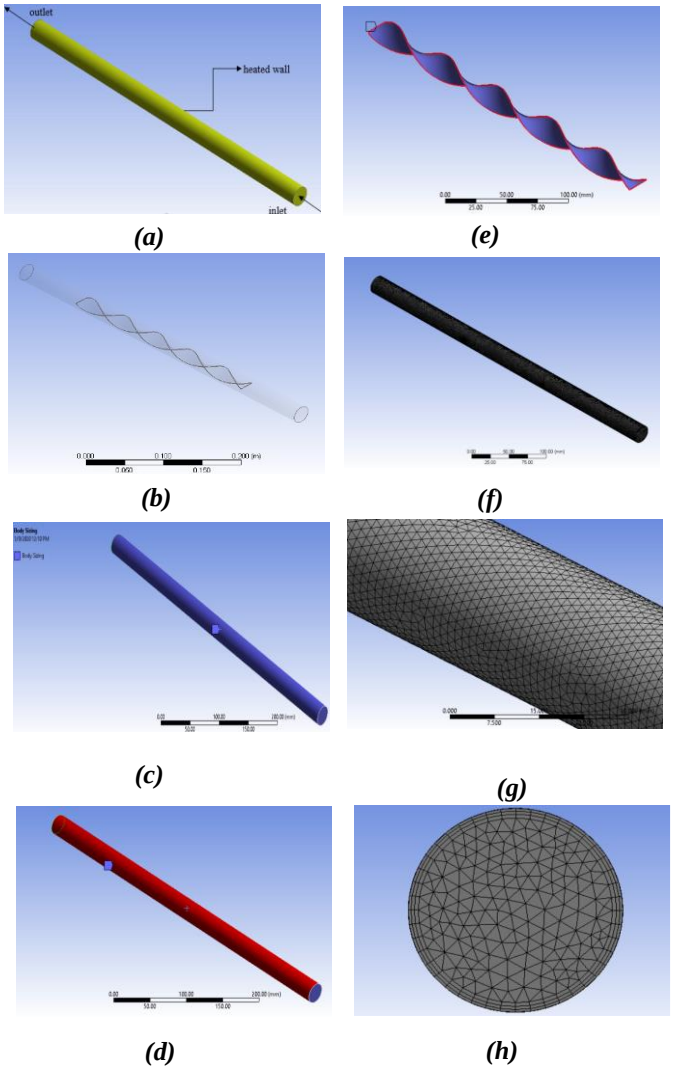

Fig. 7 Geometry and Mesh generation

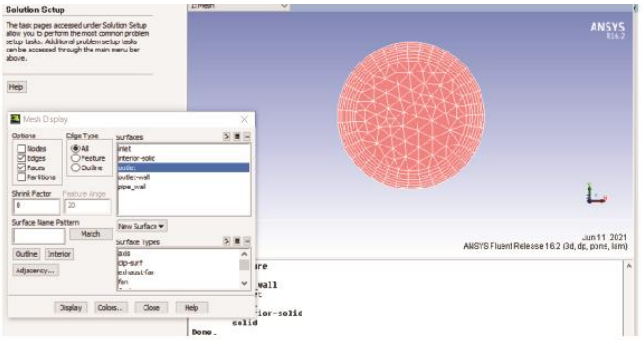

(a) Outlet

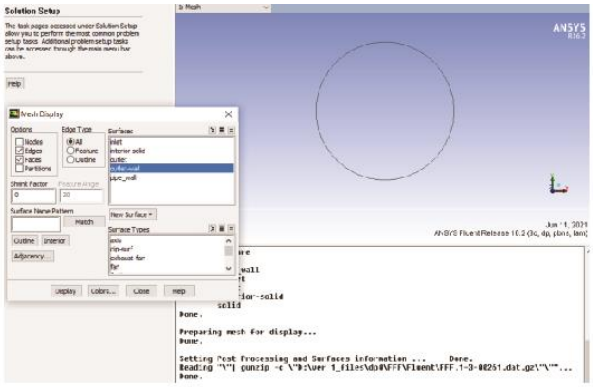

(b) Outlet Wall

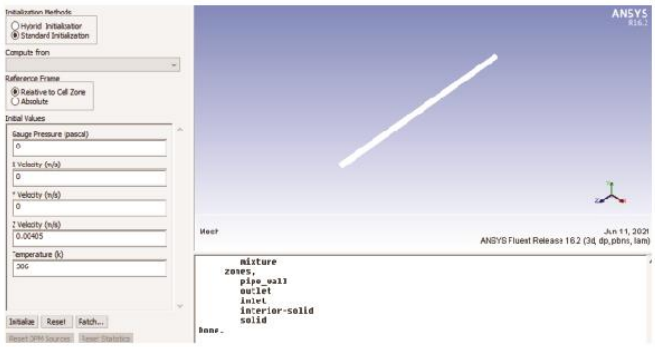

(c) Initial Temperature value

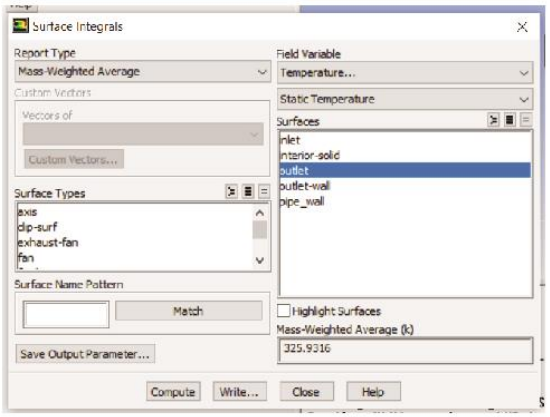

(d) Mass Weighted Temperature

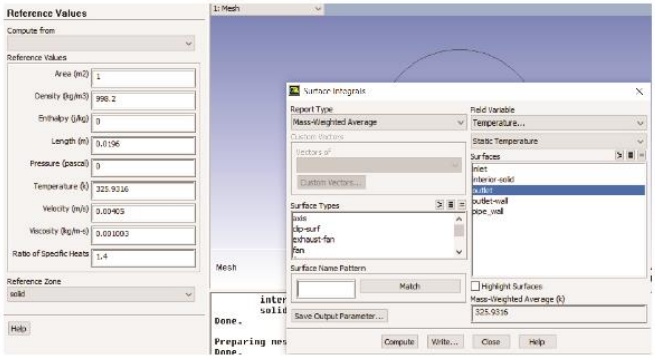

(e) Reference temperature value at outlet wall

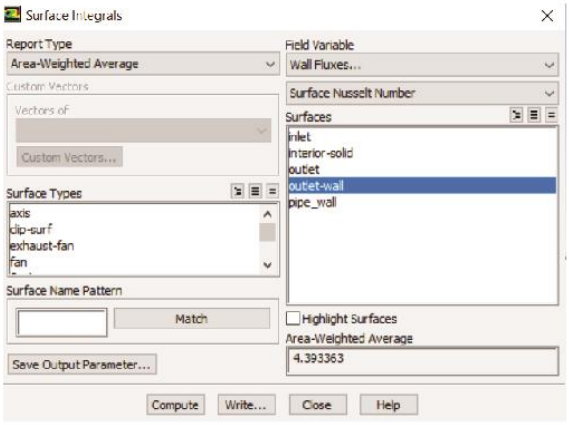

(e) Nusselt Number Calculations

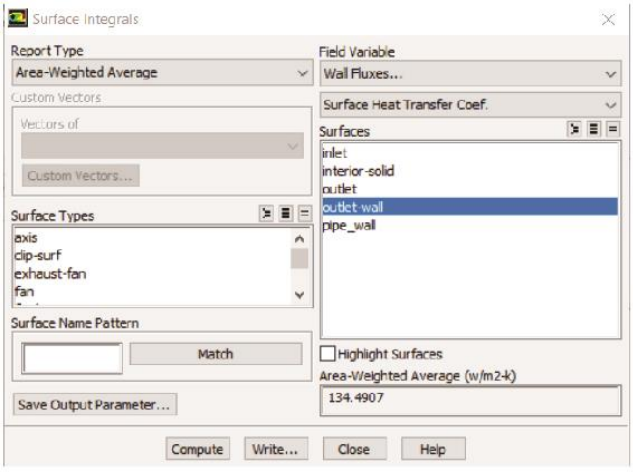

(g) Surface heat transfer co-efficient

Fig. 8 Nussselt Number and Heat Transfer Co-efficient Calculation

Another vital formula that is required for observing in which length the fully developed flow occurs is "Entrance Length Formula" for laminar flow-

$$L_{h,laminar} = 0.05ReD \quad 16$$

Table 1 Thermoplastic properties of the base fluid and nanofluid particles [35]

Property	Water	TiO_2
Density (Kgm^{-3})	998.2	3985
Specific heat ($Jkg^{-1}K$)	4182	683
Thermal Conductivity ($Wm^{-1}K^{-1}$)	0.60	11

3.2 Geometry and meshing

From Fig. 7, the different steps from geometry to mesh generation have been depicted by sub-figures (a) to (h). At first, the twisted-tape was created by SOLIDWORKS 18 software that has been imported at the geometry section of ANSYS 16.2 software, and an enclosure of cylindrical shape has been created that is shown in (a) whilst the following subsidiary figure (b) illustrated the existence of the twisted-tape inside the plain tube. Before finishing the geometry, the Boolean operation tool was utilized without preserving the tool body. Completing the first step in ANSYS, i.e., Geometry, (c) body sizing has been done by taking the element size of 1.8 mm in the second step, i.e., mesh section. An inflation layer has been imposed on the surface body, i.e., (d) of the tube. As laminar flow is considered in the whole operation, three layers of inflation operation has been taken in that option that is existed in the software. The subsectional figure (e) depicted that the inflation layer had been used at the eight different edges of the twist, taking three inflation layers as before. By clicking the option generate mesh, the final mesh product has been shown in (f) and (h) figures, revealing the mesh generation's close view. In subsidiary fig (f), the whole domain section shows a smooth transition. Another critical factor is that the growth rate has always been 1.2 in meshing operations. Several elements and element metrics statistics would be easily analyzed that the meshing operation was competent for this geometrical structure.

3.3 Procedure of Measuring Nusselt Number and Heat Transfer Co-efficient at the Outlet Wall and Twisted Tape Inserter

In this procedure, for Fig. 8, a random plain tube of 19.6 mm in length, a constant heat flux of q=300 Wm^{-2}, and inlet temperature, T_{inlet}= 306 K were taken and water was used as fluid. The calculation of Nusselt Number and Heat Transfer Co-efficient is depicted below by those images.

From subordinate figure (a) of Fig. 8, it can be easily seen by using Ansys 16.2, the outlet plane has been was created by isosurface command. Then the following picture (b), the outlet wall surface has been originated by the help of isosurface command again. Before that outlet and pipe-wall i.e. fluid domain options have been selected simultaneously. Picture (c) presents the initial value of temperature 306K. In picture (d) and (e), the mass weighted temperature at the outlet wall for water flowing through the tube and other reference values of are shown. Following picture (f), selecting surface integral from Reports and area weighted average from the type of report, the outlet wall Nusselt number can be calculated by fixing the field variable option to wall fluxes. From picture (f), the Nusselt number is observed 4.393 which is close to the actual Nusselt number 4.36 in constant heat flux condition for any length of plain tube. The surface heat transfer co-efficient can also be calculated by selecting the option surface heat transfer co-efficient shown in picture (g).

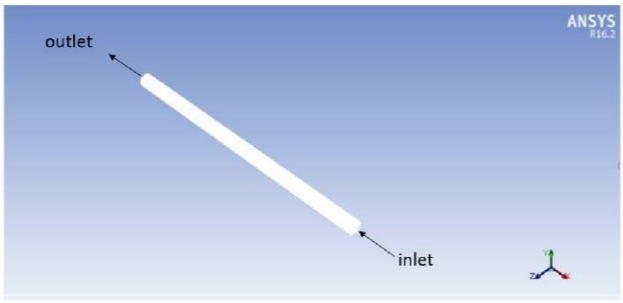

(a) Total fluid domain of tube

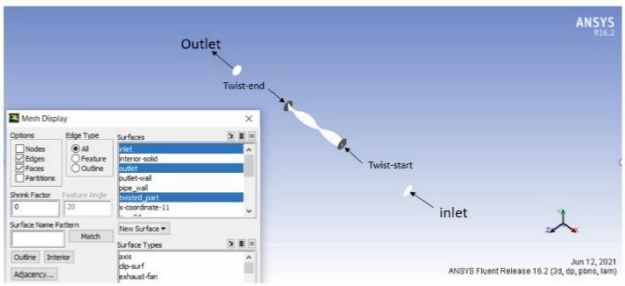

(b) Inlet-Outlet Plane and Twisted-Part

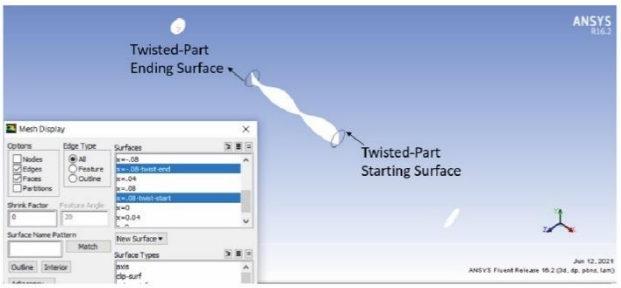

(c) Starting and Ending Surface Area of Twisted Part

Fig. 9 Twisted tape inserter starting, ending planes and surfaces

From Fig. 9, how the Nusselt number and heat transfer co-efficient in the twisted tape inserter are calculated can be easily visualized. In picture (a), the fluid domain and the direction of flow are represented. In the next picture (b), twist starting and ending planes have been created with the help of isosurface command. Twisted tape inserter's starting and ending surface have been originated same way as described previously in Fig. 8. By the temperature difference between the mass weighted averages of the twist starting and ending plane to the area weighted averages of the twist starting and ending surface, LMTD is calculated. From Equation 14 of section 3, the heat transfer co-efficient can be analyzed. Then, Equation 10 from section III, is utilized for measuring Nusselt number for various Reynolds numbers.From Fig. 9, how the Nusselt number and heat transfer co-efficient in the twisted tape inserter are calculated can be easily visualized. In picture (a), the fluid domain and the direction of flow are represented. In the next picture (b), twist starting and ending planes have been created with the help of isosurface command. Twisted tape inserter's starting and ending surface have been originated same way as described previously in Fig. 8. By the temperature difference between the mass weighted averages of the twist starting and ending plane to the area weighted averages of the twist starting and ending surface, LMTD is calculated. From Equation 14 of section 3, the heat transfer co-efficient can be analyzed.

Then, Equation 10 from section III, is utilized for measuring Nusselt number for various Reynolds numbers.

3.4 Mesh Independency Test and Model Validation

A series of simulations have been conducted for the mesh independence test. A different number of meshes were used to visualize the change in the heat transfer characteristics, i.e., Nusselt number in the plain tube with constant heat flux. A plain tube having constant heat flux possesses a Nusselt number 4.36 [36]. From Table 2, it is seen that mesh with element size 1.8 mm can produce almost similar results with meshes with element size 1.5 mm and 1 mm. Also, results just deviate 0.7% from the reference value, which is equal to 4.36. This mesh was used for further simulations.

Table 2 Mesh independency test

Element size	Nodes	Elements	Nusselt number
2.5 mm	44763	151347	4.4296
2 mm	79866	291358	4.4098
1.8 mm	103525	391318	4.3916
1.5 mm	163298	657043	4.391
1 mm	488808	2184342	4.3903

It is known that for the constant heat flux condition, the Nusselt number for a plain tube is 4.36 in case of any value of Reynolds number. From Fig. 7, it is observed that the numerical results with the element size 1.8-mm is 4.3916, which is close to the theoretical value for all the Re, taken in consideration. Another validation was done by comparing the experimental results conducted by L. Syam Sundar et al. using TiO_2 nanofluid in a plain tube with constant heat [13]. In that case, a simple tube having a length of 1.5 m, 0.005 ID, and 0.006 OD was used as geometry. As the numerical simulation ran based on constant heat flux, a constant heat flux of q=4000 wm^{-2}, inlet temperature T_{inlet}= 300k, Reynolds number *(Re)* ranging from 300 to 2100 with an interval of 300 and TiO_2 nanofluid containing 0.3% volume fraction had been used. In this present study, the same values are taken to run the simulation and compare with the results of the existed values of L of Syam Sundar's work which is shown in Fig. 11.

From Fig. 9, it is clearly observed that for Reynolds numbers ranging from 300 to 2100 for 0.3% volume fraction of TiO_2 nanofluid, the Nusselt number variation is minimal between the present work and L. Syam Sundar's numerical results. At Reynolds number=300, Nusselt number is 6.52 for the current work, which is 6.44% higher than Sundar's analysis. However, at a higher Reynolds number, this variation becomes relatively less. For example, at Reynolds number 900, the variation is 3.695%. Again, if the value of the Reynolds number being 1500 for the present state, the value of the Nusselt number is 11.04, and in Sundar's explanation [13], it was observed 10.878, which is 1.467% lower than the present state. At higher Reynolds number 2100, this variation becomes to a minimum percentage which is equal to 0.862%. That means that the present work has been entirely accurate and close the simulation values for the same boundary conditions, illustrated by L. Syam Sundar et al. [13]. Fig. 10 and Fig. 11 gave reasonably accurate results in the process of validation. The negligible deviations were eliminated for the conveniences in future procedures.

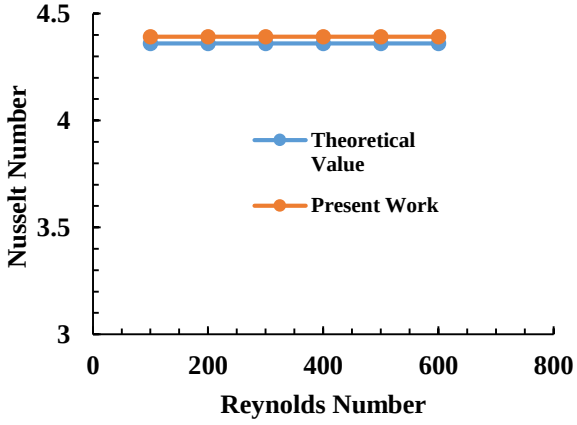

Fig. 10 Model validation for a plain tube having constant heat flux

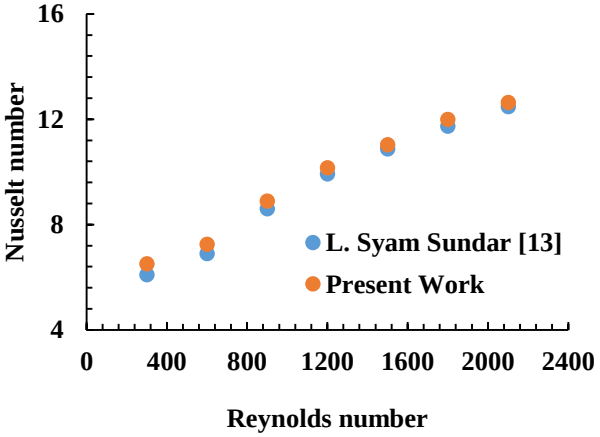

Fig. 11 Model validation for TiO2 nanofluid flow through a tube with constant heat flux

4 Results and Discussions

The total core hour for the entire calculation is (4×28×24). Fig. 12 depicts temperature contour at the different cross-sections. As mentioned above, the length of the tube is 0.5 m. For this figure, the length of the twisted tape inserter 0.3 m has been taken and the twist ratio 3. The direction of flow is seen from section 2, Fig. 1. From Fig. 12, it is seen that the starting point of flow (0.0 m position) is the inlet of tube. It has not been considered in the contours because the change in flow pattern is mainly seen from the start of the twist i.e. at 0.1 m of tube. It is observed at 0.1 m, from sub-Fig (a), the temperature is lower than the other section of the tube because the mixing of fluid is about to start. Moving forward, at 0.15-m of tube, the temperature tends to increase in Fig (b). At the middle section of the tube, i.e., Fig (c), the change can be easily visualized. Same tendency is seen in Fig (d) and at the end of the twisted tape insert i.e. at 0.4-m tube length in Fig (e). Fig (f) represents the highest possible temperature is obtained at the outlet position of the tube. Fig (g) illustrates the flow has been thermally fully developed as the temperature reaches its peak value at the tube's ending or outlet.

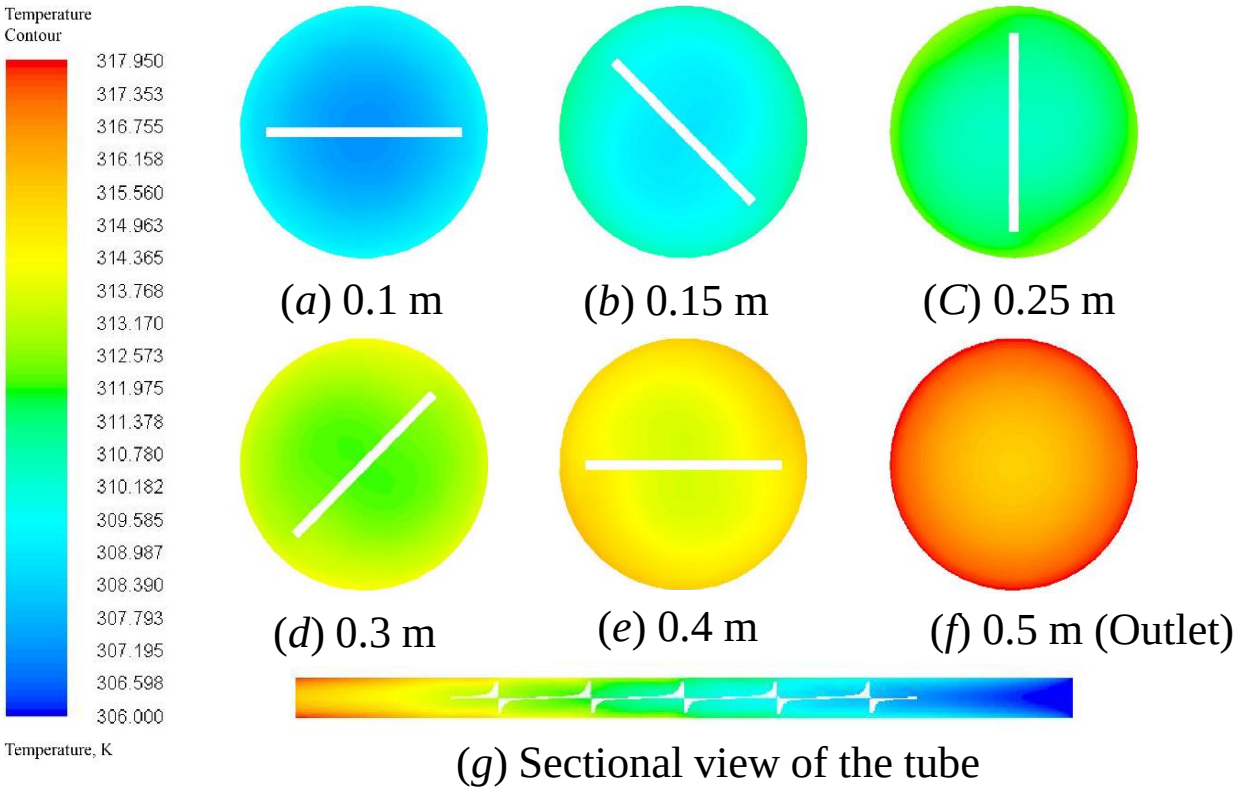

Fig. 12 Temperature contour at different sections whereas distance measure from the inlet

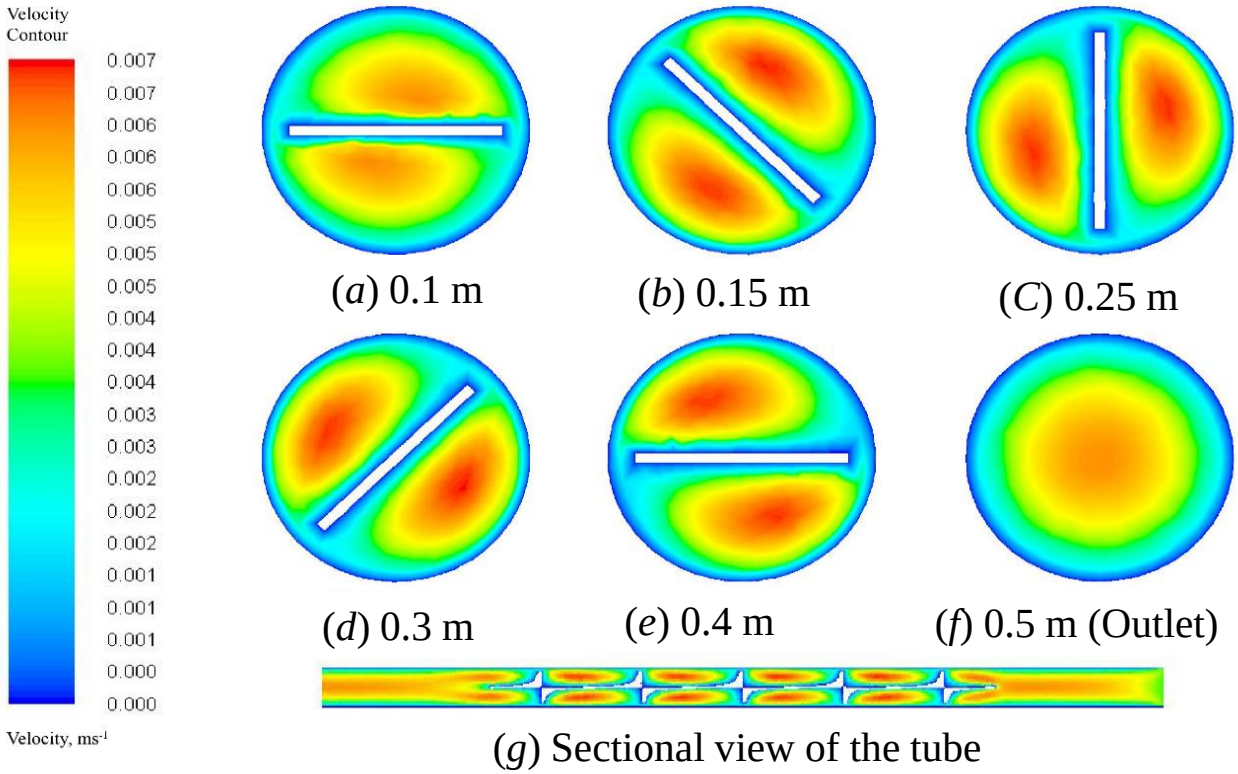

Fig. 13 Velocity contour at different cross-sections whereas distance measure from the inlet

In Fig. 13, same parameters are used just like Fig. 12. It is seen that the velocity of nanofluid flow tends to zero when the fluid is adjacent to the solid portion. Fig (a) depicts that the flow does not reach its maximum velocity at the 0.1 m distance of the tube, i.e., starting the twisted-tape. However, from Fig (b) to (e), for increasing linear distance, higher flow velocity is visualized for a specific portion, mainly at the centroid portion between the surface tube and the twisted part. Since the length of the twisted tape is 0.3-m, at the end of the twisted-tape, i.e., at 0.4 m of the tube, the highest possible velocity or peak velocity is observed because the velocity profile becomes fully developed. Fig (f) illustrates the outlet condition briefly in the pipe. As the flow became fully developed previously, there would not be any vital change in flow velocity characteristics, and subordinate Fig (g) reveals the flow is fully developed before reaching the outlet of the plain tube. The fully developed region's starting distance from inlet can be made analytically by entrance length formula which is described in Equation 16 from section 3.

The parameters related to heat transfer augmentation vary for changing specific parameters in the tube with twisted-tape insert. Twist ratio, Reynolds number, number of twists for a certain length twisted-tape, and volume fractions of fluid change the heat transfer parameters of fluid flow through a tube. Those parameters' impact on heat transfer characteristics both for water and nanofluid has been judged and illustrated. The most significant part of this paper investigates the changes of the stated features at the tube outlet and the twisted-tape part.

From Fig. 14, it is evident that the Nusselt number in the twisted-tape section is relatively higher than the value of the outlet wall section. The Nusselt number of twisted-tape section was calculated by creating isosurfaces both at the twist-start and end section, finding LMTD and heat transfer co-efficient within that section which is described elaborately in section 3 (Fig. 9). Since it is known the heat transfer rate at the twisted-tape section will be higher because of the higher fluid mixing, Nusselt number increment is visualized in the twisted tape portion than the outlet section. The highest possible Nusselt number at the outlet section and the twisted-tape will be gained for twist-ratio 1, Reynolds number (*Re*) 500 whereas the lowest is for twist-ratio 5, Reynolds number 100. The reason for this was judged previously. The maximum Nusselt number for the outlet wall section 6.975, whilst in the twisted-tape portion, it is 7.372. That shows the increment has gone 5.385%. Similarly, the lowest possible values at the outlet wall and the twisted-tape section are 4.423 and 5.1635. The percentage of enhancement in Nusselt number is 14.34. The reason for both increments can be explained by higher mixing of fluid in twisted area, extended surface area of twisted tape inserter and obstacle in boundary layer development. In the twisted tape section swirl flow happens. As the flow has gone fully developed at a certain distance, a slight change in fluid flow velocity happened by proceeding further. Most importantly, the higher mixing of fluid enhances the heat transfer rate and the heat transfer parameters.

From Fig. 15, it can be easily understood that the Nusselt number decreases at a higher twist-ratio. By varying the Reynolds number with the twist-ratio, the whole scenario is represented by the graph. For Reynolds number 100, 200, 300, 400 and 500 the decrease in Nusselt number at the outlet for twist ratio 1 to 5 is 10.4%, 16.07%, 18.67%, 20.7% and 23.832% respectively. The line for Reynolds number 500 shows linear decrement. This is due to the pitch of the twisted tape inserter decreases with the twist ratio. Thus, it is visualized that there will be more twists if the twist-ratio decreases and the mixing or turbulence of fluid would be higher for a certain length. Therefore, the Nusselt number shows an increment.

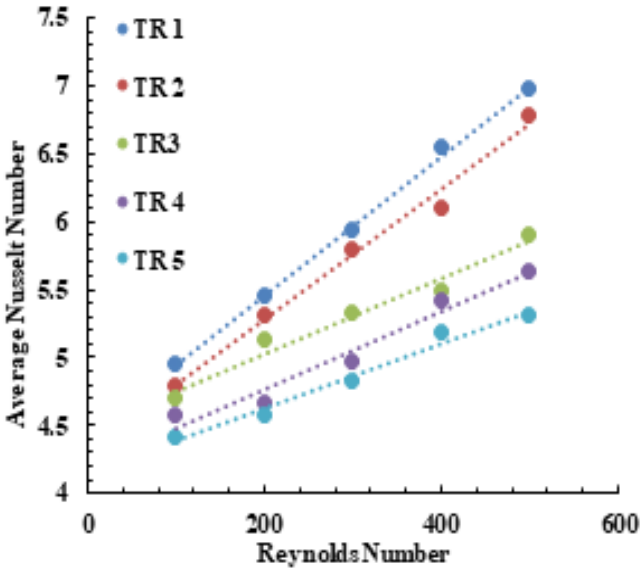

Fig. 14 Average Nusselt number vs. Reynolds number at the twisted-tape portion for water flowing through a tube for different twist ratios

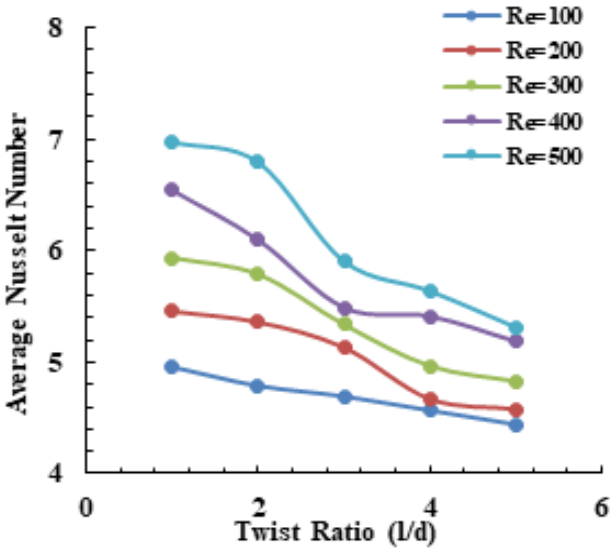

Fig. 15 Average Nusselt number vs. Twist ratio at the outlet wall for water flowing through a tube for different Reynolds numbers

It is revealed from Fig. 16, the 'highest' Nusselt number obtained for the twisted-tape portion is higher than the outlet wall section. This happens due to higher percentage mixing or turbulence and friction of fluid adjacent to the twisted tape inserter. Thus, the increased heat carrying capacity fluid of twisted portion leads to higher Nusselt number. At a certain distance of the tube, the flow becomes fully developed and this fully developed flow helps to generate the higher Nusselt number in the twisted tape inserter. And at the outlet, the fully developed flow remains steady. No turbulence is happened. That is the reason for lower Nusselt number at the outlet wall than the twisted tape portion. Like before, for Reynolds number 100, 200, 300, 400 and 500 the decrement in Nusselt number for twist ratio 1 to 5 in twisted-tape inserter is 18.5%, 17.22%, 18.77%, 19.21% and 20.265%. The decrement for twist-ratio 4 and 5 for all the Reynolds numbers is not high enough for the twisted-tape portion. This significant change is seen for twist ratios 1, 2, and 3 because of the more mixing of fluid and interruption in boundary layer development.

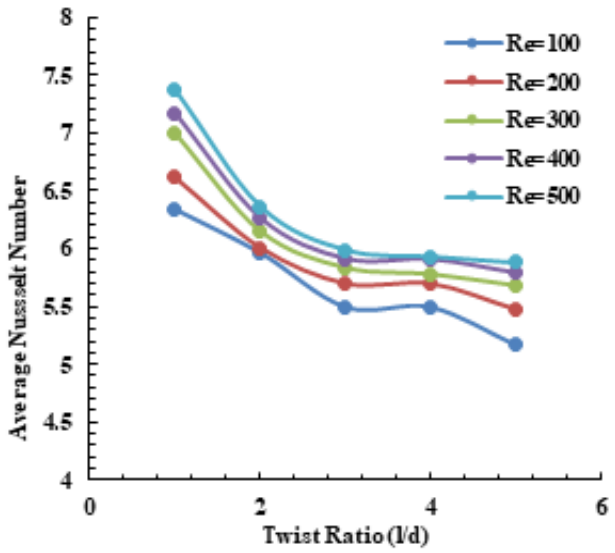

Fig. 16 Average Nusselt number vs. Twist ratio at the twisted-tape portion for water flowing through the tube for different Reynolds numbers

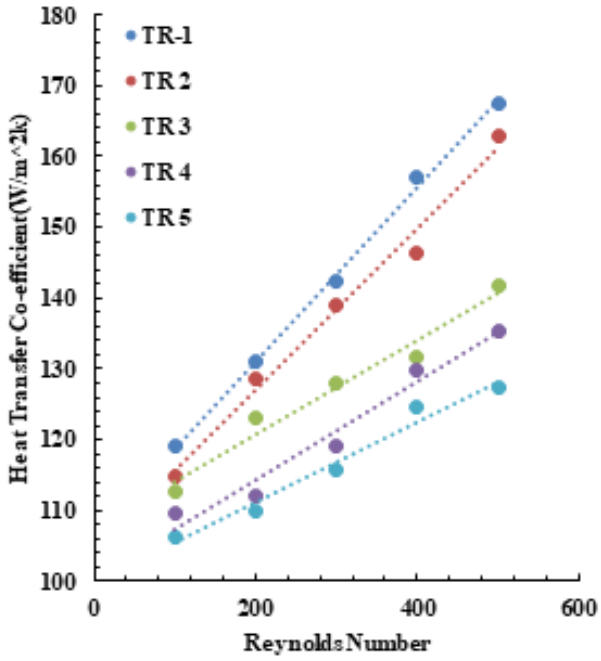

Fig. 17 Heat transfer co-efficient vs. Reynolds number at the outlet wall for different twist ratios for water flowing through the tube

From Fig. 17, it is evident that the heat transfer coefficient increases due to the increase in Reynolds number for any twist ratio. However, it shows the maximum possible value for twist ratio 1 and Reynolds number 500, 167.2. On the other hand, the lowest value is gained for twist ratio 5, and Reynolds number 100 that is 106.152. The percentage of increment is 36.58%, from the lowest to the highest value. If each twist ratio is separately considered, there will be 28.91%, 29.49%, 20.5%, 18.99%, and 16.75% increase in heat transfer co-efficient for twist ratio 1, 2, 3, 4, and 5 respectively. It is investigated that the increase is higher for twist ratios 1 and 2 than the rest. In contrast, this enhanced heat transfer rate drops quite linearly because of larger twist ratios as the fluid mixing decreased. From the trend lines, it can be easily understood the increment is linear for laminar flow for those parameters, i.e., Reynolds number and twist ratio.

As previously discussed, the heat transfer coefficient in the twisted-tape section is numerically analyzed by Ansys 16.2 software by creating isosurfaces at both ends of the twist. Then the LMTD was manually calculated within the twisted tape inserter portion. Constant heat flux is confined to the total plain tube, and the heat transfer co-efficient is analyzed just as discussed in section 3.3. From Fig. 18, it is seen that for twist ratios 4 and 5, the heat transfer increases linearly in small percentage. The percentages of increment are 11.762 and 12.155, respectively. On the other hand, for twist ratios 1, 2, and 3, the increment in rate is 14.02, 6.29, and 8.248% according to for Reynolds number 100 to 500. The maximum and minimum values are for Reynolds number 500, twist ratio 1 and Reynolds number 100, twist ratio 5. Compared with the outlet section, an increment of heat transfer coefficient at the twisted-tape portion is seen because the fluid flow gets much barrier at the twisted-tape section than the outlet wall as swirl flow created in the area for extended surface area. After passing through this section, the flow becomes fully developed, and a slight change in flow rate has been visualized.

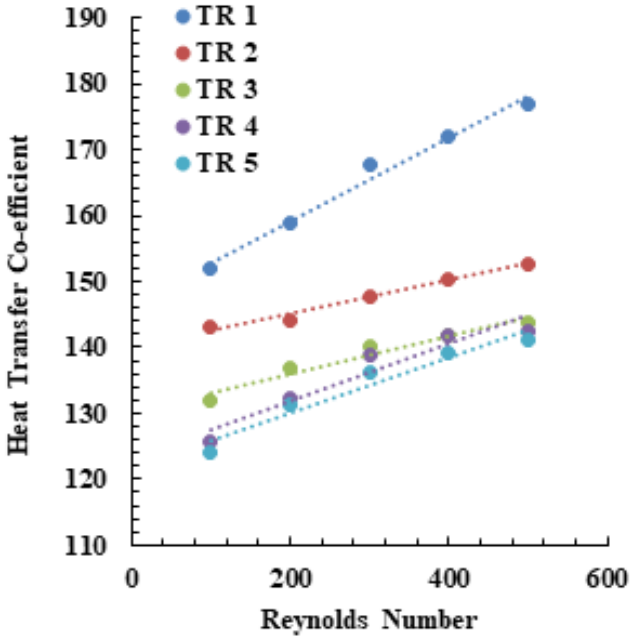

Fig. 18 Heat transfer co-efficient vs. Reynolds number at the twisted-tape section for different twist ratios for water flowing through the tube

From Fig. 19, it is evident that in this graphical representation, twist ratio has taken as an independent parameter. The presence of twisted tape inserter augments the heat transfer rate which is explained by the Equation 12 in section 3. The decrement is seen for the increased twist ratio. For twist ratio 1 to 5 the decrement is 10.79%, 16.05%, 18.67%, 20.7% and 23.8% for the described Reynolds numbers. The trend line quite similar to Fig. 15.

As discussed previously, the twisted inserter's heat transfer co-efficient was numerically investigated with the LMTD of the twisted tape's starting and ending planes (section 3.3). This passive technique of enhancing heat transfer increases the compactness of the inserter with extended surface area. These pathways of the twisted tape lead to high pressure drop. Pressure drop depends on fluid velocity; change in velocity field near twisted-tape wall will eventually increase the heat transfer co-efficient. At the extended surface area, there will be boundary layer development.

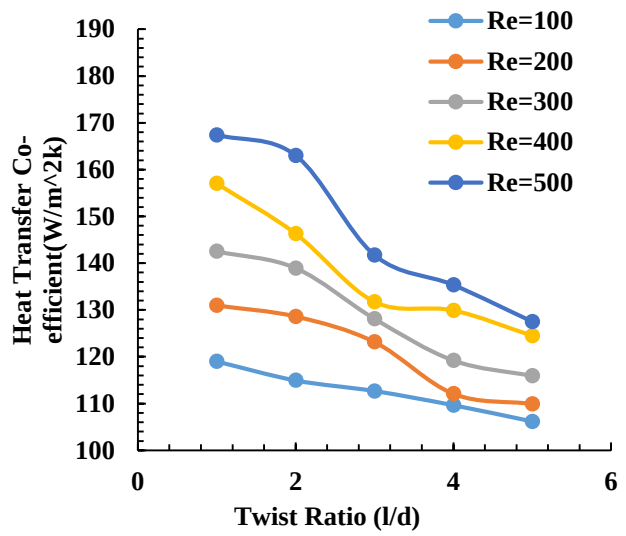

Fig. 19 Heat transfer co-efficient vs. twist ratio at the outlet wall for different twist ratios for water flowing through the tube

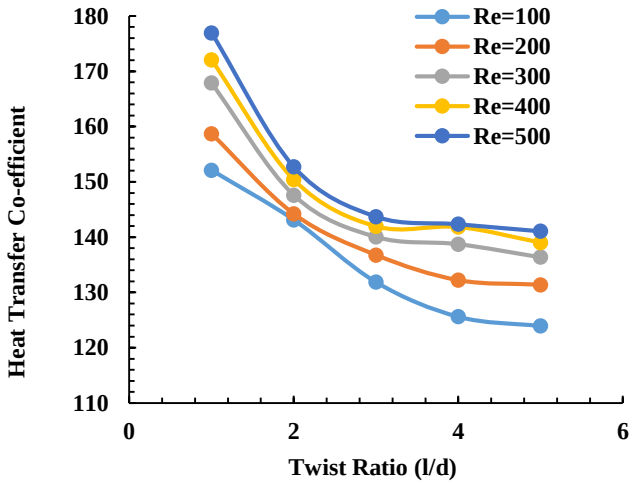

Fig. 20 Heat transfer co-efficient vs. twist ratio at the twisted-tape for different twist ratios for water flowing through the tube

As the tapes are small, boundary layer cannot develop infinitely and hence, faces obstacles continuously. Therefore, heat transfer co-efficient increases at the twisted tape portion. On the other hand, near the outlet wall of the tube, the flow becomes steady. In Fig 19, a less sharp decrease in heat transfer co-efficient is observed at that section because the flow has already become fully developed. No change in velocity field is evident. For twist ratios 4 and 5, the change in that parameter is not significant enough. It stays in a pretty stable situation for the described Reynolds numbers instead. In case of the twist ratios 1, 2, and 3, the change is significant for the Reynolds number 100 to 500. The percentages of variation between twist ratios 1 and 3 for Reynolds number 100 to 500 are 13.31, 13.836, 15.455, 17.51, and 18.77%. As the mixing of fluid becomes lower with the increase in twist ratio, heat transfer co-efficient encounters a decrement trend, illustrated by Fig. 20.

From Fig. 21, it is evident that for twist ratios 1, 2, and 3, the pressure drop per meter length of the twisted-tape portion has little difference, which can be seen from the trend line equations. For twist ratios 1 and 2, the 'pressure drop' changes pretty significantly in any Reynolds number. In both aspects, i.e., twist ratio 1 and 2, there is an increase of 22.78%, 25.53%, 29.95%, 33.82%, and 36.895% in pressure drop, respectively for Reynolds number 100 to 500. Thus, by decreasing twist-ratio, higher pressure drop can be obtained for any Reynolds number in laminar flow.

If a certain length of twisted-tape is taken for investigating the effect of the number of twists on heat transfer characteristics in a tube, for instance, by taking multiple twists, significant changes can be visualized in heat transfer phenomena at the outlet wall and the twisted-tape portion of that tube.

From Fig. 22, it is seen for the increased number of twists in a certain length the Nusselt number increases. In this particular case, the length of the twisted-tape was taken at 0.3 m. It had twists number 1,2,3,4 and 5 for a specific Reynolds number 100. Both for the outlet wall and the twisted-tape inserter Nusselt number increases quite linearly, which is observed from the figure above and the trend lines. The calculation of Nusselt number at outlet wall and twisted-tape inserter portion was discussed previously. The twisted tape portion provides higher values because the mixing, velocity and heat carrying capacity are higher in this section, which is also illustrated.

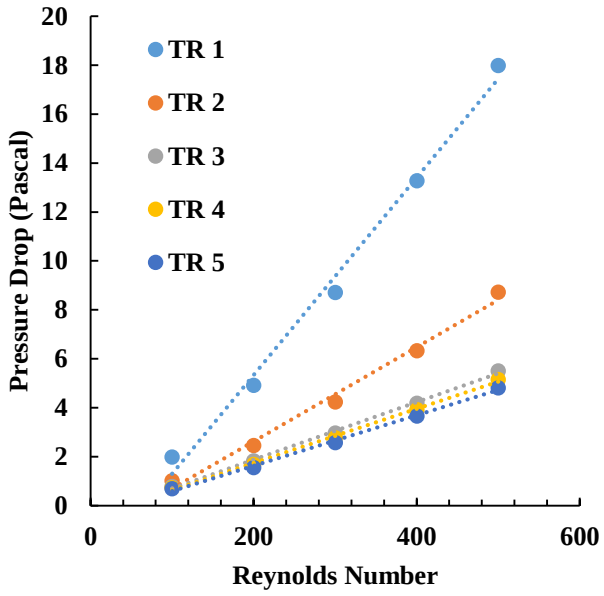

Fig. 21 Pressure drop vs. Reynolds number at the twisted-tape for different twist ratios for water flowing through the tube

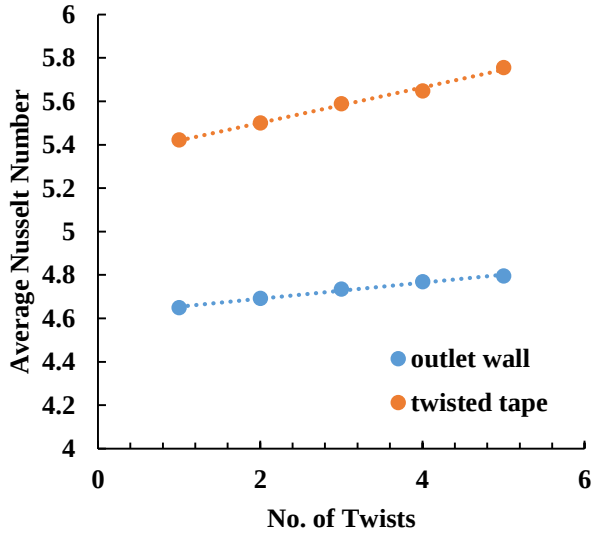

Fig. 22 Graphical representation of Average Nusselt number vs. no. of twists at the outlet wall and twisted tape for water flowing through the tube

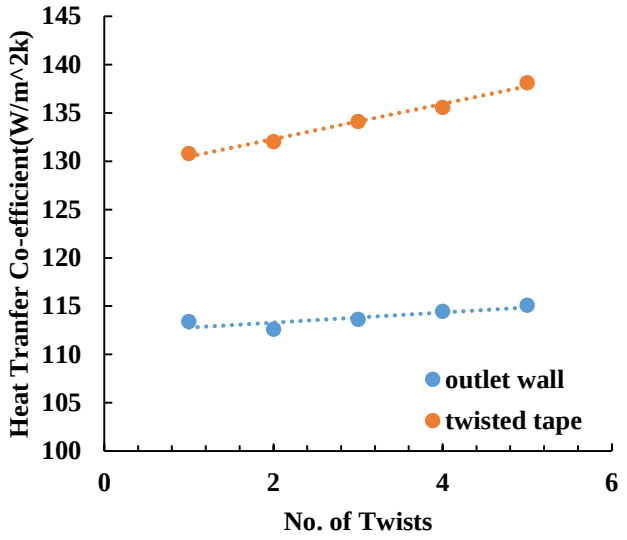

Fig. 23 Graphical representation of heat transfer co-efficient vs. no. of twists at the outlet wall and twisted tape for water flowing through the tube

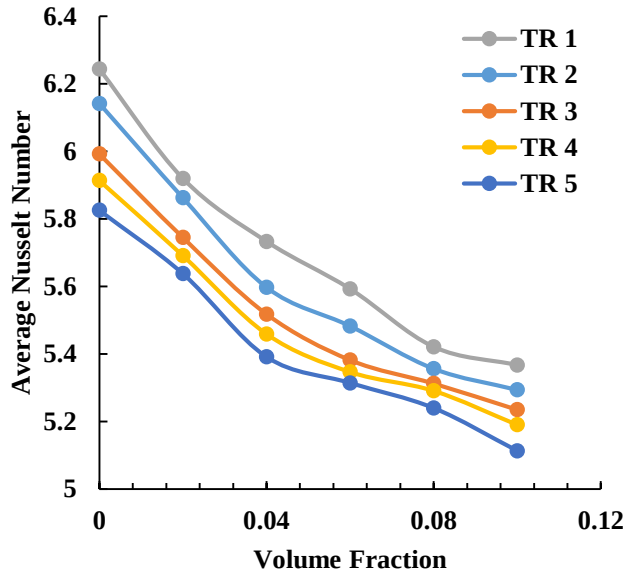

Fig. 24 Average Nusselt number vs. volume fractions at the outlet wall for different twist ratios

As stated previously, if the number of twists increases for a certain length, the heat transfer coefficient also increases. The reason behind this is for increasing the number of twists, the pitch length decreases. Thus, the twist ratio also faces a decrement. All those reasons combined are responsible for heat transfer augmentation, i.e., increasing in heat transfer co-efficient. From Fig. 23, difference in heat transfer coefficient in the twisted-tape portion and outlet wall at the tube can be described. Considering the same values discussed in Fig. 22, the heat transfer coefficient represents the linear increment in both outlet wall and twisted-tape portions. By taking twist numbers 1 to 5 for 0.3 m twisted tape inserter and Reynolds number 100, the increased percentage of heat transfer co-efficient for the twisted tape inserter portion than the outlet wall are seen 13.3 %, 14.71 %, 15.27 %, 15.57 % and 16.68 % respectively.

For nanofluid (TiO_2+water) flow through the tube, there is seen quite a few changes in terms of heat transfer characteristics as the volume fractions of nanofluid change. In this paper, five different volume fractions have been taken to judge the variation in heat transfer phenomena. From Fig. 24, it can be clearly understood that for twist ratio 1 and volume fraction 0, the highest Nusselt number is obtained, which values 6.244. The lowest value is acquired for the highest twist ratio 5, volume fraction 0.1, which is 5.1128. All the values obtained have been calculated for Reynolds number 100. Most importantly, this figure shows similarity for any twist ratio. If the volume fraction of nanofluid increases, the Nusselt number decreases. This decrement rate is approximately close in all cases. For twist ratio 1 to 5 and volume fractions 0 to 0.1 with an interval of 0.02, the decrement percentage is 14.04, 13.8, 12.63, 12.23, and 12.22 respectively for the stated conditions.

The Fig. 25 shows that the increased volume fractions of nanofluid flow in a twisted-tape causes increment in heat transfer co-efficient. As the numerical value of volume fraction increases, heat transfer co-efficient also reaches its peak. At the outlet wall, the highest value is 343.987 for volume fraction 0.1, twist ratio 1, whereas the lowest value provided by Ansys 16.2 software is 137.761 for twist ratio 5. Both values are judged under the condition of Reynolds number 100. For water, the same procedure was done in Fig. 17, where the highest and lowest value of heat transfer coefficients are 106.152 and 118.992 for Reynolds number 100. Thus, it can be said by adding particles in fluid flow, a higher heat transfer augmentation happens in the same boundary conditions. This occurs due to higher mixing of nanofluid and swirling phenomena at the twisted-tape section. The above graph illustrates that the increment in heat transfer co-efficient is linear which can be acknowledged by the trend lines.

From above figures relating to the nanofluid flow, a significant difference is visualized between water and nanofluid flow through the plain tube in the same boundary conditions. For water flows through the tube, both the Nusselt number and heat transfer co-efficient face a significant increase. However, in the case of TiO_2 nanofluid flow for the stated parameters, a decline in the values of Nusselt number is seen. On the other hand, a significantly higher heat transfer coefficient is obtained. This phenomena describes the nanofluid flow's main characteristics.

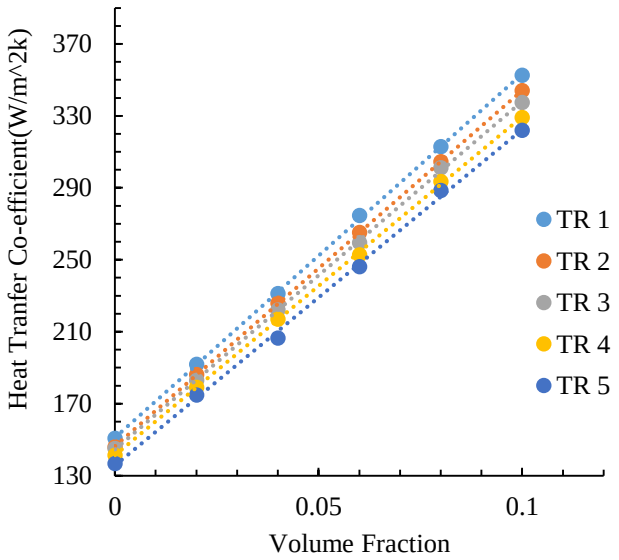

Fig. 25 Heat transfer co-efficient vs. volume fractions at the outlet wall of the twisted-tape inside the pipe containing nanofluid (TiO2+water)

In the case of pressure drop, a decline with the increase in volume fractions can be easily visualized. From Fig. 26, it is evident that the decrement is linear for all the twist ratios and volume fractions. For water, the pressure drop per meter length is relatively higher, which is illustrated elaborately in Fig. 21.

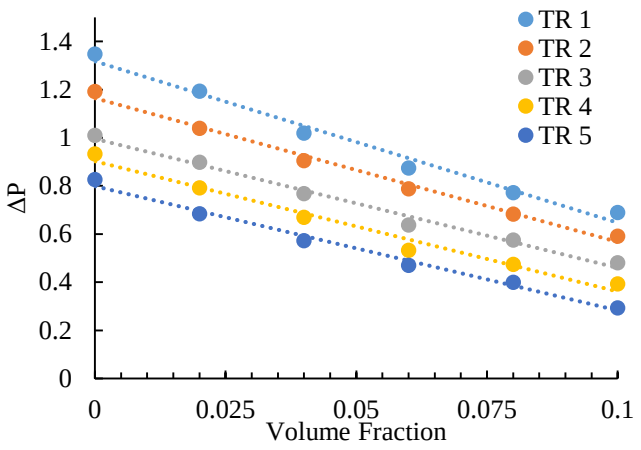

Fig. 26 Pressure drop vs. volume fractions at the twisted-tape section inside the pipe containing nanofluid (TiO2+water)

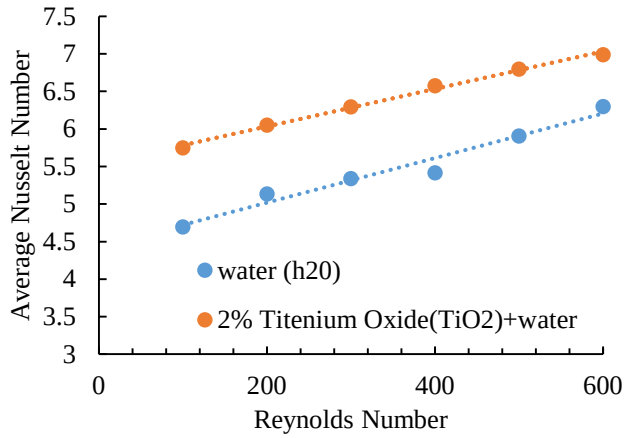

Fig. 27 The Nusselt number between water and nanofluid flowing through the tube for different Reynolds numbers at the outlet wall

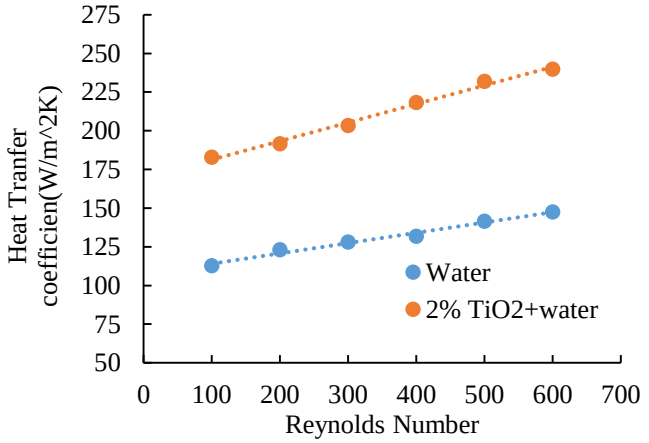

Fig. 28 The heat transfer coefficient between water and nanofluid flowing through the tube for different Reynolds numbers at the outlet wall

However, in Fig. 26, the values of pressure drop obtained in nanofluid flow are much less. For twist ratios 1 to 5 and volume fractions 0 to 0.1 with an interval of 0.02, a decrease of 48.83 %, 50.4 %, 52.475 %, 57.976 %, and 64.45 % 'pressure drop' is obtained from highest value to the lowest (considering Re=100). From the trend lines, it is evident that this decline phenomena regarding the stated parameters is linear.

Fig. 27 illustrates the variation in Nusselt number for water and TiO_2 nanofluid (2%) flow through the tube where Reynolds number 100 to 600 and a specific twist ratio 3 have been taken into consideration. It is evident that by increasing the Reynolds number, the Nusselt number increases both for water and nanofluid. By using 2% volume fraction of nano-fluid, the Nusselt number at the outlet wall increases 18.28 % for Re=100, 15.18 % for Re=200, 15.189 % for Re=300, 17.644 % for Re=400, 13.12 % for Re=500 and 9.945 % for Re=600. Thus, the difference can be easily comprehended by the stated boundary conditions and graphical representation. Not only for twist ratio 3 but also for other twist ratios and volume fractions, this difference will be observed if any analytical description is made. From Fig. 28, it can be easily understood that just like the Nusselt number, the heat transfer coefficient at the outlet wall, also shows an increment by increasing the value of Reynolds number. For water flow, the highest value is 147.529, whereas 2% TiO_2 nanofluid flow shows 239.872. A 38.49% increase at the outlet wall for Reynolds number 600 is obtained using nanofluid which is depicted in the graph. Same as Fig. 27, twist ratio 3 has been taken in this case. Reynolds number 100, 200, 300, 400 and 500 show 38.42%, 35.69%, 37.021%, 39.644% and 42.277% higher values than water flow at the outlet wall. An enhancement in heat transfer coefficient is clearly seen for all the twist ratios if nanofluid is used instead of water through the plain tube.

5 Conclusion

A comprehensive investigation of convective heat transfer through a circular pipe consisting of a twisted tape inserter is presented. The analysis shows the enhancement in heat transfer phenomena due to nanofluid flow instead of pure fluids. The parameters investigated in this procedure are volume fraction, twist ratio, number of twists, and the Reynolds number. The result clearly shows that the amount of heat transfer coefficient is increased with the increase in volume fraction of nanoparticles. However, the Nusselt number decreases with the increment in fractional volume. In another case, Nusselt number increased with a decrease in twist ratio from 5 to 1. Beyond this, it is found that maximum heat transfer is obtained at twist ratio one. The quantity of heat transfer and Nusselt number is increased with the increase in Reynolds number. Increasing the number of twists for a specific length of twisted tape depicts if the twist becomes more than one for this length, the pitch length decreases. Hence, the heat transfer coefficient, and Nusselt number increase. Differences between water flow and nanofluid flow by taking two heat transfer augmentation parameters, i.e., Nusselt number and heat transfer coefficient at the tube's outlet wall have been depicted. Not only at the outlet wall but also at the twisted-tape portion, the differences among heat transfer parameters were illustrated elaborately both for water and TiO_2 nanofluid flow. All numerical analyses, including different heat transfer parameters for nanofluid flow, were numerically calculated by taking the particles' size 10 nm. Greater sizes could also be taken, but the simulations for investigating will be time-consuming. In the tables and graphical representations, the values were compared percentage-wise in the paper. By trend lines, it was easy to comprehend the change in each aspect of specific heat enhancement characteristics.

This work could be further extended by using a double twisted-tape and investigating those stated effects at higher Reynolds numbers.

Nomenclature

l = length of the pitch
d = width of the tube
$T.R$ = Twist ratio (l/d)
T = temperature (K)
g = gravitational acceleration (ms^{-2})
Nu = Nusselt number
Re = Reynolds number
h = heat transfer co-efficient ($Wm^{-2}K^{-1}$)
υ = kinematic viscosity (m^2s^{-1})
μ = dynamic viscosity ($kgm^{-1}s^1$)
ρ = density (kgm^{-3})
ψ = stream function (m^2s^{-1})
k = thermal conductivity ($Wm^{-1}K^{-1}$)
C_p = specific heat ($Jkg^{-1}k^{-1}$)
Φ = volume fraction
q = constant heat flux (Wm^{-2})

References

[1] Somerscales, E.F. and Bergles, A.E., 1997. Enhancement of heat transfer and fouling mitigation. *Advances in heat transfer*, *30*, pp.197-253.

[2] Eldabe, N.T., Abo-Seida, O.M., Abo-Seliem, A.A., ElShekhipy, A.A. and Hegazy, N., 2017. Peristaltic transport of magnetohydrodynamic carreau nanofluid with heat and mass transfer inside asymmetric channel. *American Journal of Computational Mathematics*, *7*(01), p.1-20.

[3] Sundar, L.S., Singh, M.K. and Sousa, A.C., 2014. Enhanced heat transfer and friction factor of MWCNT–Fe3O4/water hybrid nanofluids. *International Communications in Heat and Mass Transfer*, *52*, pp.73-83.

[4] He, W., Toghraie, D., Lotfipour, A., Pourfattah, F., Karimipour, A. and Afrand, M., 2020. Effect of twisted-tape inserts and nanofluid on flow field and heat transfer characteristics in a tube. *International Communications in Heat and Mass Transfer*, *110*, p.104440.

[5] Arulprakasajothi, M., Elangovan, K., Reddy, K.H.C. and Suresh, S., 2016. Experimental investigation on heat transfer effect of conical strip inserts in a circular tube under laminar flow. *Frontiers in Energy*, *10*(2), pp.136-142.

[6] Eiamsa-ard, S., Wongcharee, K., Eiamsa-Ard, P. and Thianpong, C., 2010. Heat transfer enhancement in a tube using delta-winglet twisted tape inserts. *Applied Thermal Engineering*, *30*(4), pp.310-318.

[7] Peng, Y., Alsagri, A.S., Afrand, M. and Moradi, R., 2019. A numerical simulation for magnetohydrodynamic nanofluid flow and heat transfer in rotating horizontal annulus with thermal radiation. *RSC advances*, *9*(39), pp.22185-22197.

[8] Chang, S.W., Yu, K.W. and Lu, M.H., 2005. Heat transfers in tubes fitted with single, twin, and triple twisted tapes. *Experimental Heat Transfer*, *18*(4), pp.279-294.

[9] Eiamsa-ard, S., Wongcharee, K., Kunnarak, K., Kumar, M. and Chuwattabakul, V., 2019. Heat transfer enhancement of TiO 2-water nanofluid flow in dimpled tube with twisted tape insert. *Heat and Mass Transfer*, *55*(10), pp.2987-3001.

[10] Jafaryar, M., Sheikholeslami, M. and Li, Z., 2018. CuO-water nanofluid flow and heat transfer in a heat exchanger tube with twisted tape turbulator. *Powder technology*, *336*, pp.131-143.

[11] Kumar, B., Kumar, M., Patil, A.K. and Jain, S., 2019. Effect of V cut in perforated twisted tape insert on heat transfer and fluid flow behavior of tube flow: an experimental study. *Experimental Heat Transfer*, *32*(6), pp.524-544.

[12] Meyer, J.P. and Abolarin, S.M., 2018. Heat transfer and pressure drop in the transitional flow regime for a smooth circular tube with twisted tape inserts and a square-edged inlet. *International Journal of Heat and Mass Transfer*, *117*, pp.11-29.

[13] Syam Sundar, L., Sharma, K.V., Parveen, S. and Gaffar, M.A., 2009. Laminar convective heat transfer of nanofluids in a circular tube under constant heat flux. *International Journal of Nanoparticles*, *2*(1-6), pp.314-320.

[14] Haq, R.U., Noor, N.F.M. and Khan, Z.H., 2016. Numerical simulation of water based magnetite nanoparticles between two parallel disks. *Advanced Powder Technology*, *27*(4), pp.1568-1575.

[15] Celen, A., Kayaci, N., Çebi, A., Demir, H., Dalkılıç, A.S. and Wongwises, S., 2014. Numerical investigation for the calculation of TiO2–water nanofluids' pressure drop in plain and enhanced pipes. *International Communications in Heat and Mass Transfer*, *53*, pp.98-108.

[16] Qi, C., Liu, M., Luo, T., Pan, Y. and Rao, Z., 2018. Effects of twisted tape structures on thermo-hydraulic performances of nanofluids in a triangular tube. *International Journal of Heat and Mass Transfer*, *127*, pp.146-159.

[17] Selimefendigil, F. and Öztop, H.F., 2016. Conjugate natural convection in a cavity with a conductive partition and filled with different nanofluids on different sides of the partition. *Journal of Molecular Liquids*, *216*, pp.67-77.

[18] Sheikholeslami, M., Ganji, D.D. and Rashidi, M.M., 2016. Magnetic field effect on unsteady nanofluid flow and heat transfer using Buongiorno model. *Journal of Magnetism and Magnetic Materials*, *416*, pp.164-173.

[19] Sundar, L.S., Kumar, N.R., Naik, M.T. and Sharma, K.V., 2012. Effect of full length twisted tape inserts on heat transfer and friction factor enhancement with Fe3O4 magnetic nanofluid inside a plain tube: An experimental study. *International Journal of Heat and Mass Transfer*, *55*(11-12), pp.2761-2768.

[20] Ternik, P., 2015. Conduction and convection heat transfer characteristics of water–Au nanofluid in a cubic enclosure with differentially heated side walls. *International Journal of Heat and Mass Transfer*, *80*, pp.368-375.

[21] Vashistha, C., Patil, A.K. and Kumar, M., 2016. Experimental investigation of heat transfer and pressure drop in a circular tube with multiple inserts. *Applied Thermal Engineering*, *96*, pp.117-129.

[22] Heris, S.Z., Nassan, T.H., Noie, S.H., Sardarabadi, H. and Sardarabadi, M., 2013. Laminar convective heat transfer of Al2O3/water nanofluid through square cross-sectional duct. *International Journal of Heat and Fluid Flow*, *44*, pp.375-382.

[23] Akbari, M., Behzadmehr, A. and Shahraki, F., 2008. Fully developed mixed convection in horizontal and inclined tubes with uniform heat flux using nanofluid. *International Journal of Heat and Fluid Flow*, *29*(2), pp.545-556.

[24] Rashidi, M.M., Nasiri, M., Khezerloo, M. and Laraqi, N., 2016. Numerical investigation of magnetic field effect on mixed convection heat transfer of nanofluid in a channel with sinusoidal walls. *Journal of Magnetism and Magnetic Materials*, *401*, pp.159-168.

[25] Barzegarian, R., Moraveji, M.K. and Aloueyan, A., 2016. Experimental investigation on heat transfer characteristics and pressure drop of BPHE (brazed plate heat exchanger) using TiO2–water nanofluid. *Experimental Thermal and Fluid Science*, *74*, pp.11-18.

[26] Sun, F., Yao, Y., Chen, M., Li, X., Zhao, L., Meng, Y., Sun, Z., Zhang, T. and Feng, D., 2017. Performance analysis of superheated steam injection for heavy oil recovery and modeling of wellbore heat efficiency. *Energy*, *125*, pp.795-804.

[27] Naphon, P., Wiriyasart, S. and Arisariyawong, T., 2018. Artificial neural network analysis the pulsating Nusselt number and friction factor of TiO2/water nanofluids in the spirally coiled tube with magnetic field. *International Journal of Heat and Mass Transfer*, *118*, pp.1152-1159.

[28] Akbari, O.A., Toghraie, D., Karimipour, A., Marzban, A. and Ahmadi, G.R., 2017. The effect of velocity and dimension of solid nanoparticles on heat transfer in non-Newtonian nanofluid. *Physica E: Low-Dimensional Systems and Nanostructures*, *86*, pp.68-75.

[29] Bas, H. and Ozceyhan, V., 2014. Optimization of parameters for heat transfer and pressure drop in a tube with twisted tape inserts by using Taguchi method. *Arabian Journal for Science and Engineering*, *39*(2), pp.1177-1186.

[30] Minea, A.A., Buonomo, B., Burggraf, J., Ercole, D., Karpaiya, K.R., Di Pasqua, A., Sekrani, G., Steffens, J., Tibaut, J., Wichmann, N. and Farber, P., 2019. NanoRound: A benchmark study on the numerical approach in nanofluids' simulation. *International Communications in Heat and Mass Transfer*, *108*, p.1-23.

[31] Lodhi, M.S., Sheorey, T. and Dutta, G., 2020. Single-phase fluid flow and heat transfer characteristics of nanofluid in a circular microchannel: Development of flow and heat transfer correlations. *Proceedings of the Institution of Mechanical Engineers, Part C: Journal of Mechanical Engineering Science*, *234*(18), pp.3689-3708.

[32] White, F. M., 1998, Fluid Mechanics, McGraw-Hill Higher Education.

[33] Hatami, M., Kheirkhah, A., Ghanbari-Rad, H. and Jing, D., 2019. Numerical heat transfer enhancement using different nanofluids flow through venturi and wavy tubes. *Case Studies in Thermal Engineering*, *13*, p.1-10.

[34] Munson, B. R., Young, D. F., Okiishi, T. H. and Huebsch, W. W., 2015, Fundamentals of Fluid Mechanics, John Wiley & Sons, Inc., New Jersey.

[35] Sakinah, S.Z.A., Azmi, W.H. and Alias, J., 2020, May. Characterization of TiO2 nanopaint for automotive application. In *IOP Conference Series: Materials Science and Engineering* (Vol. 863, No. 1, p. 012053). IOP Publishing.

[36] Holman, J. P. and Bhattacharyya, S., 2016, Heat Transfer (In SI Units), Tata McGraw Hill Education Private Limited, New Delhi.

SciEn
Journal of Engineering Advancements Vol. 02(03) 2021, pp 148-152 https://doi.org/10.38032/jea.2021.03.004

Effects of Gasoline-Diesel Ratio on Combustion and Emission Characteristics of a Dual-Fuel CI Engine: A CFD Simulation

*Md. Habibur Rahaman, Kazi Mostafijur Rahman**

Department of Mechanical Engineering, Khulna University of Engineering & Technology (KUET), Khulna-9203, Bangladesh.

Received: July 11, 2021, Revised: August 16, 2021, Accepted: August 18, 2021, Available Online: August 22, 2021

ABSTRACT

Recently, considerable efforts are made by the engine researches all over the world, focusing primarily on achieving ultra-low emissions of NOx (nitrogen oxides) and soot without any compromise to high thermal efficiency from dual-fuel engine. In this study, combustion performance and engine-out emission of a single cylinder gasoline-diesel dual-fuel engine are numerically investigated by employing a commercial computation fluid dynamics (CFD) software, especially developed for internal combustion engines modeling. Here, gasoline-diesel relative ratio has been varied to find its impacts on performance of a dual-fuel engine. The results show that, in-cylinder pressure, in-cylinder temperature and rate of heat release (ROHR) are increased with gradual increment in diesel relative to gasoline. Injecting higher amount of diesel directly inside the combustion chamber as pilot fuel might have facilitated the auto-ignition process by reducing the ignition delay and accelerated the premixed gasoline-air flame propagation. These led to shorter main combustion duration which is quite desirable to suppress the knock in dual-fuel engines. In addition, NOx emission is found to decrease with relatively higher percentage of diesel. On the other hand, with increasing gasoline ratio relative to diesel, combustion duration is prolonged significantly and led to incomplete combustion, thereby increasing unburned hydrocarbon (UHC) and carbon monoxide (CO).

Keywords: Dual-fuel Engine, Gasoline-Diesel Ratio, CFD, Rate of Heat Release (ROHR), Combustion Duration.

1 Introduction

Depletion of crude oil, unstable fuel supply/cost, growing concern on environmental pollution and imposing stringent emission regulation, have intensified the demand of clean and efficient combustion technology for internal combustion engines (ICE). In transportation sector, though diesel engines are most fuel-efficient but they suffer from excessive emissions of NOx (nitrogen oxides) and soot which require the use of expensive exhaust-gas after-treatment devices. To overcome these challenges, dual-fuel engine is gaining attention where main fuel with low reactivity is added through the intake port of the engine; a pilot fuel with high reactivity is injected in relatively small amount directly inside the combustion chamber in order to initiate the combustion of premixed or partially primary fuel–air charge [1]-[3]. Kokjohn et al. [1] investigated the effects of varying fuel reactivity on performance a gasoline-diesel dual-fuel engine running with varying quantities of gasoline and diesel fuel to optimally accommodate engine load and speed changes. They achieved the dual-fuel operation by port fuel injection of gasoline and early cycle direct injection of diesel fuel. In their study it is reported that around 80% gasoline-20% diesel has optimal fuel reactivity. Many automobile manufacturers, now a days, have been focusing on dual-fuel mode of combustion in compression ignition engine using various combination of both alternative and conventional fuels such as hydrogen, alcohol-based fuel, biogas, biodiesel, methane, natural gas, diesel and gasoline [4]-[10]. Mousavi et al. [11] investigated the effects of pilot diesel fuel injection timing and quantity in a natural gas-diesel CI engine. They found that optimizing the pilot fuel injection timing and quantity of diesel could results in an improvement in engine efficiency and reduction in the CO emissions though NO productions increase. Ma et al. [12] carried out an experimental study on n-heptane/diesel dual-fuel CI engine. They reported that injection timing of pilot diesel fuel has significant influences on both combustion and emission performances. NOx emissions could be reduced for premixed ratio up to 0.3 but beyond that value of premixed ratio, NOx emissions will rise up. In a study by Micklow et al. [13], it is shown that a major portion of natural gas near the cylinder wall remained unburned in a dual-fuel engine operation at part load. Use of multi-dimensional ICE modeling through the high-performance computer (HPC) facilitates the design and development of new advanced engine with high efficiency and low emission in order to meet the market demand. Computational Fluid Dynamic (CFD) is a proven tool to model the complex processes such as high-pressure fuel injection, mixture formation, ignition and flame propagation occurring inside the combustion chamber of ICE. Mattarelli et al. [14] performed CFD modeling of a 4-cylinder diesel engine, capable of operating in both diesel combustion and dual-fuel (Diesel and Natural gas) combustion modes. The modeling data demonstrated that, in dual-fuel mode of combustion, formation of soot particles, CO and CO_2 emissions could be reduced but NOx emission remains at higher level. Lopez et al. [15] characterized the impacts of relative ratios of gasoline-diesel blends on ignition delay and flame structure in a dual-fuel engine. Increasing the gasoline ratio in the mixture lead to improved ignition delay. Similar findings have been reported by Cha et al. [16]. They found that increasing the gasoline amount decreases soot and NO emissions. Puduppakkam et al. [17] performed CFD modeling of dual-fuel engine utilizing detailed kinetics mechanisms for both the gasoline and diesel surrogate fuels with an advanced and efficient chemistry solver. Their modeling approach was able to achieve accurate representation of

*Corresponding Author Email Address: mostafij@me.kuet.ac.bd

combustion phasing and better predictions of unburned hydrocarbons and CO emissions. They found that compared to less-reactive gasoline surrogate components such as iso-octane and toluene, most-reactive fuel component n-heptane (component in both diesel and gasoline surrogates) consumed at a much faster rate.

Studies on the performances of dual-fuel engines operating with varying gasoline-diesel ratio are very limited, especially the numerical investigation. However, this is quite pertinent to explore the different combustion strategies by varying fuel reactivity in order to extend the dual-fuel engine operating regime with optimized fuel blends. Therefore, in this study, effects of gasoline-diesel relative ratio on combustion and emission characteristics of a dual-fuel engine have been investigated. Combustion characteristics in terms of in-cylinder pressure, in-cylinder temperature and rate of heat release (ROHR) are checked whereas engine-out emissions such as-oxides of nitrogen (NOx), unburned hydrocarbon (UHC) and carbon monoxide (CO) level are quantified with different blends of gasoline-diesel by employing computational fluid dynamics (CFD) modeling.

2 Computational Approach for Modeling Dual-Fuel Engine Operation

A commercially available software ANSYS Forte (version 18.1) incorporated with highly efficient advanced chemistry solver module CHEMKIN is used to simulate the dual-fuel engine operation. ANSYS Forte is based on the solution of full Reynolds-averaged Navier-Stokes (RANS) equations. For the compressible and gas phase flows, model transport equations of mass, momentum and energy conservation laws are formulated. RNG k-ε turbulence model was used as it is extensively validated for modelling the ICE.

2.1 Geometry and Mesh Generation

The heavy-duty 2.44-Liter Caterpillar 3401 Single Cylinder Oil Test Engine (SCOTE) used by Kokjohn et al. [1] was modeled in this study. Engine specifications are given in Table 1. For computational domain, sector mesh technique is adopted which is quite useful to reduce the computational cost when combustion chamber of the engine is considered to be symmetrical with respect to each nozzle-hole of the injector. The engine has a six-hole injector which allows the simulation to use a 60° sector (360°/6). Therefore, a sector mesh of 60° angle (Fig. 1) with periodic boundary conditions is utilized.

Table 1 Engine Specifications

Engine	Caterpillar SCOTE
No. of cylinders	1
Bore	13.72 cm
Stroke	16.51 cm
Connecting Rod Length	26.16 cm
Compression Ratio	16.1
Strokes Per Engine Cycle	4
Engine Speed	1500 rpm
No. of Nozzle-hole	6
No. of Diesel Injection	Double (pulsed)
Total fuel mass (gasoline + diesel) [mg/cycle]	130
Squish	0.157 cm

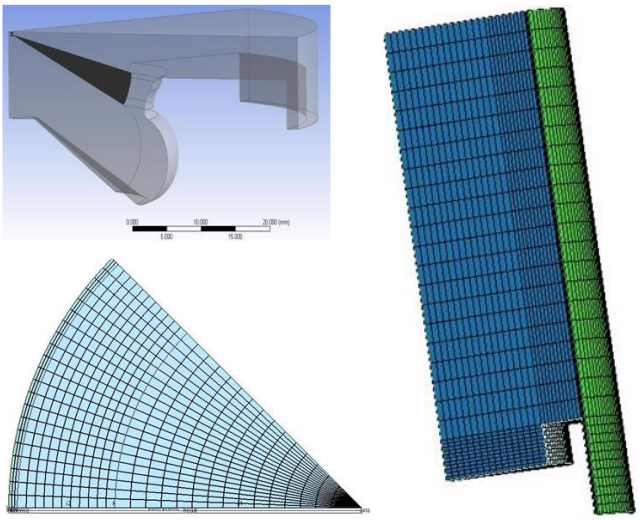

Fig. 1 A 60° sector mesh for a modeling dual-fuel engine

2.2 Ignition and Flame Propagation Models

The thermodynamic properties and chemical reaction mechanisms of gasoline-diesel fuels available in the Lawrence Livermore National Laboratory (LLNL), USA - are added in CHEMKIN format to the chemistry model of the CFD code to simulate the dual-fuel combustion process of gasoline-diesel fuels [18]. A reduced mechanism with 425 species and 3128 reactions resulted for the reactivity-controlled compression ignition (RCCI) engine (i.e., dual-fuel) simulations [17]. In dual-fuel engine, the injection and autoignition of the liquid pilot (i.e., diesel) fuel serves to initiate the flame propagation of premixed air-fuel (i.e., gasoline-air). For tracking flame propagation of premixed air-fuel, well-established G-equation model is used [19]-[20]. In ANSYS Forte, the simulation can consider both auto-ignition and flame-propagation modes of combustion progress simultaneously.

Table 2 Initial Conditions

Parameters	Value
Intake Valve Closing	95° before TDC
Exhaust Valve Open	130° after TDC
Temperature at Inlet Valve Closing	350 K
Pressure at Inlet Valve Closing	4 bar
Turbulence Intensity	0.1
Turbulent Length Scale (cm)	1.0
Initial Swirl Ratio	0.7
Initial Swirl Profile Factor	3.11

2.3 Initial and Boundary Conditions

Table 2 and Table 3 present the initial and boundary conditions of the engine simulations, respectively. For all the values of gasoline/diesel ratios, these initial and boundary conditions remain the same. Turbulent law-of-the-wall velocity condition and fixed temperature walls are usually employed for

engine simulation. Here, to capture wall boundary layer effects more accurately for boundary layers that are thinner than the mesh size, the "Law of the Wall" model is specified for piston, head and liner.

Table 3 Boundary Conditions

Periodicity	60 degrees
Wall model	Law of the wall
Piston Temperature	500 K
Head Temperature	500 K
Line Temperature	430 K

3 Results & Discussion

3.1 Effects of gasoline-diesel relative ratio on combustion characteristics

The influences of varying gasoline-diesel ratio on combustion performance in terms of in-cylinder pressure, in-cylinder temperature and rate of heat release are elucidated in Fig. 2 - Fig. 4. Increasing the relative amount pilot fuel, i.e., diesel compared to gasoline resulted in gradual increment in peak in-cylinder pressure, temperature and apparent heat release rate. With the increase of pilot diesel fuel amount, more energy is released. Consequently, apparent heat release rate (AHHR) which is the difference between chemical heat release rate and wall heat transfer loss rate, is also higher than lower diesel substitution case. From Fig. 4, it is seen that, 15% and 21% diesel cases led to higher peaks in apparent heat release rate than 8% diesel injection.

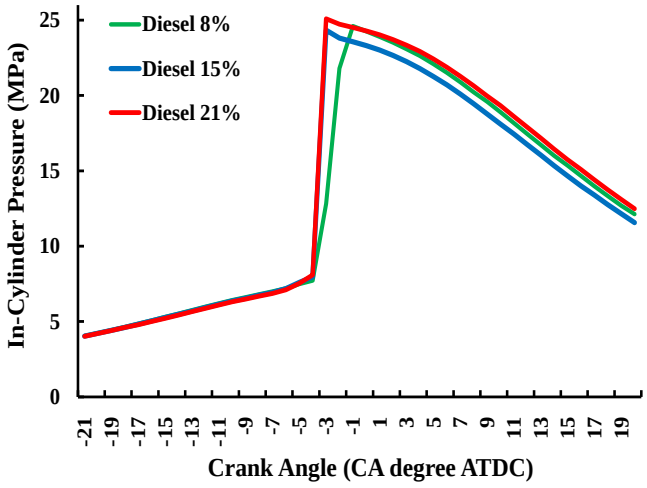

Fig. 2 In-cylinder pressure history with different gasoline-diesel relative ratio

A careful observation of Fig. 4 reveals that heat release occurred earlier for both 21% diesel and 15% diesel pilot injection cases than that for 8% diesel pilot injection. This clearly indicates that autoignition of pilot fuel as well as onset of combustion are earlier when relative amount high reactivity pilot fuel (i.e., diesel) is increased compared to low reactivity fuel (i.e., gasoline). In addition, early autoignition of pilot fuel established the fact that, ignition delay period reduced with higher percentage of pilot fuel injection.

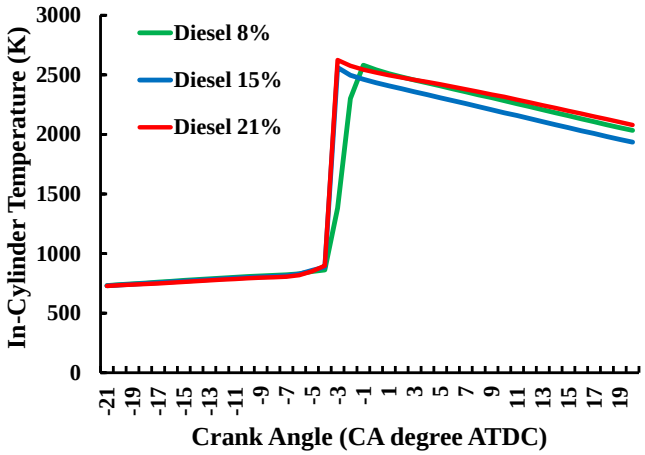

Fig. 3 In-cylinder temperature with different gasoline-diesel relative ratio

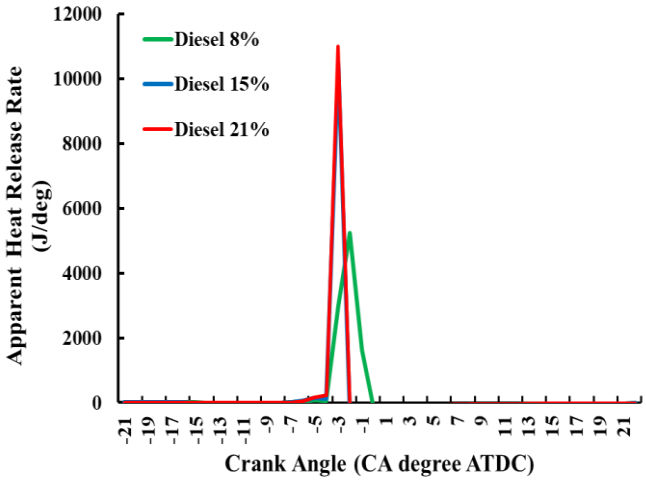

Fig. 4 Apparent Heat Release Rate with different gasoline-diesel relative ratio

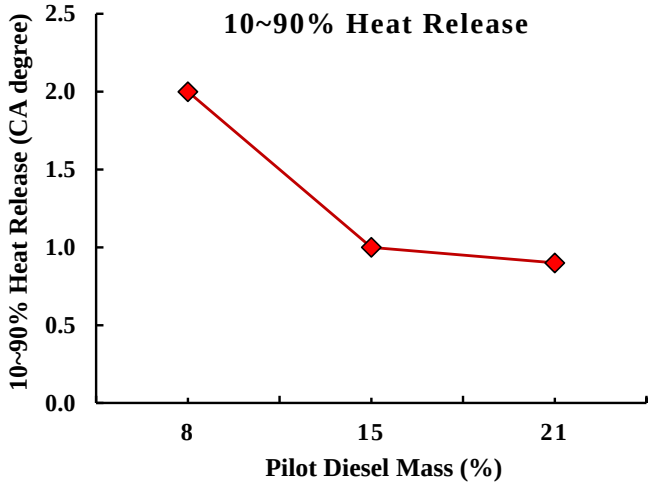

Fig. 5 Variation of main combustion duration with different gasoline-diesel relative ratio

In a dual-fuel engine, there exists pre-mixed gasoline fuel in the cylinder, therefore, the end gas may autoignite before the arrival of propagating flame front and thus SI engine type knocking may occur. Thus, shorter combustion duration is desirable in case of dual-fuel engines.

Fig. 5 shows that, main combustion duration, which is generally defined as the duration for 10% ~ 90% of the heat release, is getting longer when diesel pilot fuel is injected in lesser amount, i.e., for 8% diesel-92% gasoline case. This demonstrates that, introducing higher diesel fuel in the combustion zone accelerated the combustion reaction and subsequently led to shorter main combustion duration, which is preferable to suppress the tendency to engine knock.

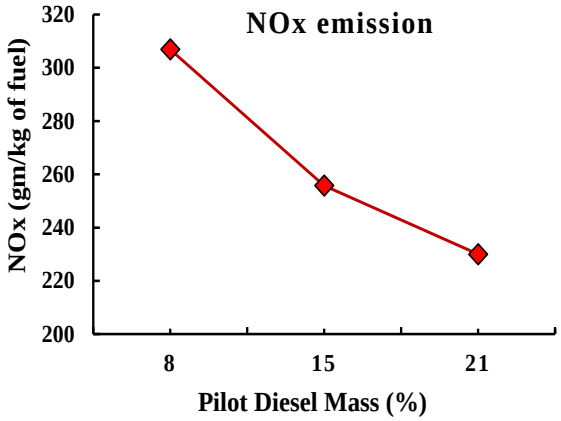

Fig. 6 Effect of gasoline-diesel relative ratio on NO formation

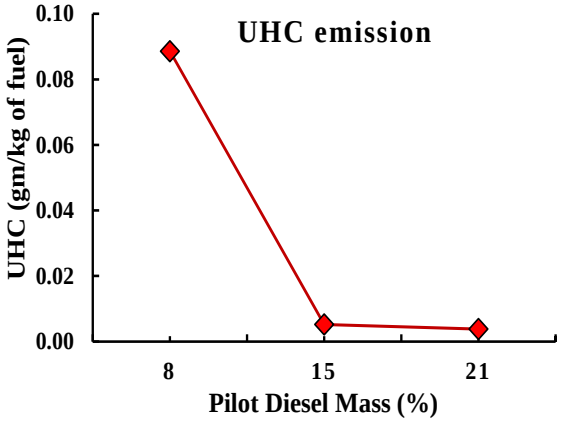

Fig. 7 Effect of gasoline-diesel relative ratio on UHC formation

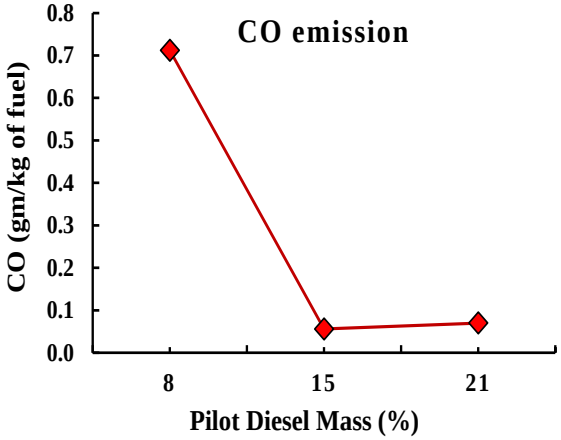

Fig. 8 Effect of gasoline-diesel relative ratio on CO formation

3.2 Effects of gasoline-diesel relative ratio on engine-out emissions

Fig. 6 to Fig. 8 represent the engine-out emissions of oxides of nitrogen, unburned hydrocarbon and carbon monoxide for different mass percentage of gasoline-diesel fuels.

It is evident from Fig. 6 that the higher percentage of gasoline led to higher level of NOx emission. Here, 92% gasoline - 8% diesel case resulted in highest NOx emission, whereas minimum NOx emission observed for 79% gasoline - 21% diesel case. Premixed flame (in this case gasoline flame) has generally much higher temperature than non-premixed/diffusion flame (i.e., diesel flame). Therefore, NOx emission is found to be higher as result of high temperature premixed flame associated with the increase of gasoline mass percentage. NOx formation is strongly influenced by two parameters namely, temperature and oxygen concentration as per Zeldovich mechanism; and it is found to increase exponentially with in-cylinder temperature [21].

8% diesel-92% gasoline case emits more unburned hydrocarbon (UHC) and carbon mono-oxide (CO) compared to that for 21% diesel-79% gasoline case. This might be attributed to the fact that flame propagation is not fast enough for lower percentage of diesel to consume all pre-mixed gasoline. Moreover, flame might be quenched earlier, therefore, some gasoline remained unburned near the cylinder wall or combustion became incomplete. Hence, both UHC and CO emissions level are found to be higher with greater percentage of gasoline.

4 Conclusions

In this study, the influences of gasoline-diesel relative ratio on combustion characteristics in terms of in-cylinder pressure, temperature, rate of heat release, combustion duration; and engine-out emissions of NOx, UHC and CO level from a single cylinder four-stroke dual-fuel engine was investigated through computational fluid dynamics (CFD) modeling. A commercially available software incorporated with highly efficient advanced chemistry solver module CHEMKIN is used to simulate the dual-fuel engine operation. Percentage of pilot diesel is varied arbitrarily from 8% to 21% by mass. A sector mesh of 60^{o} angle with periodic boundary conditions is considered instead of using the whole engine geometry in order to reduce the computational cost and time. The major findings of this modeling are summarized as follows:

- With the increase of pilot diesel fuel amount, more energy is released which resulted in higher in-cylinder pressure, in-cylinder temperature and rate of heat release.
- Autoignition of pilot fuel as well as onset of combustion occurred earlier when relative amount high reactivity pilot fuel (i.e., diesel) is increased compared to low reactivity fuel (i.e., gasoline). Besides, ignition delay period reduced with higher percentage of pilot fuel injection.
- Introducing higher amount of diesel fuel in the combustion zone accelerated the combustion reaction and subsequently led to shorter main combustion duration, which is preferable in dual-fuel engine to suppress the tendency to engine knock. Moreover, shorter main combustion duration could lead to higher thermal efficiency by reducing heat loss to cylinder wall.
- Higher percentage of gasoline led to higher level of NOx, UHC and CO emissions.

Acknowledgment

We sincerely acknowledge the support of the Department of Mechanical Engineering, Khulna University of Engineering & Technology (KUET) by providing the computing facility to conduct this CFD modelling.

References

[1] Kokjohn, S.L., Hanson, R.M., Splitter, D.A. and Reitz, R.D., 2010. Experiments and modeling of dual-fuel HCCI and PCCI combustion using in-cylinder fuel blending. *SAE International Journal of Engines, 2(2)*, pp.24-39.

[2] Dempsey, A.B. and Reitz, R.D., 2011. Computational optimization of reactivity controlled compression ignition in a heavy-duty engine with ultra low compression ratio. *SAE International Journal of Engines*, *4*(2), pp.2222-2239.

[3] Benajes, J., Molina, S., García, A., Belarte, E. and Vanvolsem, M., 2014. An investigation on RCCI combustion in a heavy duty diesel engine using in-cylinder blending of diesel and gasoline fuels. *Applied Thermal Engineering*, *63*(1), pp.66-76.

[4] Park, S.H., Yoon, S.H. and Lee, C.S., 2014. Bioethanol and gasoline premixing effect on combustion and emission characteristics in biodiesel dual-fuel combustion engine. *Applied energy*, *135*, pp.286-298.

[5] Jeftić, M. and Zheng, M., 2015. A study of the effect of post injection on combustion and emissions with premixing enhanced fueling strategies. *Applied Energy*, *157*, pp.861-870.

[6] Fraioli, V., Mancaruso, E., Migliaccio, M. and Vaglieco, B.M., 2014. Ethanol effect as premixed fuel in dual-fuel CI engines: experimental and numerical investigations. *Applied energy*, *119*, pp.394-404.

[7] Guerry, E.S., Raihan, M.S., Srinivasan, K.K., Krishnan, S.R. and Sohail, A., 2016. Injection timing effects on partially premixed diesel–methane dual fuel low temperature combustion. *Applied energy*, *162*, pp.99-113.

[8] Yang, B., Xi, C., Wei, X., Zeng, K. and Lai, M.C., 2015. Parametric investigation of natural gas port injection and diesel pilot injection on the combustion and emissions of a turbocharged common rail dual-fuel engine at low load. *Applied Energy*, *143*, pp.130-137.

[9] Dimitriou, P., Tsujimura, T., Kojima, H., Aoyagi, K., Kurimoto, N. and Nishijima, Y., 2021. Experimental and Simulation Analysis of Natural Gas-Diesel Combustion in Dual-Fuel Engines. *Advances in Compression Ignition Natural Gas–Diesel Dual Fuel Engines*.

[10] Pham, V.C., Choi, J.H., Rho, B.S., Kim, J.S., Park, K., Park, S.K., Le, V.V. and Lee, W.J., 2021. A Numerical Study on the Combustion Process and Emission Characteristics of a Natural Gas-Diesel Dual-Fuel Marine Engine at Full Load. *Energies*, *14*(5), p.1342.

[11] Mousavi, S.M., Saray, R.K., Poorghasemi, K. and Maghbouli, A., 2016. A numerical investigation on combustion and emission characteristics of a dual fuel engine at part load condition. *Fuel*, *166*, pp.309-319.

[12] Ma, J., Lü, X., Ji, L. and Huang, Z., 2008. An experimental study of HCCI-DI combustion and emissions in a diesel engine with dual fuel. *International Journal of Thermal Sciences*, *47*(9), pp.1235-1242.

[13] Micklow, G.J. and Gong, W., 2002. Mechanism of hydrocarbon reduction using multiple injection in a natural gas fuelled/micro-pilot diesel ignition engine. *International Journal of Engine Research*, *3*(1), pp.13-21.

[14] Mattarelli, E., Rinaldini, C.A. and Golovitchev, V.I., 2014. CFD-3D analysis of a light duty Dual Fuel (Diesel/Natural Gas) combustion engine. *Energy Procedia*, *45*, pp.929-937.

[15] López, J.J., Novella, R., García, A. and Winklinger, J.F., 2013. Investigation of the ignition and combustion processes of a dual-fuel spray under diesel-like conditions using computational fluid dynamics (CFD) modeling. *Mathematical and Computer Modelling*, *57*(7-8), pp.1897-1906.

[16] Cha, J., Kwon, S. and Park, S., 2011. An experimental and modelling study of the combustion and emission characteristics for gasoline–diesel dual-fuel engines. *Proceedings of the Institution of Mechanical Engineers, Part D: Journal of Automobile Engineering*, *225*(6), pp.801-812.

[17] Puduppakkam, K.V., Liang, L., Naik, C.V., Meeks, E., Kokjohn, S.L. and Reitz, R.D., 2011. Use of detailed kinetics and advanced chemistry-solution techniques in CFD to investigate dual-fuel engine concepts. *SAE International Journal of Engines*, *4*(1), pp.1127-1149.

[18] https://combustion.llnl.gov/archived-mechanisms/surrogates/prf-isooctane-n-heptane-mixture [Accessed on 06-Mar-2020].

[19] Peters, N., Turbulent Combustion. Cambridge University Press: Cambridge, UK, 2000.

[20] Tan, Z., Reitz, R.D., 2006. An Ignition and Combustion Model for Spark Ignition Engine Multi-Dimensional Modeling. *Combustion and Flame*, *145*, pp. 1-15.

[21] Heywood, J.B., Internal Combustion Engine Fundamentals. McGraw-Hill Publications: New York, USA, 1988.

SciEn
Journal of Engineering Advancements Vol. 02(03) 2021, pp 153-158 https://doi.org/10.38032/jea.2021.03.005

Detection of Glaucoma using ORB (Oriented FAST and Rotated BRIEF) Feature Extraction

Kazi Safayet Md. Shabbir[1], Md. Imteaz Ahmed[2], Marzan Alam[1]*

[1]Department of Mechatronics and Industrial Engineering, Chittagong University of Engineering and Technology, Chattagram-4349, Bangladesh
[2]Department of Mechanical Engineering, Chittagong University of Engineering and Technology, Chattagram-4349, Bangladesh

Received: June 14, 2021, Revised: August 02, 2021, Accepted: August 09, 2021, Available Online: August 23, 2021

ABSTRACT

This research was utilized to identify glaucoma, a type of eye illness. This endeavor necessitates the use of pictures from the fundus camera for image processing. This study reflects the effort done to detect glaucoma-affected eyes utilizing image feature extraction using Oriented FAST and Rotated BRIEF (ORB). ORB is a binary descriptor approach that is based on BRIEF and is highly fast. This technique is insensitive to picture noise and is invariant to any rotation. ORB is two orders of magnitude faster than SURF and performs similarly to SIFT. It is more efficient than other texture analysis methods. It is less computationally difficult than other approaches in the literature. This technique extracts features and detects texture by inspecting each pixel of the retina picture. It was trained on 160 fundus pictures of normal and glaucoma-affected retinas. After that, any healthy or glaucoma-affected eye may be easily recognized by obtaining an accurate eye picture. The results reveal that this technique has a precision and accuracy of more than 90%.

Keywords: ORB, Glaucoma, Fundus, SIFT, Python.

1 Introduction

In 1622 English oculist Richard Bannister was the first person who found out the elevation of Intraocular Pressure (IOP) that causes tension in the eyeball and termed it as glaucoma [1]. Glaucoma causes blindness if it is ignored and there is no way of detecting an affected eye without taking a fundus image of the retina. As glaucoma does not have any symptoms and there is no single test to detect people with glaucoma [2] it became the third leading reason for blindness throughout the globe. A source implies that 4.5 million people across the world have been blinded because of glaucoma [3]. Based a surveillance study in 2004 in Dhaka, Bangladesh shows that approximately 586,000 people are definitely or probably suffering from glaucoma [4]. That's why early detection of glaucoma can be a great solution to prevent blindness. This leads to a screening-based program to classify glaucoma-affected retina. Screening-based programs require a retinal image of the patient and an optometrist will decide if the patient needs any medical attention furthermore. This is the only solution to detect glaucoma at its early stage and any kind of optical surgery (like laser treatment or implementing drainage) relating to glaucoma can be avoided to preserve the quality of the patient's life and medical cost as well. Present techniques to detect glaucoma are not cost-effective so that, implementation of these techniques can be expensive. If the methods are improved it can drastically reduce the cost and make the implementation easier.

The diagnosis of glaucoma can be done using three essential tests. Firstly, Tonometry includes the measurement of Intraocular Pressure (IOP). But the thing is there is no difference in the value of IOP so that it is not possible to discriminate between healthy and glaucomatous eyes [2]. Secondly, visual field testing is a subjective and most sensitive examination if used as a screening test [5]. But there is a handicap of this method, it needs comparatively more time to run the whole test, highly developed equipment, and an operator who will guide the subject during the test. Most of the patients found this task difficult to perform and 90% of the patients aging 40 years could perform the screening test properly. The success rate drastically decreases to 71% for patients aging more than 70 years [2]. Finally, the nerve layer or optic disc examination can be the procedure of choice for screening tests of glaucoma. To perform this test fundus camera or 3D imaging tool is necessary to detect the signs of glaucoma in the retina. 3D imaging tool has an advantage over the fundus camera as it can gather data of the optical disc on a 3D perspective measurement.

Cup depth of the retina is one of the most common indicators of glaucoma that can easily be measured. This is a more accurate approach to detect glaucoma. Besides being able to measure such things 3D imaging tools are expensive and not suitable for large-scale implementation. Therefore, computer-aided diagnosis (CAD) using screening tests of fundus images is more acceptable because of its availability and cost-efficiency. In this paper, the fundus image has been used to detect glaucoma-affected eyes. The method used in this work is feature detection based on Oriented FAST and Rotating BRIEF (ORB) which is more suitable for this task than other feature extraction methods like SIFT or SURF [6]. This process uses each pixel of the image, unlike other methods that use specific regions of the image to perform the task.

The paper has been organized as follows, Section II includes a Literature review about the previous work done in this field. Section III describes the method that has been used to perform the task of detection. Section IV represents the result found in the experiment and the conclusion about it.

*Corresponding Author Email Address: imteaz@cuet.ac.bd

2 Literature Review

All of the previous work that has been published can be categorized into two sections, fractionalizing the retinal objects, on the other hand, classifying it with the help of features in the image. To imply the first category segmentation is needed of the patient's retina so that it can get the structure of it. From the structure, some parameters define the healthy retina and glaucomatous retina through calculation. It is cupping that is damaged due to glaucoma in the retina. This is one of the main things that is considered as the main features alongside with image of the optic disc and blood vessels' retinal image.

In the early days, various Greek medical literature described glaucoma as an incurable disease [7]. But through numerous medical and technological researches now it has become curable. The first approach to cure this disease was to decrease IOP using drugs that were discovered in a study of intraocular hemorrhage control [8]. All the work was related to curing glaucoma but the hardest part was to detect it before it starts damaging the eye. In the late 19th century blue on yellow perimetry was a successful method of detecting glaucoma in its early stage [9].

Enlarging of the optical disc is what happens in the optical nerve system because of glaucoma. This is why the cup to disc ratio (CDR) varies for normal vs. affected eyes (See Fig. 1). Disc size does not affect detecting glaucoma and it was found in a study of open-angle glaucoma [10]. Moreover, emission of blood occurs in the optic disc and retinal disc, the retinal layer gets thinner, and the retinal nerve fiber layer (RNFL) gets defected. Calculating CDR and RNFL there is a method to detect glaucoma [11]-[12]. The ratio between the vertical diameter of the optic and disc is known as CDR, which is most commonly used for detecting glaucoma and must needed measurement parameter for segmentation.

CDR is very sensitive to glaucoma that has made an opportunity to examine it as this represents the deformation inside the optic cup. Detection of CDR can be automatically done that is proposed by a study [13]. The high value of CDR means a large optic disk, which happened due to glaucoma affection inside the retina [14]. But there are some exceptions found in some research like, CDR in some cases act like a continuous variable that is distributed as IOP [2]. This can turn into a conclusion like this, Small CDR valued patients might face vision loss or vice versa [15]. To avoid this kind of miscalculation CDR of both optic disc is needed to make sure if the disc size of the retina is large or not.

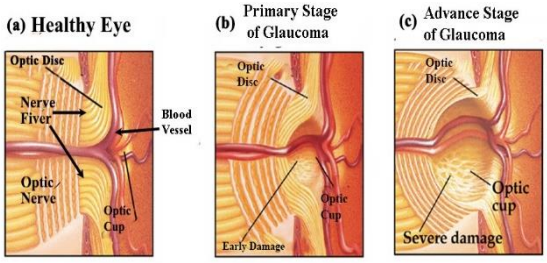

Fig. 1 Cupping in glaucomatous damage. a) Normal disc with small cup region, b) disc with early glaucoma, and c) disc with advanced glaucoma.

Accurate segmentation that has been taken from both of the eyes of the patient is mandatory for CDR-based methods used for detecting glaucoma [16]. Misdiagnosis may occur if there is an error in measuring CDR value or in segmentation, thus taking these values accurately is vital. It is very difficult to get the correct segmentation of the retinal image as the optic disc size varies according to optic cups. Perfect segmentation results in sensitive, specific, and accurate glaucoma detection and it is tough to achieve. A method was developed to estimate the amount of damage done by glaucoma, it used fundus images of the eye [17]. The difficulties arise because of the low contrast created by the blood vessels of the retina in the fundus image around the area of the optic cup/disc.

The specific field of this computer-aided diagnosis is a classification of the fundus image using image processing to achieve the highest accuracy possible. Several works had been done to achieve this goal. Using colored fundus Image automatic glaucoma detection method was proposed using Image processing [18]. Wavelet-based classification is used in a study to extract features of glaucoma for detection [19]. Another image processing-based work that has been done is Histogram of Oriented Gradients (HoG) using the Naive Bayes method of classification [20]. The automatic system for analyzing the retinal images to detect glaucoma was in 2014 [21]. This work was about the depth discontinuity in the retinal surface.

All the present works relating to glaucoma are based on the researches above. As the process of detecting glaucoma is convenient with image processing there have been several works done in this field. Various image processing method has been applied to analyze the texture of glaucoma or classify glaucoma from the fundus image. Texture analysis has been done using the Binary Robust Independent Elementary Feature (BRIEF) method [22]. BRIEF is a binary-based descriptor that has a high success rate in texture analysis. In this paper, the method used is a BRIEF-based feature detection and tracking system called ORB. The advantage of using this method is quick response, no issue with blood vessel contrast of the image, and higher accuracy than any methods that have been used till now to pursue this work. So, to get better accuracy and precision this method has been used in this study.

3 Methodology

The whole process is done using the python language and using library of it. The colored fundus image from the fundus camera is where the work starts from. The method using here uses pixel by pixel of the image that helps to gain more accuracy with less complexity. After splitting the image's colors using the green channel gave a spectacular result while gathering features of the images that has been used. Histogram equalization intensified the features of the images that are useful for extracting features.

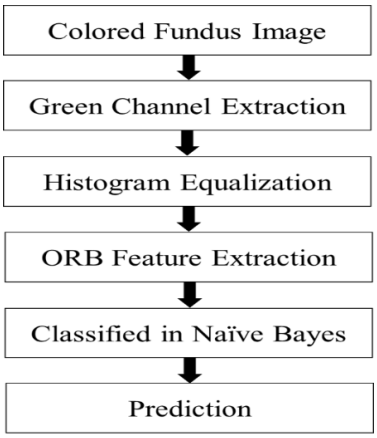

Fig. 2 Detecting Glaucoma using ORB

After processing the image, Oriented FAST and rotated the BRIEF (ORB) method has used for extracting features. Then organized those extracted features in stacks and fed them to Naïve Bayes for classification and training the model. Finally, that model predicts images if they have glaucoma or they are healthy. The whole process is shown in Fig. 2.

3.1 Image Preprocessing

This section is divided into two steps. At first, green channel extraction and then equalization of the histogram. All these processes are done in a python language environment. Fig. 3 is an example image that will be used for further explanation. Applying all the steps used in this method into this image other steps can be easily described.

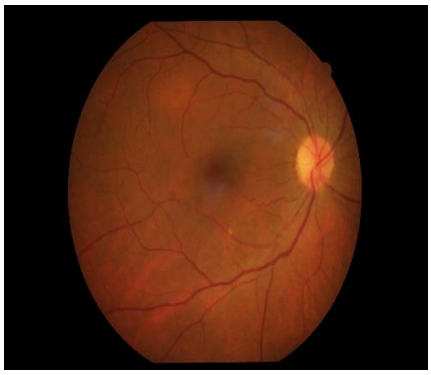

Fig. 3 Colored Fundus Image

3.2 Green Channel Extraction

First, it splits images using the library and then use various channels of colors Blue, Green, and Red. After that green channel gives better results in terms of extracting features than the other two channels. Using library read the colored fundus image at first, then using image slice a 2D array extracts green channel from the image. This is a part of pre-processing the image and getting it ready for feature extraction.

After using the green channel extraction operation of the fundus image it appears to be like Fig. 4.

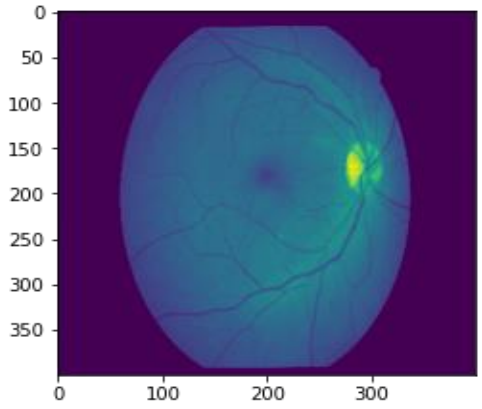

Fig. 4 Green Channel Extraction in Pre-processing the fundus image

This image was resized in (400,400) pixels and then we use a split function from the library to get three separate channels. Then we used the green channel and that's why the image is greenish. But the image is not clear enough for extracting features from it, which is when the Histogram Equalization is required.

3.3 Histogram Equalization

Histogram equalization is required to make sure of using all the features an image contains that is important in image processing. It stretches the histogram of the image to get the right pixel value in all regions of the image so that it intensifies the clarity of the image so all the features are visible for extraction.

For histogram equalization, there are various functions. It has a dedicated function for histogram equalization but it has some limitations in a highly contrasted image where the image has a higher histogram region with both types of pixels: dark and bright. To solve this problem, Contrast Limited Adaptive Histogram Equalization (CLAHE) is used in our method. CLAHE requires a clip limit of the image and uses the title grid size of the photo to enhance its histogram. Using clip limit and grid size the image is distributed into small tiles. In OpenCV the default tiles size is 8x8 and this method uses this size as well. After getting those 8x8 pixel tiles it equalizes the histogram in that small region. To avoid any noise enhancement of the tiles contrast limiting is used that has a default value, 40. Before equalizing the histogram, it limits the contest value and distributes those clipped pixels evenly to further bins. If any artifacts appear in those 8x8 tiles border, using bilinear interpolation it is removed in this method of histogram equalization. Therefore, using this function in images with higher histograms results in a more evenly distributed histogram both in the foreground and the background of the image.

The green channel extracted image after applying CLAHE is shown in Fig. 5. It has become more visible and more detailed that is required for a better feature extraction process.

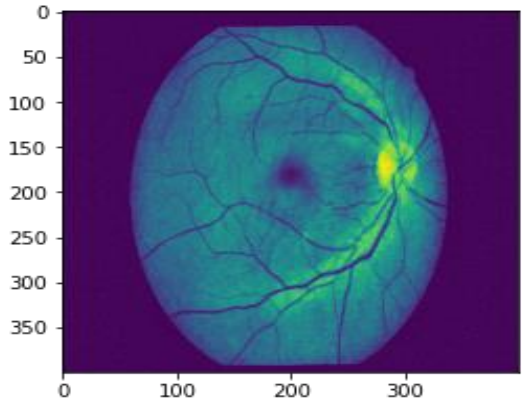

Fig. 5 Equalizing Histograms using CLAHE function

3.4 Feature Extraction

Oriented FAST and Rotated BRIEF (ORB) is our feature extraction method for texture analysis of the fundus image. ORB is a highly modified combination of two methods Features from Accelerated Segment Test (FAST) and Binary Robust Independent Elementary Feature (BRIEF). From FAST it gets key points as it is a corner detection method and from BRIEF, we get descriptor. ORB uses them to enhance their performance and overcome the limitations of FAST that is it can't calculate the orientation of the image.

Locating the patch of the corner in the center, it calculates the centroid based on intensity weight, taking vector from the corner point and centroid gives the direction. Therefore, orientation is achieved from it. With respect to X and Y moments of the rotation are calculated that have a radius of '***r***', which improves the invariance of rotation. Here '***r***' represents the size

of the path. Using the key points found in the Oriented FAST method BRIEF is steered to overcome its limitations of performance in terms of rotation. If the feature set of binary tests in BRIEF is 'm' and the location is (x_i, y_i) makes a 2 × m matrix. The coordinates of the pixels are stored in 'S'. A rotation matrix S_θ is found using θ that implies the orientation of the patch.

In ORB it creates a progress table of previously calculated BRIEF patterns separating the angle with increments of 12 degrees ($2\pi/30$). S_θ will be used further as long as the key point orientation θ is used. When rotated according to those key points BRIEF gets more distributed and loses its important property of having higher variance and 0.5 mean value of each bit features. Plus point of having high variance is it helps the feature to be more discriminatory as it is response distinctively to inputs. There is another important property needed for the feature extraction which is having all the tests uncorrelated. To gain these absent properties ORB method performs a greedy search among all the binaries found after rotating the BRIEF according to key points. This greedy search finds out all the possible binaries that have large variance and means closer to 0.5 and makes these tests uncorrelated. This modified BRIEF is known as rBRIEF or Rotated BRIEF. To achieve matching in the descriptor, multi-probe Locality Sensitive Hashing (LSH) is used that has improved output than usual LSH.

To use ORB in python it just needed to call as function. This function extracts features from the pre-processed image. The number of features extracted in this method is 500. Key points and descriptors are found as output after computing them from the pre-processed fundus image, this method used the descriptor for further use. The number of features taken in descriptors here is [0:200]. Then those descriptors are stacked from each image one after another after running it through the ORB function. With 160 images going through the ORB function the number of features in stacked descriptor is 6400. Fig. 6 shows how the image looks after running it through the ORB feature extractor function.

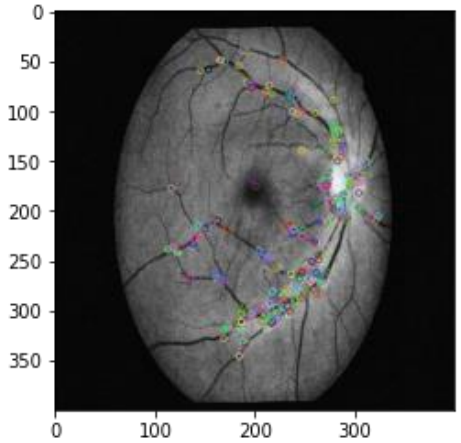

Fig. 6 Feature extraction using ORB method

After stacking those descriptors, a model is trained using machine learning. Here 80 fundus images were healthy and the other 80 were glaucoma-affected images. Classifying those images further work has been done.

3.5 Classification

Gaussian Naïve Bayes is a popular method of classification that can be easily used in Python through 'sklearn' library's datasets. Naïve Bayes is a technique used in statistical classification. It is based on Bayes Theorem which is used for predicting an outcome based on the data given. This simplifies the Bayes theorem and uses that for prediction and this is why it is known as Naïve Bayes. The equation is as follow:

$$f\left(\frac{h}{D}\right) = \frac{f\left(\frac{D}{h}\right) f(h)}{f(D)} \qquad (1)$$

Here, $f(D)$ represents the probability of the data D regardless of the hypothesis that is prior probability here.

$f(h)$ Represents the probability of h being true, which means hypothesis in regardless of given data. This is the prior probability of h.

$f\left(\frac{D}{h}\right)$ is the probability of h being true on basis of the data D given. It is called posterior probability.

$f\left(\frac{h}{D}\right)$ is the probability of h being true based on given the data D. this is also known as posterior probability.

First of all, it calculates the prior probabilities for the class given. Secondly, it finds any similar probability for that label of the given class. Thirdly, it puts all those values in the Bayes formula to find out posterior probability. Lastly, it finds out which class shows the higher possibility of being true, then marks it as result.

In this work, we fed data as features that are found from ORB extraction and trained our model using Naïve Bayes. The desired output for detecting glaucoma is defined as Glaucoma =0, Healthy =1. Therefore, the trained model will show the result as 0 or 1 after processing the image used as input and predict if that image contains glaucoma or not.

4 Simulation Results & Discussion

The method proposed above has been applied with the help of the fundus image collected. This helped to train the model properly in a python-based environment 'Jupyter Notebook'. To train this model we used 80 healthy fundus images and 80 glaucoma-affected fundus images. With the help of the ORB feature extraction method, we took [0:200] features and kept them in a descriptor. Then stacking those one by one in an array helped to train the model with the help of machine learning. Then the model used Gaussian Naïve Bays to predict normal or healthy eye and glaucoma affected eye based on the fundus image used as input.

To validate this classifier we calculated error rate, specificity, precision, and recall/sensitivity value. To calculate these values, 30 glaucoma-affected fundus images and 30 healthy fundus images were inputted into the trained model for prediction. This is what was found shown in Table 1.

Table 1 Confusion matrix of gaussian naïve bayes using ORB extraction method

	Predicted Glaucoma	Predicted Healthy	Total Act.
Actually Glaucoma	TP=28	FP=2	30
Actually Healthy	FN=3	TN=27	30
Total			60

In ORB key points and descriptors are found, descriptors are what stores features from the images using rBRIEF method. These descriptors are used to train the model and these are the things that help to predict the input image. In Table 1, TP

represents the true positive numbers & FP means the false positive numbers. Which means running 30 previously known glaucoma affected images as input in the prediction model we get 28(TP) correct result finding them as glaucoma affected and 2(FP) incorrect finding them as healthy. Similarly, for 30 healthy images running into the model as input, false-negative was 3 images, which means 3 images are detected as glaucoma affected though they are healthy, and 27 images are found true negative, which means correctly predicted them as healthy image.

Here,

Accuracy = $\frac{TP+TN}{Total}$ …… (2) = 91.67%

Error rate = $\frac{FP+FN}{Total}$ …… (3) = 8.3%

Specificity = $\frac{TN}{Total\ Act.\ Healthy}$…..(4) = 90%

Precision= $\frac{TP}{Total\ Act.\ Glaucoma}$….. (5) = 93.3%

Recall = $\frac{TP}{TP+FN}$ ……..... (6) = 90.32%

Table 2 Analyzing the performance of different methods

Methods	Recall	Specificity	Accuracy	Precision
Wavelet	85.45	87.54	86.67	83.33
WBCT	81.34	88.73	84.53	85.54
Contourlet	74.36	80.20	78.84	76.84
HoG	88.89	75	75	89.20
ORB	90.32	90	91.67	93.3

Table 3 Comparing ORB with other studies

Author	Methodology	Total Image	Classification method	Accuracy	Recall
Bock et al. [18]	Value of pixel intensity, spectran and texture features	200	NB, SVM, KNN	86%	N/A
Dua et al. [19]	Features of wavelet energy	60	NB, SVM, SMO, Random forest	86.67%	85.54%
Krishnan et al. [23]	DWT and Higher order spectra trace transform	60	SVM	91.70%	90%
Kolar et al. [24]	Fractal features	30	SVM	74%	N/A
Townsend et al. [25]	Detection based on HTR	200	SVM	87.50%	N/A
Nirmal et al. [20]	Features of HoG based detection	101	NB	75%	88.89%
Proposed method	ORB feature extraction method	160	GNB (Python)	91.67%	90.32%

Comparing these values with other works previously done we get that accuracy of our work is better than them. The accuracy of Wavelet-based classification is 86.67%, Contourlet-based work had 78.84%, WBCT had 84.53%, HoG feature had 75% based on their confusion matrix provided. This ORB method Gained 91.6% accuracy. Recall of Wavelet-based classification is 85.45%, Contourlet-based work had 74.36%, WBCT had 81.34%, HoG feature had 88.89% based on their confusion matrix provided. This ORB method Gained 93.32% recall. Specificity of Wavelet-based classification is 87.54%, Contourlet-based work had 80.20%, WBCT had 88.73%, HoG feature had 75% based on their confusion matrix provided. This ORB method gained a 91.6% recall rate. Calculating the error rate of HoG based classification of its confusion matrix the rate found is 10% where ORB has an 8.3% error rate.

5 Conclusion

From this paper, it is clear that ORB feature extraction has higher accuracy, less complexity, highest sensitivity, and lowest error rate. The reason behind using this method is it's faster than other methods used before and less complex to use. The accuracy in texture analysis is high as well. Moreover, SURF and SIFT methods are patented, so paying the patent holders is required to use those methods. Because of using Gaussian Naïve Bayes in python, the prediction method becomes easier. OpenCV has various mathematical functions that are easier to use in python comparing to other platforms. ORB overcame all the limitations of the FAST and BRIEF method and faster than other feature extraction. The accuracy gained by the model we trained from 160 images is 91.67% and sensitivity or recall is 90.32% that is higher than other compared studies. Moreover, ORB can be used in any low-powered device, these reasons are what makes it a better choice than other methods.

References

[1] Banister, R., 1971. A treatise of one hundred and thirteene diseases of the eyes (No. 297). Theatrum Orbis Terrarum.

[2] Rotchford, A., 2005. What is practical in glaucoma management?. *Eye*, *19*(10), pp.1125-1132.

[3] www.sightsavers.org/protecting-sight/what-is glaucoma/ Accessed on 24.04.2021

[4] Rahman, M.M., Rahman, N., Foster, P.J., Haque, Z., Zaman, A.U., Dineen, B. and Johnson, G.J., 2004. The prevalence of glaucoma in Bangladesh: a population based survey in Dhaka division. *British Journal of Ophthalmology*, *88*(12), pp.1493-1497.

[5] Katz, J., Sommer, A., Gaasterland, D.E. and Anderson, D.R., 1991. Comparison of analytic algorithms for detecting glaucomatous visual field loss. *Archives of Ophthalmology*, *109*(12), pp.1684-1689.

[6] Rublee, E., Rabaud, V., Konolige, K. and Bradski, G., 2011, November. ORB: An efficient alternative to SIFT or SURF. In *2011 International Conference on Computer Vision* (pp. 2564-2571). IEEE.

[7] Laios, K., Moschos, M.M. and Androutsos, G., 2016. Glaucoma and the origins of its name. *Journal of Glaucoma*, *25*(5), pp.e507-e508.

[8] Krupen, T., 1997. Autonomic drugs: controlling the inflow. *van Buskirk EM, Shields MB, eds*, *100*, pp.262-71.

[9] Johnson, C.A., Adams, A.J., Casson, E.J. and Brandt, J.D., 1993. Blue-on-yellow perimetry can predict the development of glaucomatous visual field loss. *Archives of Ophthalmology*, *111*(5), pp.645-650.

[10] Jonas, J.B., Gusek, G.C. and Naumann, G.O., 1988. Optic disc morphometry in chronic primary open-angle glaucoma. *Graefe's Srchive for Clinical and Experimental Ophthalmology*, *226*(6), pp.522-530.

[11] Nayak, J., Acharya, R., Bhat, P.S., Shetty, N. and Lim, T.C., 2009. Automated diagnosis of glaucoma using digital fundus images. *Journal of Medical Systems*, *33*(5), pp.337-346.

[12] Muramatsu, C., Fujita, H., Nakagawa, T., Sawada, A., Yamamoto, T. and Hatanaka, Y., 2011. Automated determination of cup-to-disc ratio for classification of glaucomatous and normal eyes on stereo retinal fundus images. *Journal of Biomedical Optics*, *16*(9), p.096009.

[13] Wolfs, R.C., Ramrattan, R.S., Hofman, A. and de Jong, P.T., 1999. Cup-to-disc ratio: ophthalmoscopy versus automated measurement in a general population: The Rotterdam Study. *Ophthalmology*, *106*(8), pp.1597-1601.

[14] Varma, R., Steinmann, W.C. and Scott, I.U., 1992. Expert agreement in evaluating the optic disc for glaucoma. *Ophthalmology*, *99*(2), pp.215-221.

[15] Douglas, G.R., GR, D. and SM, D., 1974. A correlation of fields and discs in open angle glaucoma. *Can J Ophthalmol*, 9(4):391-8

[16] Lim, C.S., O'brien, C. and Bolton, N.M., 1996. A simple clinical method to measure the optic disc size in glaucoma. *Journal of Glaucoma*, *5*(4), pp.241-245.

[17] Spaeth, G.L., Henderer, J., Liu, C., Kesen, M., Altangerel, U., Bayer, A., Katz, L.J., Myers, J., Rhee, D. and Steinmann, W., 2002. The disc damage likelihood scale: reproducibility of a new method of estimating the amount of optic nerve damage caused by glaucoma. *Transactions of the American Ophthalmological Society*, *100*, p.181.

[18] Bock, R., Meier, J., Nyúl, L.G., Hornegger, J. and Michelson, G., 2010. Glaucoma risk index: automated glaucoma detection from color fundus images. *Medical Image Analysis*, *14*(3), pp.471-481.

[19] Dua, S., Acharya, U.R., Chowriappa, P. and Sree, S.V., 2011. Wavelet-based energy features for glaucomatous image classification. *IEEE Transactions on Information Technology in Biomedicine*, *16*(1), pp.80-87.

[20] Nirmala, K., Venkateswaran, N. and Kumar, C.V., 2017, November. HoG based Naive Bayes classifier for glaucoma detection. In *TENCON 2017-2017 IEEE Region 10 Conference* (pp. 2331-2336). IEEE.

[21] Joshi, G.D., 2014. Automatic retinal image analysis for the detection of glaucoma. *International Institute of Information Technology*.

[22] Mohammad, S. and Morris, D.T., 2015, May. Texture analysis for glaucoma classification. In *2015 International Conference on BioSignal Analysis, Processing and Systems (ICBAPS)* (pp. 98-103). IEEE.

[23] Krishnan, M.M.R. and Faust, O., 2013. Automated glaucoma detection using hybrid feature extraction in retinal fundus images. *Journal of Mechanics in Medicine and Biology*, *13*(01), p.1350011.

[24] Kolář, R. and Jan, J., 2008. Detection of glaucomatous eye via color fundus images using fractal dimensions. *Radioengineering*, *17*(3), pp.109-114.

[25] Townsend, K.A., Wollstein, G., Danks, D., Sung, K.R., Ishikawa, H., Kagemann, L., Gabriele, M.L. and Schuman, J.S., 2008. Heidelberg Retina Tomograph 3 machine learning classifiers for glaucoma detection. *British Journal of Ophthalmology*, *92*(6), pp.814-818.

SciEn
Journal of Engineering Advancements Vol. 02(03) 2021, pp 159-163 https://doi.org/10.38032/jea.2021.03.006

Design Optimization of B-series Marine Propeller using NSGA-II, Iterative and Gekko Algorithm

S. M. Munawar Mahtab, Debasish Roy, M. S. Rabbi, Md. Iftekharul Alam*

Department of Mechanical Engineering, Chittagong University of Engineering and Technology, Chattogram-4349, Bangladesh.

Received: July 02, 2021, Revised: August 17, 2021, Accepted: August 23, 2021, Available Online: August 31, 2021

ABSTRACT

The design of a propeller plays a significant role in naval architecture. Optimization of various design factors is the primary concern for effective and efficient propulsion. This study investigates the optimization of the B-series marine propellers using three different methods, i.e. (i) a non-linear constrained single-objective optimization approach using the Non-Dominated Sorting Genetic Algorithm (NSGA-II), (ii) a python package for dynamic optimization based optimization software 'Gekko', (iii) an iterative approach and results were compared with each other. Efficiency is considered as the single objective function whereas three constraints are imposed: cavitation, thrust and strength. Analogous characteristics have been found in the comparison of results from all three methods. Comparing the various factors, this study suggests that, Gekko can be used as the optimization algorithm.

Keywords: Optimization, B-series Propeller, NSGA-II, Iterative, Gekko.

1 Introduction

In naval architecture, the propeller design plays a significant role in naval architecture. Marine propellers are operated in non-uniform flow of water and thus complex to be modelled the environment and analysed. Performance of a marine propeller depends on numerous parameters such as thrust, cavitation, material strength, geometry, shape etc. Optimization of the theoretically designed marine propellers is a way to increase the performance and hence, the efficiency. The constrained single objective optimization has been used in this study for optimization. In this method, a single parameter considered as an objective and other parameters can be taken as design constraints [1].

Among numerous algorithms, Genetic algorithm i.e. Non-Dominated Sorting Genetic Algorithm (NSGA-II), and iterative algorithm follow the evolutionary approach to investigate the optimized solution for a given problem taking in consideration various constraints and the main objective. Xie [2] adopted multi-objective optimization approach where efficiency ratio and thrust coefficient were taken as objectives. To avoid the dangerous effects of increased cavitation, it was kept as a constraint. Gaafary et al. [3] developed an algorithm to find out optimum design parameters of B-series propellers where the single objective optimization approach has been adopted keeping propeller thrust, material strength, and cavitation as constraints to maximize efficiency. Theoretical findings were compared with the results found from the commercial software.S. Mirjalili et al. [4] used multi-objective optimization where efficiency was taken as a maximization function and cavitation was taken as a minimization function. It was found that the efficiency increases proportional to the number of blades up to a limit of 5 blades and cavitation also decreases proportional to the number of blades. Windyandari et al. [5] investigated the Indonesian purse seine boats to find optimized design of marine propellers which will improve thrust performance of the traditional purse seine boats.

Oosterveld et al. [6] performed a multi-regressional analysis using some open-water test data of B-series propellers. These regression analysis data can be used to design the propeller in marine engineering. Suen et al. [7] used genetic algorithm to find out optimum design parameters for B-series marine propellers. Main objective of the optimization was maximization of efficiency using non-linear constraints. The results achieved using genetic algorithm was compared with results of iteration method. It was observed that genetic algorithm yielded higher efficiency and more reliable result than the iteration method. Benini et al. [8] carried out a multi-objective design optimization experiment for marine propellers. The two objectives of the optimization were maximization of open-water efficiency and thrust coefficient. Result of the study showed that the two objectives conflicts each other.

In the present study, optimization of the B-series marine propeller is investigated using dynamic optimization package Gekko, based on python programming language. To verify the technique, the popular optimization methods stated in the review, NSGA-II and iterative algorithms have also been conducted and consequently. In this optimization procedure, a single objective optimization approach was adopted where cavitation, material strength and thrust requirements were defined as constrains. The objective function was maximization of efficiency. To make a comparison with the three methods the issue was imposed as single objective since the iterative algorithm was specially designed for constrained single objective optimization. The results were compared considering computing cost, time, and efficiency.

The mathematical representation of design objective and constraints are mentioned in Section 2. Various optimization algorithms are explained in this section as well. Section 3 contained the numerical simulation parameters. Depiction of result and their illustrations are presented in Section 4. Conclusions are drawn in Section 5.

*Corresponding Author Email Address: rabbi@cuet.ac.bd Published by: SciEn Publishing Group

2 Optimization Problem

2.1 Design Objective

To optimize the marine propeller, maximization of efficiency is the main objective function, considered in this study. The open water efficiency of marine propellers is calculated using the following equations:

$$\eta = \frac{J}{2\pi}.\frac{K_T}{K_Q} \tag{1}$$

and

$$J = \frac{V_S(1-w)}{nD} \tag{2}$$

where K_T and K_Q are thrust coefficient and torque coefficient respectively. J is the advanced coefficient and V_S is the service speed.

2.2 Design Constraints

In the constrained single objective optimization technique, important parameters that are interrelated with the performance of a marine propeller needed to be defined as constraints. Cavitation is one of the crucial parameters depends on blade area ratio. Cavitation can be avoided by increasing the blade area ratio and the minimum blade area ratio can be calculated using the following equation [9]:

$$\left[\frac{A_E}{A_O}\right]_{min} = \frac{(1.3+0.3Z)T}{(P_O - P_V)D^2} + K \tag{3}$$

where, K= 0.1, 0.2 for twin-screw and single-screw ships, correspondingly.

Z = number of blades
P_O= the centreline of the propeller shaft static pressure
P_V= vapour pressure
D=propeller diameter

So, the cavitation constraint for the optimization is

$$\left[\frac{A_E}{A_O}\right] \geq \left[\frac{A_E}{A_O}\right]_{min} \tag{4}$$

A minimum amount of generated propeller thrust is also required to achieve a better overall performance. To ensure the thrust requirement, a thrust constraint is needed for the optimization. The generated propeller thrust (T_{CAL}) must be larger than the required thrust (T_R) and can be formulated as [3]:

$$T_{CAL} = K_T\, \rho\, n^2 D^4 \tag{5}$$

$$T_R = \frac{R_T}{N_p\,(1-t_d)} \tag{6}$$

where, ρ =seawater density
R_T=total resistance of the ship
N_p= number of propeller
t_d =thrust deduction

To maintain optimum strength of the propeller blades, the minimum blade thickness ratio should be considered in the optimization process. The minimum blade thickness to diameter ratio can be determined using the following formula [10]:

$$\left[\frac{t_{min}}{D}\right]_{0.7R} = 0.028 + 0.21\sqrt[3]{\frac{[3183.87 - 1508.15(P/D)]P_s}{1266652.04nD^3(S_c + 20.9D^2n^2)}} \tag{7}$$

where, $\left[\frac{t_{min}}{D}\right]_{0.7R}$ = minimum blade thickness ratio.

Using this equation and considering geometry of the propellers the blade thickness should satisfy the following criterion:

$$\left[\frac{t}{D}\right]_{0.7R} \geq \left[\frac{t_{min}}{D}\right]_{0.7R} \tag{8}$$

This is the strength constraint for the optimization process.

2.3 Optimization methods

2.3.1 NSGA II

Genetic algorithms follow an evolutionary approach to find out optimized solution for a problem [11]. In this single objective optimization problem, a special type of genetic algorithm is applied. Non-Dominated Sorting Genetic Algorithm uses a non-dominance arranging for the parent populations. Using the random parent population, new generations are found and sorted according to their fitness. Eventually the best possible values of the objective function are given as output. The algorithm uses a principle, i.e. the elitist has the right to carry out the procreation process for the next generation. Where an explicit diversity preservation mechanism is used that emphasizes the non-dominated solutions among all other solutions.

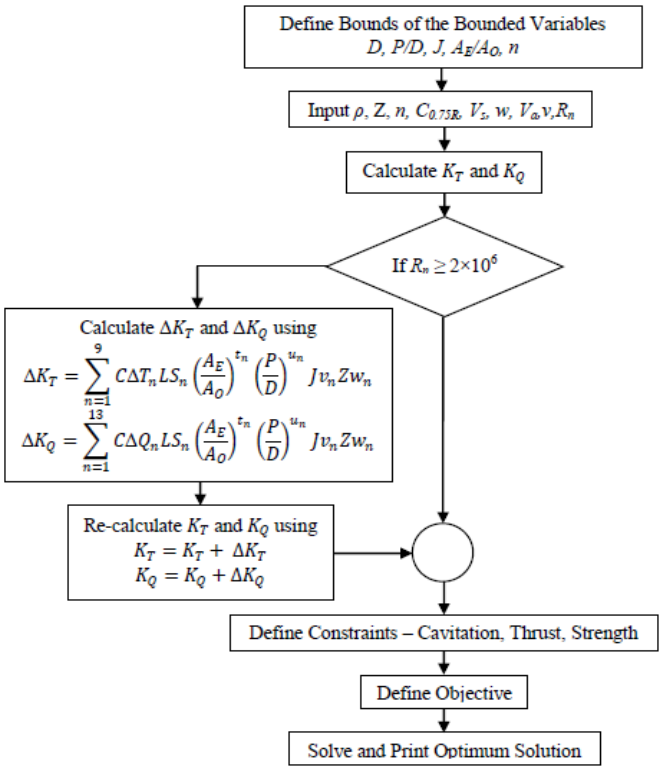

Fig. 1 Flowchart of the methodology followed in this study

2.3.2 Iterative Algorithm

Gaafary et al. [5] developed a special program that follows an iterative approach and specially designed for constrained single objective optimization to find optimum solution for B-series marine propellers.

2.3.3 Gekko

Gekko is an open-source python package that facilitates the use of python programming language in the field of dynamic optimization [11]. It is an Algebraic Modelling Language that facilitates the use of nonlinear model predicative control (NMPC), real-time optimization (RTO), moving horizon estimation (MHE), and dynamic simulation. Since propeller optimization problem is constrained non-linear problem so, the present study imposes this software package to address this issue. Method used in this study is illustrated by flowchart in Fig. 1.

Using the constraints and algorithms, numerical simulation has been done.

3 Numerical Simulation

Determination of the design parameters is the key factor for any optimization technique. Following the literature [5] the input data are listed in Table 1, the range of the bounded variables is given in Table 2, and to conduct the experiment for NSGA II technique, the input values are listed in Table 3.

Table 1 Input variable for numerical computation

Input Parameter	Value
Total resistance, R_T	35000 kN
Service speed, V_S	12 ms^{-1}
Number of propellers, N_P	2 (double screw)
Number of blades, Z	4
Propeller immersion, P_{CL}	2.5 m
Wake, W	0.2
Thrust deduction, t_d	0.15
Permissible stress, S_C	265 MPa
Height of propeller aperture, H_{pap}	1.2

Table 2 Range of bounded variables

Parameter	Range
Diameter, D	0.2 ~ 1.0
Expanded area ratio, A_E /A_O	0.3 ~ 0.8
Pitch, P/D	0.25 ~ 1.4
Advanced co-efficient, J	0.2 ~ 1.2
Rotating speed, n	5 ~ 15

Table 3 Parameters for NSGA II computation

Parameter	Value
Max generations	100
Population	100
Mutation probability	0.05
Distribution index	20
Crossover index	20

4 Results and Discussion

The calculations were done for 4-bladed B-series marine propeller. For each algorithm, 11 solutions were available. The advanced co-efficient, J plays a significant role in the performance of propeller. Decision variables are plotted in Fig. 2. It is found that, the K_T and K_Q shows analogous behaviour for all techniques. As the value of J increases, the value of K_T and K_Q decreases. K_T shows higher value for Gekko algorithm than the others.

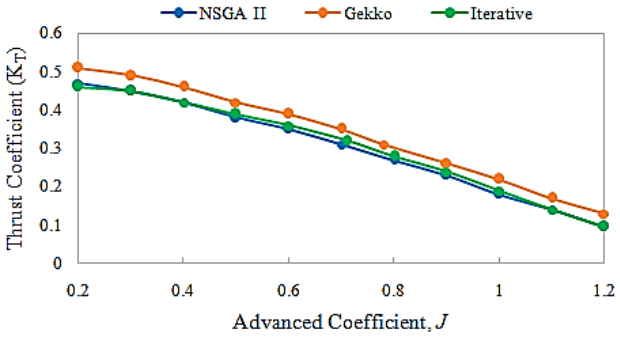

(a)

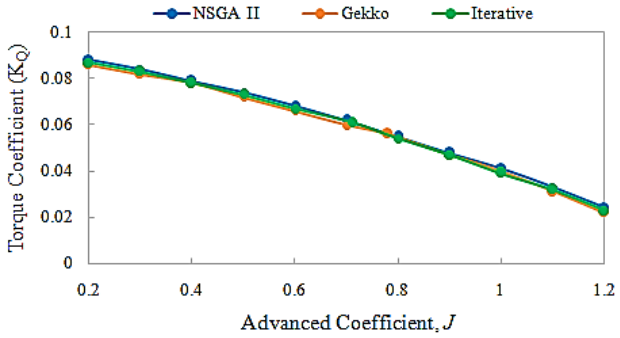

(b)

Fig. 2 (a) Thrust and (b) Torque co-efficient variation for different algorithms

It has been found that the open water diagram provides the insight of the performance of any marine propeller optimization technique. Fig. 3 illustrates the open water diagram for all algorithms used in this study. It can be seen that, with the increasing value of co-efficient J upto 0.8, the efficiency increases and for the higher value of J, it decreases gradually. Among 11 solutions, the best solutions are listed in Table 4 and the significant parameters are plotted in Fig. 4.

A single objective optimization approach is considered in this study and efficiency maximum is the only concern in this optimization technique. Fig. 5 depicts the trend of the efficiency for all algorithms.

Table 4 and Fig. 5 indicated that the efficiency reaches at its maximum value for the value of J, 0.8. Maximum efficiency is found for the iterative method though for the value of 0.8, it reaches at lowers than others two. From the findings from optimization techniques, it can be said that, for the considered environment and parameters, the variables determining the advanced co-efficient, should be set at the value for maximization of the output. Moreover, Gekko can be used for any optimization technique alongside the popular techniques considering lesser calculation time consumption and easy to handle constrained optimization problems point of view.

Table 4 Best solutions for each algorithm

Algorithm	D	P/D	J	A_E/A_O	n	η	T	Q	K_T	K_Q
NSGA II	0.90	1.30	0.80	0.5	14.1	0.625	36303.2	6647.8	0.27	0.055
Iterative	0.94	1.32	0.80	0.56	14.1	0.630	44963.0	8726.1	0.28	0.054
Gekko	0.92	1.38	0.78	0.56	14.0	0.625	45612.3	8887.8	0.27	0.055

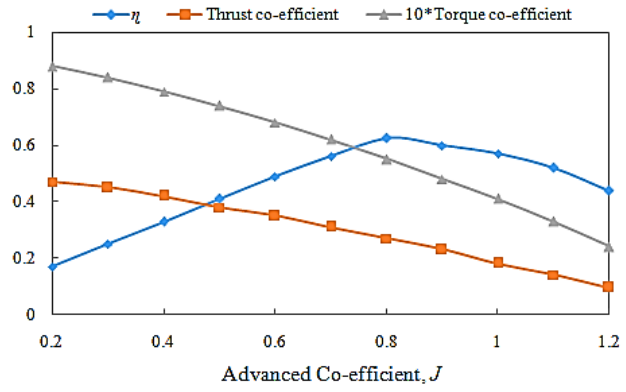

(a)

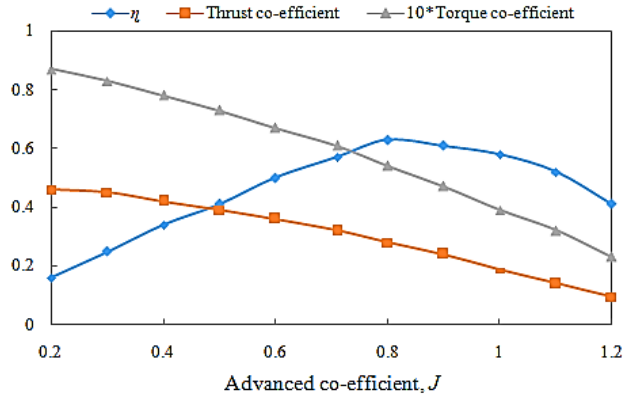

(b)

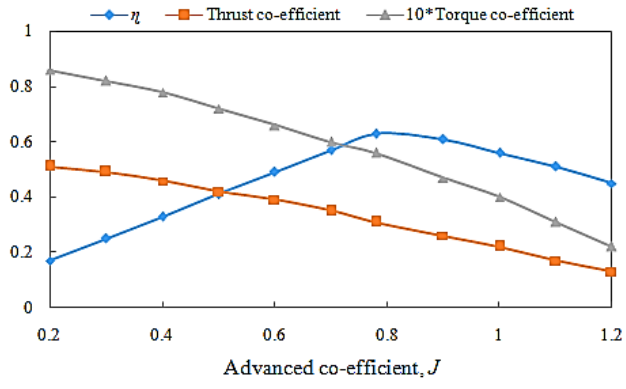

(c)

Fig. 3 Open water diagram for (a) NSGA II, (b) Iterative, (c) Gekko algorithm

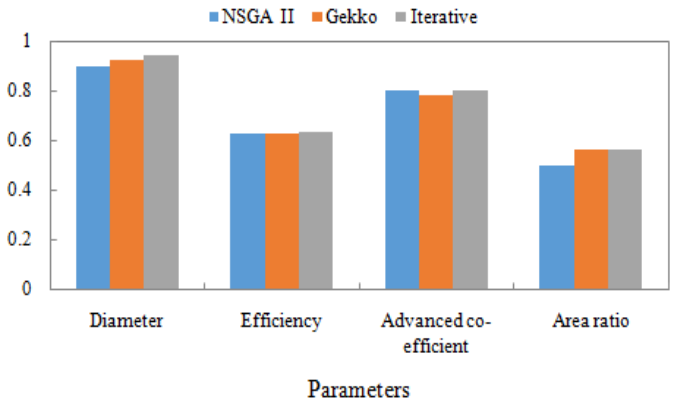

Fig. 4 Comparison of bounded variables used in this study for different algorithms

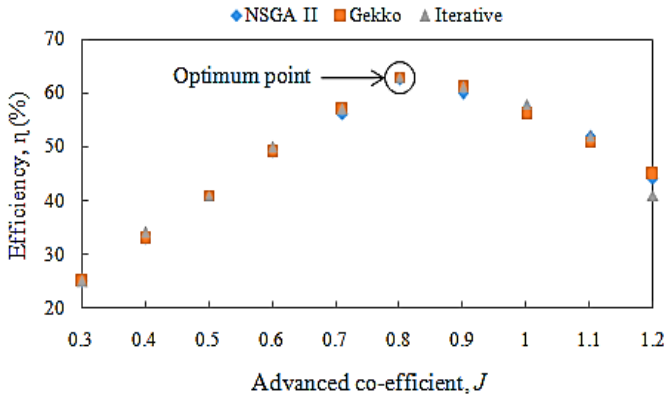

Fig. 5 Comparison of efficiency, found for different algorithms

5 Conclusion

A comparison of Non-Dominated Sorting Genetic Algorithm (NSGA II), Gekko optimization software package and an iterative algorithm in designing marine propeller is presented in this study. Three different methods yield in values in a close proximity to each other. The results also manifest a great agreement with theoretical characteristics of B-series marine propellers.Results from the three different methods have been compared to get a better method for design optimization of B-series propellers using single objective optimization. Though the iterative algorithm resulted in better efficiency, Gekko is recommended in terms of less time consumption and easy to handle constrained equations. So, its practice should be increased in the optimization field.

References

[1] Savic, D., 2002. Single-objective vs. multiobjective optimisation for integrated decision support. Proceedings of the First Biennial Meeting of the International Environmental Modelling and Software Society 1, 7-12.

[2] Xie, G., 2011. Optimal preliminary propeller design based on multi-objective optimization approach. *Procedia Engineering*, *16*, pp.278-283.

[3] Gaafary, M.M., El-Kilani, H.S. and Moustafa, M.M., 2011. Optimum design of B-series marine propellers. *Alexandria Engineering Journal*, *50*(1), pp.13-18.

[4] Mirjalili, S., Lewis, A. and Mirjalili, S.A.M., 2015. Multi-objective optimisation of marine propellers. *Procedia Computer Science*, *51*, pp.2247-2256.

[5] Windyandari, A., Haryadi, G.D. and Zakki, A.F., 2018. Optimization Procedure To Determine The Optimum Propeller Of Traditional Purse Seine Boat. *Technology*, *9*(13), pp.1519-1526.

[6] Oosterveld, M.W.C. and van Oossanen, P., 1975. Further computer-analyzed data of the Wageningen B-screw series. *International shipbuilding progress*, *22*(251), pp.251-262.

[7] Suen, J.B. and Kouh, J.S., 1999. Genetic algorithms for optimal series propeller design. *WIT Transactions on The Built Environment*, *45*.

[8] Benini, E., 2003. Multiobjective design optimization of B-screw series propellers using evolutionary algorithms. *Marine technology and SNAME news*, *40*(04), pp.229-238.

[9] Chen, J.H. and Shih, Y.S., 2007. Basic design of a series propeller with vibration consideration by genetic algorithm. *Journal of marine science and technology*, *12*(3), pp.119-129.

[10] Karim, M.M., 2000. A genetic algorithm (GA)-based optimization technique for the design of marine propellers. In *Proceedings of the propeller/shafting 2000 symposium. Virginia Beach, USA*.

[11] Beal, L.D., Hill, D.C., Martin, R.A. and Hedengren, J.D., 2018. Gekko optimization suite. *Processes*, *6*(8), p.106.

[12] Martínez-Cagigal V., 2021. Non Sorting Genetic Algorithm II (NSGA-II), (https://www.mathworks.com/matlabcentral/fileexchange/65494-non -sorting-genetic-algorithm-ii-nsga-ii), MATLAB Central File Exchange. Retrieved January 7, 2021.

SciEn
Journal of Engineering Advancements Vol. 02(03) 2021, pp 164-168 https://doi.org/10.38032/jea.2021.03.007

De-noising of an Image using Fuzzy Inference System and Performance Comparison with the Conventional system

Ahmed Farhan[1], Rezwan us Saleheen[2,], Chen Li Wei[1], Farhan Mahbub[2]*

[1]College of Information and Communication Engineering, Harbin Engineering University, Heilongjiang, China.
[2]Department of Mechatronics Engineering, World University of Bangladesh, Dhaka, Bangladesh.

Received: June 17, 2021, Revised: August 19, 2021, Accepted: August 31, 2021, Available Online: September 04, 2021

ABSTRACT

Noise prevailing in the image can diminish the physical appearance of the objects existing within the image and make them frail. Present research emphasizes a fuzzy inference system eradicating several types of noise from the images. The investigation implies the utilization of different levels of Salt & Pepper noise. Followed by the pixel determination applying a mask, the disparity between the focused pixel's intensity with the minimum, average, and maximum power of the chosen window has been determined. Since two fuzzy valued outputs have been obtained to match them, the one provided by a low noise rate would demonstrate the more accurate filter for the selected window. Utilizing Matlab the Peak Signal-to-Noise ratio (PSNR) and Mean Square Error (MSE) are determined for evaluating the noise reduction performance. However, these values of PSNR and MSE obtained from this research are also compared with the conventional fuzzy filtering system.

Keywords: Fuzzy Logic, Fuzzy Inference System, Salt & Pepper Noise, PSNR, MSE.

1 Introduction

The precision of processing an image debases with the existence of noise. So, de-noising of the image is notable in the arena of image processing. Nonlinear filtering procedures present superior results than linear techniques in the case of noise lessening. Current research on image processing using fuzzy logic shows that brilliant performance can be demonstrated using nonlinear approaches where fuzzy logic reasoning is the basis. Fuzzy logic deals with multiple values. However, Zadeh pioneered this logic. Computer software comprehends only binary functions. Conventional Boolean and Aristotelian logic contend with true or false, or the outright values of 0 and 1. But, fuzzy logic expresses like medium, smaller, and higher. Everything in this world cannot always follow a linear function. Fuzzy logic considers these phenomena. A conventional set of binary logic deals with crisp values, and the fuzzy sets have fuzzy values. It contains linguistic variables. It tends to be characterized as low or small, average or medium, and big or high [1]. The values have fuzzy margins and can intersect each other [2].

FIS is established on fuzzy sets, rules, and reasoning [3]. Besides, fuzzy reasoning is estimated reasoning. This procedure draws assumptions from fuzzy rules and fuzzy sets. Fuzzifier, rule base, inference engine, and de-fuzzifier are the components of this procedure. In a fuzzifier, fuzzy sets are created from crisp values. Then, fuzzy rules are formed. The fuzzy rules to the fuzzy sets are applied through the inference engine. The fuzzy output is determined from this. The resultant is a fuzzy value. So, to get the crisp value as output, the de-fuzzification fuzzification process is needed [2].

2 Literature Review

In modern days, scientists have developed various types of image de-noising methods using fuzzy logic. Mohebbian et al. [4] have used a combination of adaptive Type-2 Fuzzy filters and a Fast-ICA to filter a set of low-dose images. Moreover, they have utilized five different phantoms to examine several effects of de-noising. Because of some pictures, it is not helpful to use the deep learning method. The main innovation of this research is to convert the shot noise distribution to salt and pepper. Also, they removed noise from mapped images using independent and fast component analysis.

Some researchers have suggested a system that uses fuzzy cognitive maps to reduce noise from images and mean filters [5]. This proposed method minimizes the data loss in the noise reduction process with the mean filter. Mahalakshmi and a group of researchers utilized an adaptive filter with the optimization-based kernel interpolation and the type-2 fuzzy system to remove noise from the satellite image [6]. The authors have proposed three steps to remove noise from the images. They are noise identification, noise rectification, and enhancement of the image.

Golshan et al. [7] have developed an innovative Hysteresis Smoothing (HS) approach. Fuzzy norms are the basis of this method. In this method, fuzzy Hysteresis Smoothing is substituted by an interval soft manner. It allows the threshold levels to be determined equal to the fuzzy norm's free parameter. A. Saadia and A. Rashdi demonstrates an ultrasound image's de-noising using a fuzzy weighted mean [8]. They have offered a fractional integration filter. A $3 * 3$ window is applied around distinct pixels. The windows are assigned using fuzzy logic. An adaptive fuzzy logic approach has been proposed by some scholars for speckle reduction of the ultrasound image. However, two levels have been used for adaptiveness. Fuzzy logic has been applied to the coefficients of variation calculated from the picture with speckle noise [9].

Ananthi and Balasubramaniam proposed an innovative impulse noise revealing technique based on fuzzy sets [10]. They offered to investigate image de-noising by modeling the nebulousness of image as entropy. The authors have implemented the minimization of entropy to generate an IVIFS for the testing image. An innovative fuzzy decision filter is

*Corresponding Author Email Address: saleheen1@mte.wub.edu.bd

projected in [11] to evade the misclassification of a rigid threshold in interchanging vector filters. A fuzzy membership value is imposed for rendering the possessions of pixels. Pixels are restricted between the original and noisy image [12]. When the innermost pixel is noise-free, the pixel keeps untouched. An innovative FDW-SVR de-noising algorithm has been illustrated by Zhang et al., assigning fuzzy precedence for every sample to its density weight [13].

Altogether the study focused on some specific outcomes. Noise is evacuated without any efforts to expressly distinguish it with the non-linear filters. Salt and pepper noise is also acknowledged as impulse or spike noise. The degraded image by impulse noise holds white pixels in the black areas and black pixels in the white sections [14]. Errors in A/D converters are the precursor of this type of noise [15]. This sort of noise is also acknowledged as data drop noise in light of its unique information dropping [16]. Spatial filters eradicate noise to a sensible degree yet at the expense of obscuring images which thus makes the edges in images undetectable. Therefore a diversity of the nonlinear median type filters, for example, relaxed and weighted median filters have been established to overcome this issue [17]. To afford a wider and appropriate understanding of Fuzzy logic, an undersized overview of fuzzy logic in different types of image de-noising approaches. An algorithm using minimum, average and maximum difference of intensity of the targeted pixel as input can obtain a fuzzy valued output. Hence comparing the two outcomes specifies the comparative values of noise and also a more approximate filter for the selected window.

3 Methodology

The image which is degraded by salt & pepper noise includes dark pixels in the bright zones and bright pixels in the dark zones. The succeeding images are presented for visual comparison. Primarily, the original grayscale image has been shown and then the noisy image and the de-noised images by the projected method and the conventional fuzzy filtering method have been displayed for comparison. Fuzzy filters are grounded on 'IF and Then' rules. This is also known as fuzzy provisional statements. If 'X' denotes a universal set having 'x' number of elements and 'A' denotes a fuzzy set with the membership function μ_A, then

$$A = \{(x, \mu_A(x)) | x \in X\}. \quad (1)$$

The outcome of the fuzzy filters is governed by the fuzzy rules and the process of defuzzifying [18].

A real-life 'Leena' image [19] has been used as the original image, where different Salt & Pepper noise levels have been added with the image to get the test image for the experiment. 1% of noise has been considered as low level and 10% as the high level. A mean filter is a linear filter that utilizes a mask over each pixel in the picture. In the experiment, every part of the pixels under the mask has gained an intermediate value to form a distinct pixel. This filter can remove little noise from the noisy image, which degrades the image's visual quality [20].

Like the mean filter, the median filter also degrades image quality and removes less noise, and removes essential information with the noise. These two filters have worked here as supportive filtering systems to remove some noise initially before applying the proposed method. Fuzzy Multilevel Median Filter is a median filter with multiple levels and is combined with fuzzy rules for eliminating impulse noise from the image. The resultant outcome is,

$$r(x, y) = med(med_{max}(x, y), med_{min}(x, y), q(x, y)) \quad (2)$$

Here, $med_i(x, y)$ be the median values of the sub-windows $W_1(x, y)$, $W_2(x, y)$, $W_3(x, y)$ and $W_4(x, y)$ [18].

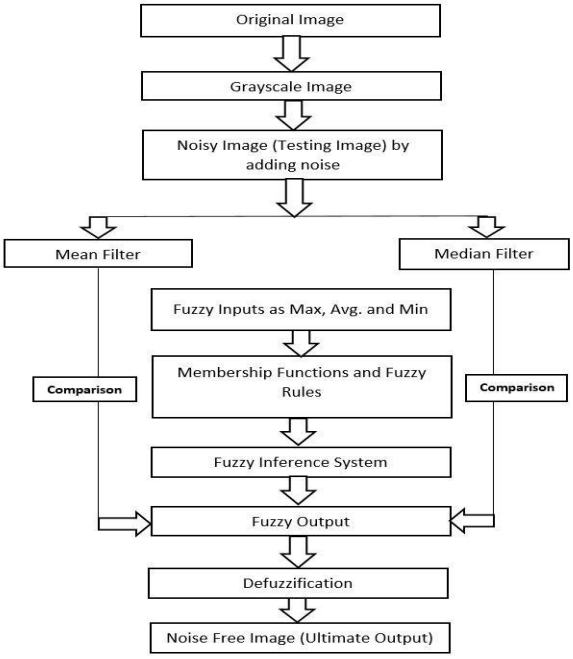

Fig. 1 Flow Chart of Proposed Fuzzy Inference System

The general system model is shown below in Fig. 1. Both mean and median filtering systems have been applied for the fuzzy inference system for comparison after getting the fuzzy inputs and outputs in fuzzification. Then, some membership functions have been formed for both inputs and output to fuzzify the data. After that, one $N * N$ mask has been used to select the pixel, where N denotes an odd number where N> 1. It can be 3, 5, 7, 9, etc.

Then, the difference between the intensity of the targeted pixel with the minimum, average, and maximum intensity of the specific window has been determined. After that, the minimum, average, and maximum differences have been passed as the inputs and obtained a fuzzy valued output. Then, another output has been determined, and compared the two outcomes and checked the significant result. Moreover, it was checked whether the mean or median filter is more approximate for this selected window. The boundary pixel intensity interchanged with the average gray level value of the $N * N$ mask with odd values (equal or greater than 3). This procedure was repeated to test all the pixels.

The fuzzy rules and the membership functions are the fundamental building block of the whole fuzzy inference system [21]. In the proposed method, three input variables having five membership functions have been used. Then, we used the outputs from the convolution of the mean and the median filter for comparison. The Mamdani model was used to make the fuzzy inference engine. This system will provide enhanced performance among all of the rules. Moreover, 125 fuzzy rules were estimated for the new assessment of the pixel under processing.

(a) (b)

(c) (d)

Fig. 2 (a) Original Gray Image, (b) Noisy Image (10% of Salt & Pepper noise), (c) Filtered image by the conventional method (PSNR is 31.0599, MSE is 50.9449), (d) Filtered image by our proposed method (PSNR is 31.6659, MSE is 44.2670).

Table 1 Performance comparison between conventional and our proposed method

Noise Level (%)	Peak Signal-to-Noise Ratio (PSNR)		Mean Square Erro (MSE)	
	Conventional Fuzzy Filtering System	Our Proposed Method	Conventional Fuzzy Filtering System	Our Proposed Method
1	32.6717	35.6879	35.1633	17.5421
1.5	32.5148	35.3826	36.4113	18.8399
2	32.3901	35.0967	37.5027	20.5159
5	32.0311	33.6141	40.7449	28.3190
10	31.0599	31.6659	50.9449	44.2670

For the input variables, the membership functions are very small (VS), small (S), medium (M), large (L), and very large (VL). These are similar for both maximum and minimum inputs.

For the medium input variables, the membership functions are very small (VS), small (S), medium (M), large (L), and very large (VL). For inputs for average values, we also have used the Gaussian membership function.

For the output, five membership functions also have to be used for the system. But, these membership functions are not similar to the inputs, and their range is also different. We used triangular type membership functions for output.

Five membership functions for all the inputs have been used to make 125 fuzzy rules for our proposed system.

Pixel distance has been generated in the existing window. This distance of the pixels has been used to calculate the two values used to compare mean and median filtering techniques and decide which one is applicable for that window pixel. The membership functions of the inputs are used to generate fuzzy if-then rules. Some of them are here,

- If the minimum distance is S and the median distance is VS, and the maximum distance is S, then output is VL.
- If the minimum distance is M and median distance is S, and the maximum distance is M, then output is L.
- If the minimum distance is L and the median distance is L, and the maximum distance is VS, then output is M.
- If the minimum distance is L, and median distance is L, and the maximum distance is L, then output is H.
- If the minimum distance is VL and the median distance is S, and the maximum distance is L, then output is VH.

After getting the fuzzified result, de-fuzzification has been performed to acquire a crisp value. Several methods are used, like the center of the area (CoA), the center of gravity (CoG), and the mean of maximum methods. In our system, the most most commonly used defuzzification method centroid method or center of area method was used. This method determines the center of area of the fuzzy set and returns the corresponding crisp value. The defuzzification step translates this linguistic result into a numerical value.The surface viewer of our proposed fuzzy inference system has been used to calculate and get the crisp value.

The assessment of our recommended scheme by comparing it with the conventional fuzzy filtering method has been projected based on PSNR and MSE of the filtered images.

The fraction of the concentrated probable power of a signal and the noise that disturbs the dependability of its demonstration is considered as PSNR of that signal. It is mostly used for determining the feature of restoration of the image. It is frequently stated in terms of logarithmic decibel measurement.

$$PSNR = 10\ log_{10}\left(\frac{Max_I^2}{MSE}\right) \quad (3)$$

Max_I is the highest potential value of the pixel of an image. For pixels with 8 bits per sample, the value of Max_I is 255. PSNR can be calculated from the known value of MSE.

MSE is as well acknowledged as mean square deviation or MSD. It is the measurement of the feature of an estimator. It is a risk function. It is always positive and non-zero. It has the similar unit of dimension as the square of the magnitude is assessed like variance.

$$MSE = \sqrt[2]{\frac{1}{MN}\sum_{x=0}^{M-1}\sum_{y=0}^{N-1}[F(x,y) - f(x,y)]^2} \quad (4)$$

Here, F(x, y) is the absolute resultant image obtained from the suggested method and *f(x, y)* denotes the novel image. M and N denote the height and the width of the testing grayscale image. If PSNR is known, then MSE can also be calculated from Eq. (3).

4 Results Analysis and Discussion

Fig. 2 represents the visual comparison of the noisy image and the output images for both methods. Table 1 shows the comparison of performance parameters of both methods.

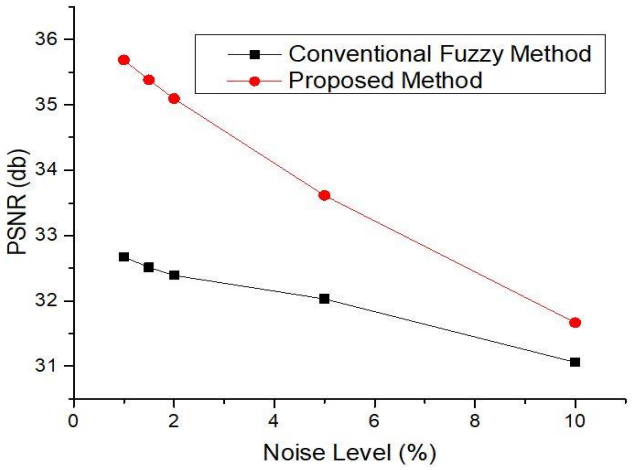

Fig. 3 PSNR versus Noise Level

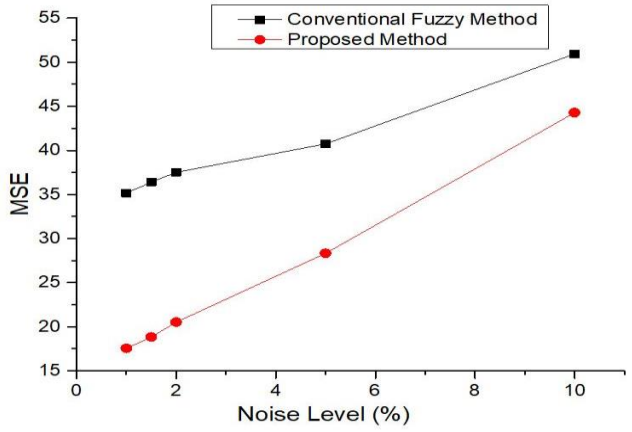

Fig. 4 MSE versus Noise Level

Fig. 3 and Fig. 4 represent the graphical comparisons of the performance parameters. The graphical representation in Fig. 3 is for different Speckle Noise level. 1% or 0.01 has been considered as the minimum noise level and 10% or 0.1 has been taken as a maximum noise level for this experiment. The method has been designed in such a way that the experiment can be directed for any level of noises (less or more) in the testing image. This graph demonstrates the change of the PSNR value with the growth of the noise level. With the rise of noise level, the value of PSNR drops for both cases.

In the case of our recommended method, there is a significant change in the value of PSNR for noise level 0.01 to 0.2. For the traditional method, there was no dramatic change in PSNR value. From the graphical display, we notice that the values of PSNR for all noise levels are better than the traditional fuzzy filtering system. Thus, the projected method can deliver a better result in the case of eliminating speckle noise.

The graph in Fig. 4 is for different Speckle Noise levels. 1% or 0.01 has been considered as low noise level and 10% or 0.1 has been taken as a high noise level for this experiment. The structure has been planned in such a technique that the experimentation can be directed for any level of noises (less or more). This line-graph clarifies the rise of the MSE value with the growth of the noise level. That illustrates the reduction of error is optimum for our proposed method.

5 Conclusion

A novel approach based on a fuzzy inference system has been proposed to eradicate noise from a noisy image better than other filtering systems. The correlated works and the deficiencies of previous research works have been highlighted and evaluated here. The projected system had been generated dependent on the mean and median filter, fuzzy logic, and fuzzy inference system, where a noisy image has been used as the test image. The difference between the targeted pixel's minimum, average, and maximum window intensity was calculated and passed as input, and fuzzy valued outputs were obtained using the same procedure. We compared them to select the more appropriate filter for this chosen window and the outcomes. These outcomes and the fuzzy conventional filtering method's outcomes have been compared using PSNR and MSE as the comparison factors. The measurable experiments appear that our recommended procedure works admirably for the salt and pepper noise. Better PSNR denotes better effectiveness, where the shrink of MSE implies more minor errors.

The further recommendation is to add additional filters, for example, Gaussian smoothing, to compare extra output and find out the best filtering system for the contemporary window. Therefore, more data will be analyzed, and the efficiency will be superior to this model.

References

[1] Blanes-Vidal, V., Cantuaria, M.L. and Nadimi, E.S., 2017. A novel approach for exposure assessment in air pollution epidemiological studies using neuro-fuzzy inference systems: Comparison of exposure estimates and exposure-health associations. *Environmental research*, *154*, pp.196-203.

[2] Godil, S.S., Shamim, M.S., Enam, S.A. and Qidwai, U., 2011. Fuzzy logic: A “simple” solution for complexities in neurosciences?. *Surgical* neurology *international*, *2*.

[3] Farhan, A., Wei, C.L. and Ahmed, M.T., 2018. A Qualitative Overview of Fuzzy Logic in ECG Arrhythmia Classification. *International Journal of Engineering Works*, 5(11), pp. 232-239.

[4] Mohebbian, M.R., Hassan, A.M., Wahid, K.A. and Babyn, P., 2020, June. Multi-Frame Low-Dose CT Image noise reduction using Adaptive Type-2 Fuzzy filter and Fast-ICA. In *2020 IEEE Region 10 Symposium (TENSYMP)* (pp. 690-693). IEEE.

[5] Altundogan, T.G. and Karakose, M., 2020, May. A Noise Reduction Approach Using Dynamic Fuzzy Cognitive Maps for Vehicle Traffic Camera Images. In *2020 Zooming Innovation in Consumer Technologies Conference (ZINC)* (pp. 15-20). IEEE.

[6] Mahalakshmi, T. and Sreenivas, A., 2020. Adaptive Filter with Type-2 Fuzzy System and Optimization-Based Kernel Interpolation for Satellite Image Denoising. *The Computer Journal*, *63*(6), pp.913-926.

[7] Golshan, H. and Hasanzadeh, R.P., 2021. Fuzzy Hysteresis Smoothing: A New Approach for Image Denoising. *IEEE Transactions on Fuzzy Systems*, *29*(3), pp.686-697.

[8] Saadia, A. and Rashdi, A., 2016. Fractional order integration and fuzzy logic based filter for denoising of echocardiographic image. *Computer methods and programs in biomedicine*, *137*, pp.65-75.

[9] Babu, J.J.J. and Sudha, G.F., 2016. Adaptive speckle reduction in ultrasound images using fuzzy logic on Coefficient of Variation. *Biomedical Signal Processing and Control*, *23*, pp.93-103.

[10] Ananthi, V.P. and Balasubramaniam, P., 2016. A new image denoising method using interval-valued intuitionistic fuzzy sets for the removal of impulse noise. *Signal Processing*, *121*, pp.81-93.

[11] Wang, G., Zhu, H. and Wang, Y., 2015. Fuzzy decision filter for color images denoising. *Optik*, *126*(20), pp.2428-2432.

[12] Wang, G., Liu, Y., Xiong, W. and Li, Y., 2018. An improved non-local means filter for color image denoising. *Optik*, *173*, pp.157-173.

[13] Zhang, Y., Xu, S., Chen, K., Liu, Z. and Chen, C.P., 2016. Fuzzy density weight-based support vector regression for image denoising. *Information Sciences*, *339*, pp.175-188.

[14] Singh, V., Dev, R., Dhar, N.K., Agrawal, P. and Verma, N.K., 2018. Adaptive type-2 fuzzy approach for filtering salt and pepper noise in grayscale images. *IEEE transactions on fuzzy systems*, *26*(5), pp.3170-3176.

[15] Farooque, M.A. and Rohankar, J.S., 2013. Survey on various noises and techniques for denoising the color image. *International Journal of Application or Innovation in Engineering & Management (IJAIEM)*, *2*(11), pp.217-221.

[16] Boyat, A.K. and Joshi, B.K., 2015. A review paper: noise models in digital image processing. *arXiv preprint arXiv:1505.03489*.

[17] Motwani, M.C., Gadiya, M.C., Motwani, R.C. and Harris, F.C., 2004, September. Survey of image denoising techniques. In *Proceedings of GSPX* (Vol. 27, pp. 27-30). Proceedings of GSPX.

[18] Nachtegael, M., Van der Weken, D., Van De Ville, D. and Kerre, E.E. eds., 2013. *Fuzzy filters for image processing* (Vol. 122). Springer.

[19] Gonzalez, R.C. and Woods, R.E., 2008. Digital image processing: Pearson International Edition.

[20] Patidar, P., Gupta, M., Srivastava, S. and Nagawat, A.K., 2010. Image de-noising by various filters for different noise. *International journal of computer applications*, *9*(4), pp.45-50.

[21] Ahmad, M.T., Greenspan, M., Asif, M. and Marshall, J.A., 2018, April. Robust Apple Segmentation using Fuzzy Logic. In *2018 5th International Multi-Topic ICT Conference (IMTIC)* (pp. 1-5). IEEE.

This page is left intentionally blank

Journal of Engineering Advancements (JEA)

DOI: https://doi.org/10.38032/jea

Indexed by:

Volume 02 Issue 03

DOI: https://doi.org/10.38032/jea.2021.03

Published by: SciEn Publishing Group

Website: www.scienpg.com